EVALUATION OF INDUCED LATERAL STRESSES FROM NOISE WALL LOADING ONTO FLEXIBLE RETAINING WALLS

by

MICHAEL ZIMMERMAN

A thesis submitted in partial fulfillment of the requirements for the degree of

MASTER OF SCIENCE

(CIVIL AND ENVIRONMENTAL ENGINEERING)

At the

UNIVERSITY OF WISCONSIN-MADISON

2019

EVALUATION OF INDUCED LATERAL STRESSES FROM NOISE WALL LOADING ONTO FLEXIBLE RETAINING WALLS

Approved

Dr. Dante Fratta, Assoc. Professor

Date: 5/10/19

Abstract

While the effects of uniform vertical surcharges have been studied extensively (e.g., Spangler 1956; Jarquio 1981; Georgiadis and Anagnostopoulos 1998; Greco 2006), the induced lateral pressures from horizontal (shearing) surcharge and non-uniform vertical surcharges is largely unknown. Past researchers (e.g., Steenfelt and Hansen 1983; Georgiadis and Anagnostopoulos 1998) have both analytically and experimentally found that plastic limit equilibrium solutions best predict these induced lateral pressures. Based on the success of plastic solutions predicting the response of retaining walls under uniform vertical surcharge loading, a modified limit equilibrium methodology was proposed to quantify the pressures from horizontal surcharge and non-uniform vertical surcharges. To validate this proposed methodology, a small-scale experimental model is constructed and tested. The experimental testing program included varying distances from the applied surcharge to the retaining wall and varying the magnitudes of these horizontal and vertical surcharges.

Results revealed that smaller distances, d, between the surcharge and the retaining walls and larger surcharge magnitudes, q_h and q_{vo}, result in higher bending moments due to higher lateral pressures. The experimental results were then compared with predictions from the proposed plastic solution, a solution based on elasticity theory, and an approximate method discussed in Berg et al. (2009) based on the AASHTO LRFD Bridge Design manual. The proposed plastic model was found to be the most accurate method of predicting the bending moment response of induced stresses from the noise wall surcharge loading for both small and large values of d. Ultimately, the values of d, q_h, q_{vo}, and ϕ (friction angle of backfill soil) were determined to control the threshold of whether a surcharge will affect a cantilever retaining wall.

Acknowledgement

To begin, a huge thank you to Dante Fratta for his continuous support, discussion and sense of humor throughout my graduate studies. His encouragement to pursue every avenue in research and willingness to answer any questions (ranging from Critical State Soil Mechanics to Seinfeld quotes) has been invaluable. I would also like to thank Professors Bill Likos and James Tinjum for taking the time to serve on my defense committee and to the Wisconsin Department of Transportation for funding my graduate studies. Next, I would like to extend my gratitude to Xiaodong Wang for assisting with the construction of my model, setting up the data logging system, and for always lending a hand when asked. I would also like to thank the GLE/CEE office staff, especially Katie Bourassa and Jamie Zander Valentine, for their help and patience with any and all purchasing and administrative questions I had throughout graduate school.

A huge shout out the many fellow graduate students and colleagues in GLE and CEE, graduate school would not have been the same without you. Some of my favorite memories gained during my time as a Master's student have been going through the struggle together and learning about their research and culture along the way. I would also like to extend my thanks to all my friends outside of school for their support and providing an escape from studies.

Last but not least, I want to thank my parents, Bill and Maggie, my brother, Bill, my sister, Sarah, and my brother-in-law Carlos. Their constant love and support were always felt and without them, this thesis would not be possible.

Table of Contents

List of Figures

1 Introduction

Noise pollution from sources like highway traffic can negatively affect areas adjacent to high-volume roadways in a variety of ways ranging from human health and to the environmental wellbeing of wildlife (Singh et al. 2017; Kaseloo and Tyson 2004). Noise wall barriers provide a way to reduce or abate noise pollution from highway traffic by "absorbing, transmitting, reflecting noise or forcing it to take a longer path over and around the barrier" (FHWA 2001). These barriers come with a substantial cost – Wisconsin alone has spent $91 million since 1981 for over 60 km of noise barriers (FHWA 2019). As transportation projects get more complex and highway traffic volumes increase, greater lengths of noise wall barriers and other abatement structures are needed to reduce the effect of traffic noise next to high-volume roadways. An example of an implemented noise wall system at the Zoo Interchange in Milwaukee, WI.

The overall system at the Zoo Interchange studied for this research includes two independent, but interrelated, elements (Figure 1.1): the noise wall and the earth retention system. The noise wall includes the noise barrier fixed to an anchor (i.e., sleeper) slab. The noise wall in Figure 1.2a carries two types of distributed loads to the underlying soil: vertical dead load from self-weight of the noise barrier and sleeper slab and horizontal loads from wind acting on the noise barrier portion. Since the resultant of the distributed wind load acts at a height above the base of the noise wall system, the wind also produces an overall moment that ultimately produces a linearly varying, distributed soil load in the vertical direction. These distributed loads are then transmitted to the underlying soil within the backfill portion of the retaining wall (Figure 1.2b).

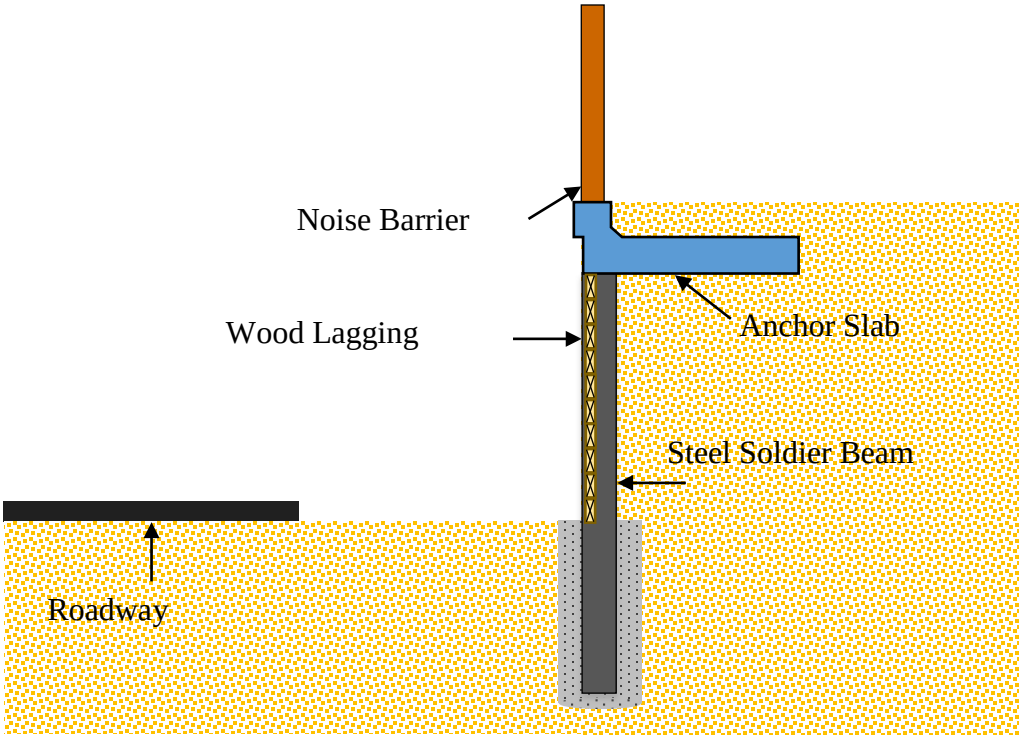

Figure 1.1. Schematic of the Zoo Interchange (Milwaukee, WI) combined noise wall system and soldier beam and lagging retaining wall system.

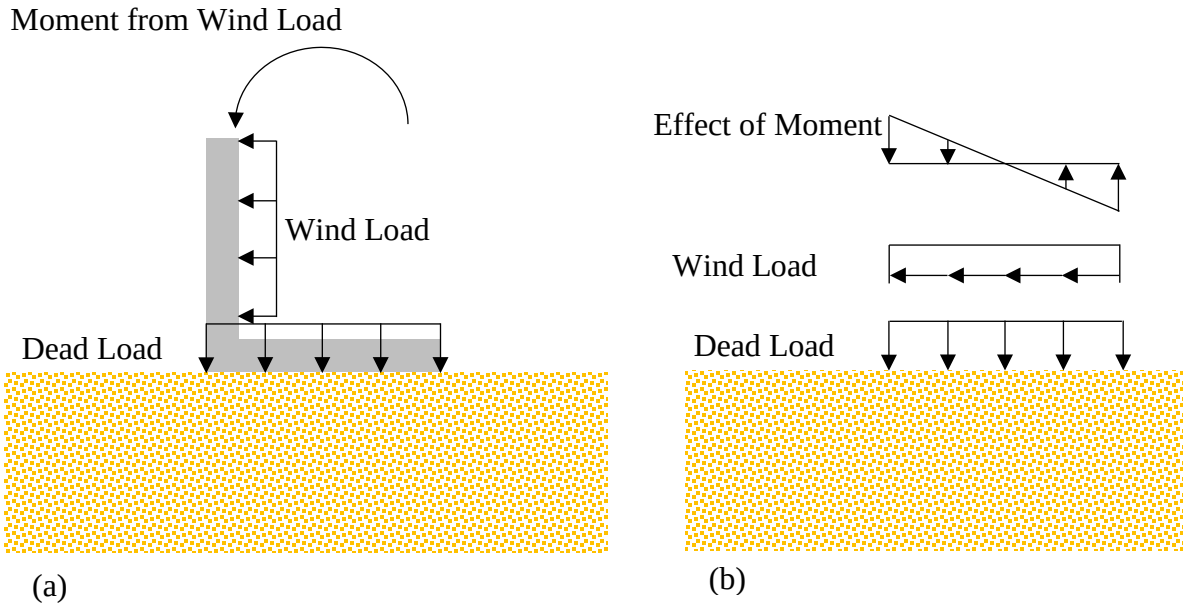

Figure 1.2. Noise wall system (a) external load sources from self-weight and wind and (b) loading effects from noise wall to underlying soil.

The soldier beam and lagging wall supporting a noise wall system at the Zoo Interchange includes steel soldier piles, wood lagging, and the concrete footing shown in Figure 1.1. The system is a flexible type of retaining wall, which relies on a portion of the retaining wall cantilevered into soil below the excavation depth to support the retained soil. The wood lagging retains the backfill and transfers the soil pressure to the soldier beam and concrete footing below. Finally, the concrete footing is supported by the soil within the excavation to stabilize the entire system. While the noise wall and retaining wall systems are independent from one another, the reactions from the noise wall system are supported by the backfill of the retaining wall and therefore affects the overall stability of the earth retention system.

While the effects of vertical surcharge on earth retention systems, like that of dead load from a noise wall system, have been studied rather extensively (Rowe 1952; Georgiadis and Anagnostopoulos 1998; Greco 2006; etc), the effect of horizontal surcharges and moments are relatively unknown. Two known design methods—an elastic method and an approximate method from AASHTO (Berg et al. 2009)—do not appear to accurately account for horizontal loads and moments applied to flexible retaining walls (discussed in detail in Chapter 2). To ensure both safe and economical designs of retaining wall systems, the effect of all three contributing surcharge load types need to be considered, in addition to the lateral earth pressures from the self-weight of the soil. The goal of this research project is to quantify the induced horizontal stresses from these surcharges on the retaining wall system. This will be accomplished by first developing a plastic solution and then testing this solution with experimental testing.

2 Background

2.1 Effective Horizontal Stresses under K_o, K_a, and K_p conditions

Stresses of soil beneath the earth's surface vary according to depth and other factors including but not limited to the presence of nearby structures, soil type, and soil unit weight. Figure 2.1 shows a soil element below the ground surface. The amount of stress that the system of soil particle structure supports in the vertical direction, i.e., the vertical effective stress, is equal to:

$$\sigma'_v = \sigma_v - u_w = \left(\sum_i \gamma_i z_i\right) - u_w \quad (1)$$

where σ_v is the total stress due to self-weight of the soil particles above the soil element and u_w is the pressure of water between the soil particles within the soil element. Total stress, σ, is equal to the sum of $\gamma_i z_i$ where γ_i is equal to the unit weight and z_i is the thickness of soil layer, i, above the point of interest.

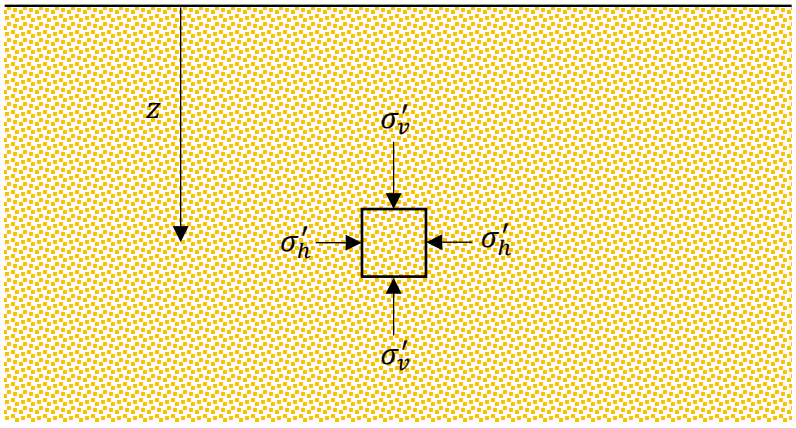

Figure 2.1. Effective stress in the vertical and horizontal directions on a soil element below the ground surface.

In the absence of any water in the void spaces between particles, u_w is equal to zero and $\sigma'_v = \sigma = \sum_i \gamma_i z_i$. The effective stress in the horizontal direction, σ'_h, is equal to the vertical effective stress multiplied by the lateral earth pressure coefficient, K, resulting in:

$$\sigma'_h = K\sigma'_v \tag{2}$$

The value of K is variable depending on how the soil is loaded with three important values: K_o, K_a, and K_p. The first of these values, K_o, is the value for soil under no lateral strain (i.e., at rest). If lateral confinement is gradually removed, lateral strain develops and the value for K and σ'_h are decreased. Eventually the soil element will fail when $K = K_a$, the active coefficient of lateral earth pressure. Conversely, if lateral confinement is slowly increased, the value of K and σ'_h will increase until failure when $K = K_p$. With these cases in mind, $K_a \leq K \leq K_p$ and the actual value of K can be anywhere between the two boundaries and is dependent on the amount of lateral strain the particular soil element has experienced.

2.2 Lateral Earth Pressures for Retaining Walls

In the case of retaining walls, researchers have proposed several methods to model the distribution of lateral pressure for design. Atkinson (2007) discusses the solution that Coulomb

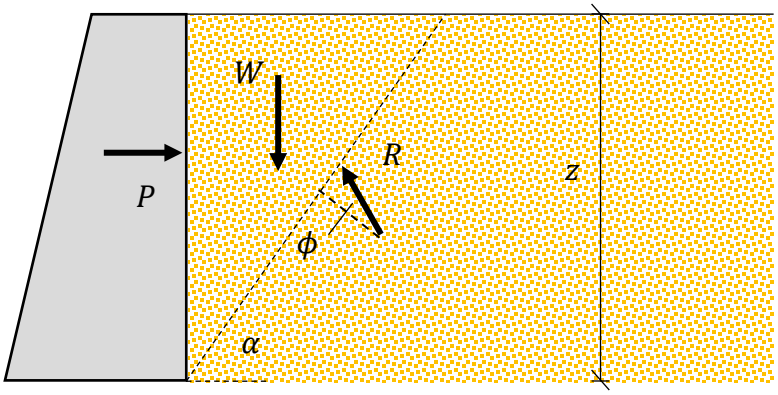

Figure 2.2. Coulomb solution for active state of failure for retaining wall under loading from self-weight of soil.

developed in 1776. Coulomb's solution provided a method to calculate the lateral thrust along a retaining wall by solving the force equilibrium of a soil wedge with an assumed planar failure surface. Figure 2.2 shows the active failure case where the failure wedge, inclined off of the horizontal plane at some angle, α, is exerting a horizontal thrust, P, onto the retaining wall. Coulomb's original model also assumes 1) a frictionless retaining wall 2) a horizontal backfill, and 3) a vertical retaining wall face. The rigid block with a weight, W, is in equilibrium with the reaction between the wedge and the surrounding soil, R, and the reaction between the failure wedge and the retaining wall, P. Solving the equilibrium equation for P results in an equation in terms of α:

$$\mathrm{P} = \frac{1}{2}\gamma \mathrm{z}^2 \frac{1}{\tan(\alpha)} \frac{\sin(\alpha - \phi)}{\cos(\alpha - \phi)} = \frac{1}{2}\gamma \mathrm{z}^2 \frac{1}{\tan(\alpha)} \tan(\alpha - \phi) = \frac{1}{2}\gamma \mathrm{z}^2 f(\alpha)\mathrm{g}(\alpha) \qquad (3)$$

where $f(\alpha) = \frac{1}{\tan(\alpha)}$ and $g(\alpha) = \tan(\alpha - \phi)$.

These two competing terms exist within the function in Equation 3: the function $f(\alpha)$, is related to the lateral extent of the failure wedge, and the load transfer function $\mathrm{g}(\alpha)$, relates how much of the self-weight of the wedge is transferred to the thrust, P. These two functions are inversely related: $f(\alpha)$ *decreases* as the wedge inclination angle, α, increases and $g(\alpha)$ *increases* as α increases. When these two terms are multiplied, they form the lateral earth pressure coefficient, $K(\alpha) = f(\alpha)g(\alpha)$. A graphical example of the dependency of $f(\alpha)$, $g(\alpha)$, and $K(\alpha)$ on α is shown in Figure 2.3 for $\phi = 30°$ and $\delta = 0°$. As expected, the critical wedge inclination angle, α_c, that produces the maximum value of $K(\alpha)$ occurs at $45° + \frac{\phi}{2} = 60°$, precisely the same value as Coulomb and Rankine had independently calculated using upper and lower bound solutions, respectively.

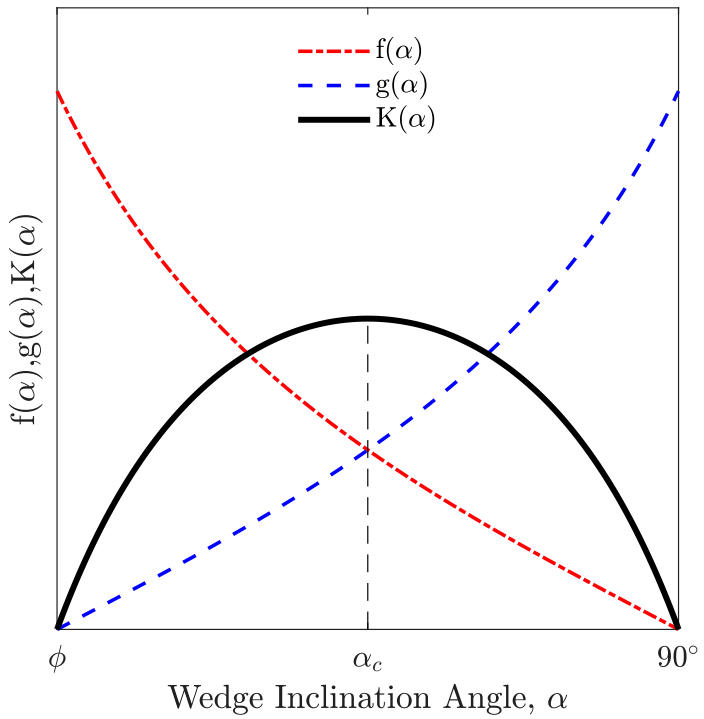

Figure 2.3. Effect of inclination angle,α, on the functions $f(\alpha)$, $g(\alpha)$, and $K(\alpha)$

Alternatively, the maximum value of thrust exerted by the soil onto the wall, P_{max}, can be determined analytically by differentiating Equation 3 with respect to α and setting equal to zero; that is: $\frac{dP}{d\alpha} = 0$ where:

$$\frac{dP}{d\alpha} = 0 = \frac{1}{2}\gamma z^2[\cot(\alpha)\sec^2(\alpha-\phi) - \csc^2(\alpha)\tan(\alpha-\phi)] \quad (4)$$

$$0 = [\cot(\alpha)\sec^2(\alpha-\phi) - \csc^2(\alpha)\tan(\alpha-\phi)]$$

Solving Equation 4 yields a maximum P when $\alpha_c = 45° + \frac{\phi}{2}$, precisely the same value independently determined by the Coulomb and Rankine. Note for Equation 4 that the value of α_c is only dependent on ϕ, and therefore is independent of z and γ. Equation 3 can then be rewritten so that:

$$P_{max} = \frac{1}{2}\gamma z^2 \mathrm{f}(\alpha_c)\mathrm{g}(\alpha_c) = \frac{1}{2}\gamma z^2 \frac{\tan\left(45° + \frac{\phi}{2} - \phi\right)}{\tan\left(45° + \frac{\phi}{2}\right)} = \frac{1}{2}\gamma z^2 \tan^2\left(45° - \frac{\phi}{2}\right) = \frac{1}{2}\gamma z^2 K_{aC} \quad (5)$$

where K_{aC} is the active earth pressure coefficient according to Coulomb's theory.

Coulomb also developed a similar approach for the passive case, shown in Figure 2.4, where the soil resists a thrust P. Solving for equilibrium results in the expression for thrust:

$$P = \frac{1}{2}\gamma z^2 \cot(\alpha)\tan(\alpha + \phi) \quad (6)$$

To find the plane resulting in the minimum resistive thrust, P_{min}, the derivative of Equation 6

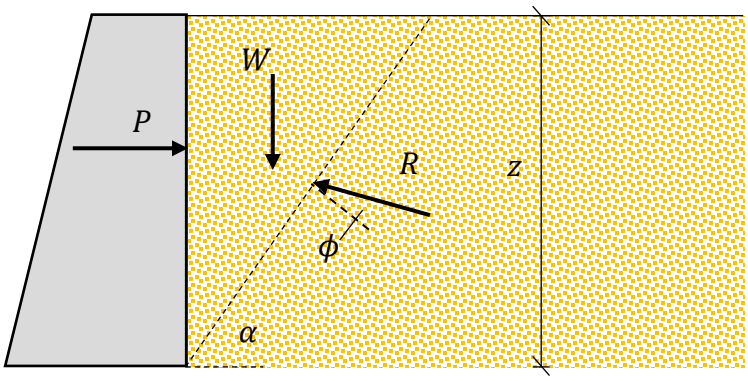

Figure 2.4. Coulomb solution for passive state of failure for retaining wall under loading from self-weight of soil.

can be taken with respect to α and set to zero; that is:

$$\frac{dP}{d\alpha} = 0 = \frac{1}{2}\gamma z^2[\cot(\alpha)\sec^2(\alpha + \phi) - \csc^2(\alpha)\tan(\alpha + \phi) \quad (7)$$

$$0 = [\cot(\alpha)\sec^2(\alpha + \phi) - \csc^2(\alpha)\tan(\alpha + \phi)]$$

Solving Equation 7, P_{min} occurs when $\alpha = \alpha_c = 45° - \frac{\phi}{2}$. Using $\alpha = \alpha_c$ for Equation 6, P_{min} can be solved as:

$$P_{min} = \frac{1}{2}\gamma z^2 \frac{\tan\left(45° - \frac{\phi}{2} + \phi\right)}{\tan\left(45° - \frac{\phi}{2}\right)} = \frac{1}{2}\gamma z^2 \tan^2\left(45 + \frac{\phi}{2}\right) = \frac{1}{2}\gamma z^2 K_{pC} \quad (8)$$

where K_{pC} denotes the passive earth pressure coefficient derived from Coulomb's theory.

The previous assumption that the wall is frictionless is in contrast to evidence, as significant friction can develop at the interface between the wall and soil (Naval Facilities Engineering Command 1982; United States Steel 1984). This interfacial friction, δ, inclines the thrust, P, as shown in Figure 2.5. Solving for equilibrium gives the following equation for P:

$$P = \frac{1}{2}\gamma z^2 f(\alpha) g(\alpha) \quad (9)$$

where $g(\alpha) = \frac{\sin(\alpha - \phi)}{\cos(\alpha - \delta - \phi)}$.

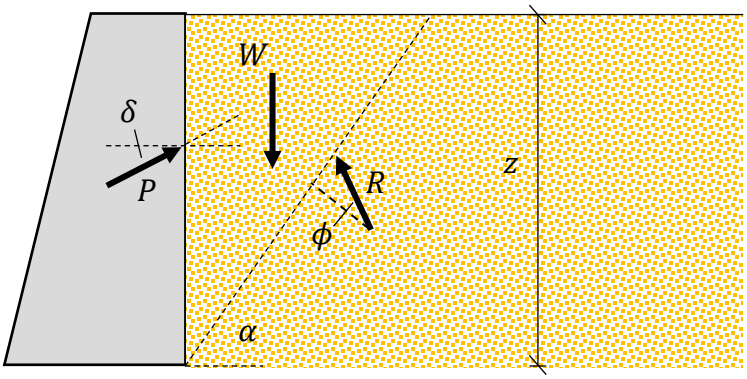

Figure 2.5. Coulomb solution for active state of failure considering friction between retaining wall and soil.

The values of K_a and K_p can be modified according to the model proposed by Poncelet (1840):

$$K_a = \frac{\cos^2(\phi)}{\cos(\delta)\left[1 + \left\{\frac{\sin(\phi + \delta)\sin(\phi)}{\cos(\delta)}\right\}^{\frac{1}{2}}\right]^2} \quad (10)$$

$$K_p = \frac{\cos^2(\phi)}{\cos(\delta)\left[1 - \left\{\frac{\sin(\phi+\delta)\sin(\phi)}{\cos(\delta)}\right\}^{\frac{1}{2}}\right]^2} \quad (11)$$

where δ is the interfacial friction angle between the retaining wall and the soil. This interfacial friction causes the failure surface to curve and, therefore the assumption of a planar failure surface deviates from reality (United States Steel 1984). For the active case, the curving effect is negligible and the planar failure surface assumption results in insignificant errors compared to the curved surface (Brinch Hansen 1953), as Figure 2.6 illustrates. For the passive case, however, the calculated pressures may be more than 50% greater than the values derived from a curved failure surface. To account for the large difference for the passive case, Caquot and Kerisel (1948) developed approximate correction factors for the passive earth pressure coefficient presented by Coulomb's solution, K_{pC}. In light of this, straight-line failure surfaces will be assumed for active pressures and passive earth pressure coefficients will be corrected. One major drawback to Coulomb's original theory is that the solution yields the *force* from the

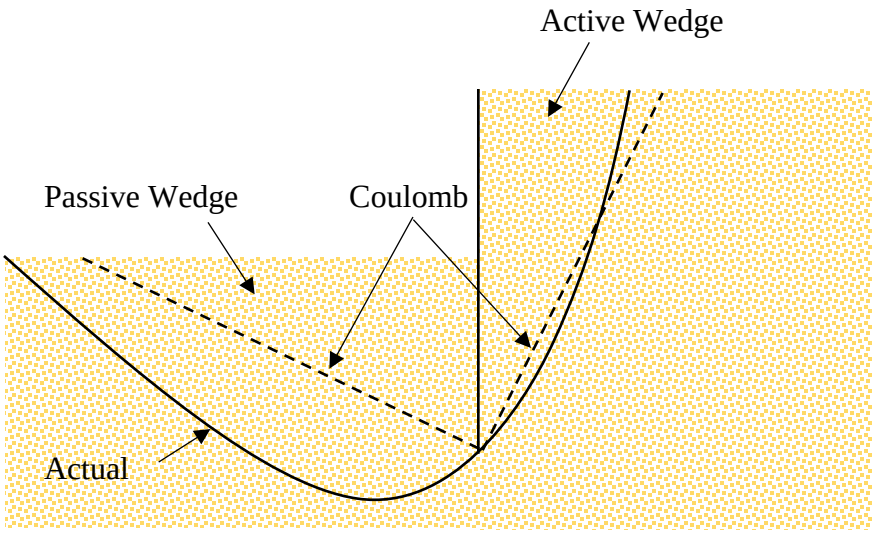

Figure 2.6. Actual failure surface (solid line) vs. the assumed planar failure surfaces from Coulomb's theory (after Terzaghi 1954).

soil wedge, not stress, along the wall since the concept of stress had not yet been derived for soil mechanics applications in the 18th century. This issue will be discussed in later sections.

Atkinson (2007) also discusses the theory from Rankine (1857) that offers a solution for lateral earth pressure distribution by way of a lower bound solution, satisfying plastic equilibrium while not violating Coulomb's failure criterion. Rankine's theory employs the use of stress states to develop lateral earth pressure. If a soil element is initially in the at rest condition, the vertical and horizontal stresses are equal to σ_v' and $K_o\sigma_v'$, respectively. These stresses are plotted in Mohr space in Figure 2.7, with the initial stress state plotted as circle AB. Line OF represents the Coulomb's failure criterion, inclined at an angle equal to the friction angle, ϕ, relative to the effective stress axis.

At the initial stress state, the soil is at a stable state since the Mohr's circle is below the failure criterion. The soil along the wall on the backfill side of a retaining wall will have a constant σ_v' and a decreasing σ_h' as soil is excavated, causing a decrease in confinement of the backfill soil. This decrease in σ_h' increases the deviatoric stress, $\Delta\sigma = \sigma_1' - \sigma_3' = \sigma_v' - \sigma_h'$, causing the Mohr's circle to increase in diameter. This decrease in σ_h' will occur until circle AC touches the failure criterion at Point D. The horizontal effective stress at this point can be computed using geometry, with a resulting $\sigma_h' = K_a\sigma_v' = \frac{1-\sin(\phi)}{1+\sin(\phi)}\sigma_v'$, meaning the soil is at the active failure state of failure.

If, instead, the wall is applying pressure to the soil, as is the case for the excavation side of cantilever walls below the excavation, σ_h' will increase until failure when circle AG is tangent to the failure criterion at point F. The horizontal effective stress can be computed as $\sigma_h' = K_p\sigma_v' = \frac{1+\sin(\phi)}{1-\sin(\phi)}\sigma_v'$ (i.e., the soil is the passive state of failure). It is important to note that because

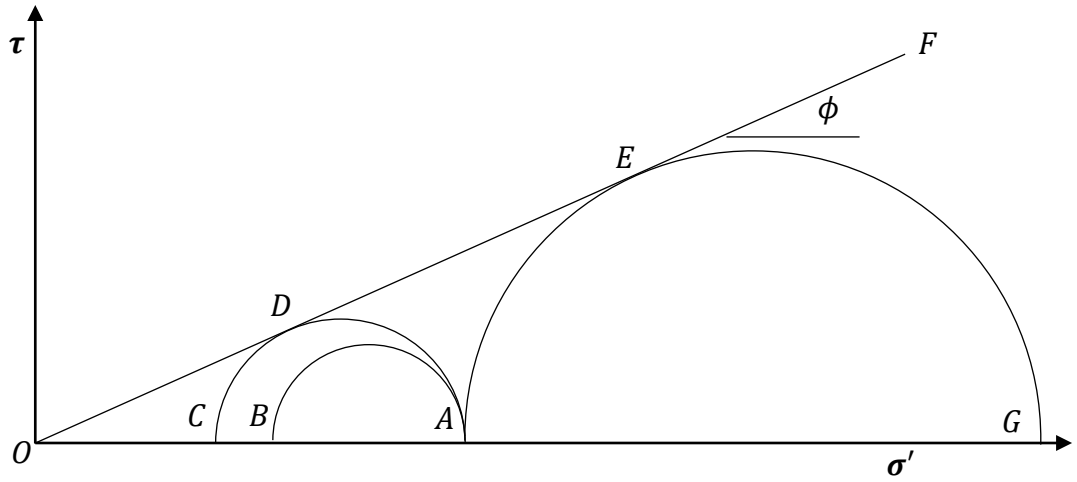

Figure 2.7 Rankine failure states for active failure (circle AC) and passive failure (circle AG). Line OF represents the Coulomb's failure line and points D and E represent failure plane for active and passive failure states, respectively.

Coulomb's upper-bound solution and Rankine's lower-bound solution are equal in the case of no wall friction, wall inclination, or backfill inclination, the true solution has been found for these conditions.

Since K_a and K_p are constants (assuming the friction angle is constant), applying the Coulomb/ Rankine model results in a linear stress distribution with depth on both the backfill and excavation sides of a cantilever retaining wall, shown in Figure 2.8. Since both the Rankine and Coulomb models were developed for the gravity walls, the active and passive pressures are assumed to increase to the end of the retaining wall. This assumption is not valid for flexible

cantilever walls, however, since force and moment equilibrium cannot simultaneously be satisfied under the pressure distribution in Figure 2.8.

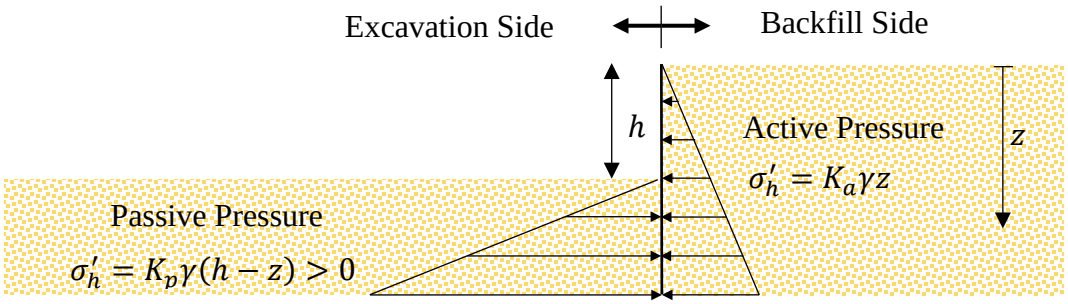

Figure 2.8. Assumed lateral earth pressure for flexible cantilever retaining walls according to Coulomb or Rankine theories. Note that for this assumed pressure distribution does not satisfy moment equilibrium.

To achieve both force and moment equilibrium, Bica and Clayton (1989) compiled a number of limit equilibrium solutions. The first of these solutions came from Engel (1903) suggested the net earth pressure distribution shown by Figure 2.9 based on experimental results, with a parabolic net pressure distribution below the excavation (Figure 2.9a) in force and moment equilibrium with the active earth pressure distribution (Figure 2.9b). Although Engel's method provides sufficient limit equilibrium, the model appears to have no theoretical or experimental basis and no explicit solution was provided, so the application of this method is questionable.

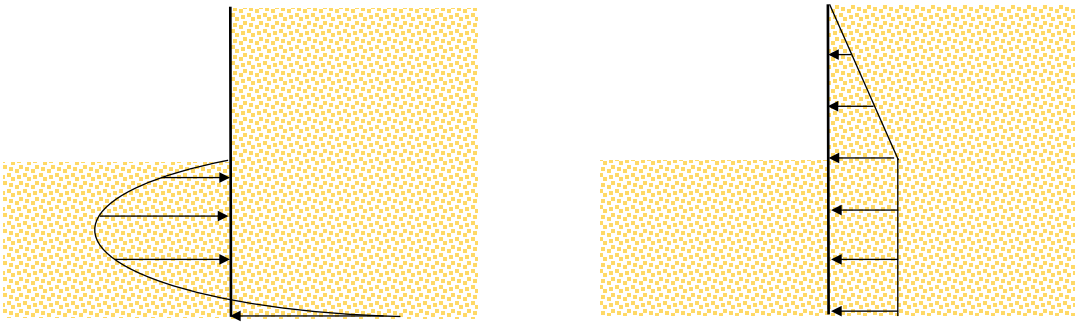

Figure 2.9. Engel's Method for net earth pressure (a) parabolic net pressure distribution below excavation (b) active pressure on backfill side of wall (after Bica and Clayton, 1989)

In light of the limitations of Engel's solution, a rectilinear solution was initially proposed by Krey (1932) and modified by many including King (1995), whose model is shown in Figure 2.10. The lateral earth pressure distribution above the excavation, i.e., for pressure distributions from $0 \leq z \leq h$, presented in this model is identical to that of the Rankine model, where lateral earth pressure, $\sigma'_{h,A}$, is equal to $K_a \gamma z$ toward the excavation. Below the excavation, however, King's model begins to deviate from the Rankine and Coulomb models as well as other rectilinear net pressure models. King's model assumes that below the excavation, the net pressure on the backfill side of the retaining wall decreases to zero at a depth of $z = h + x$. Below this point, the net pressure begins to increase in the direction toward the backfill up to maximum pressure, p_1 at $z = h + y$. Due to an overall rotation of the wall (counterclockwise in Figure 2.10), the net pressure distribution begins to decrease to value of zero at $z = h + y$. The net pressure then increases in the direction of the excavation to a value p_2 at the bottom of the retaining wall.

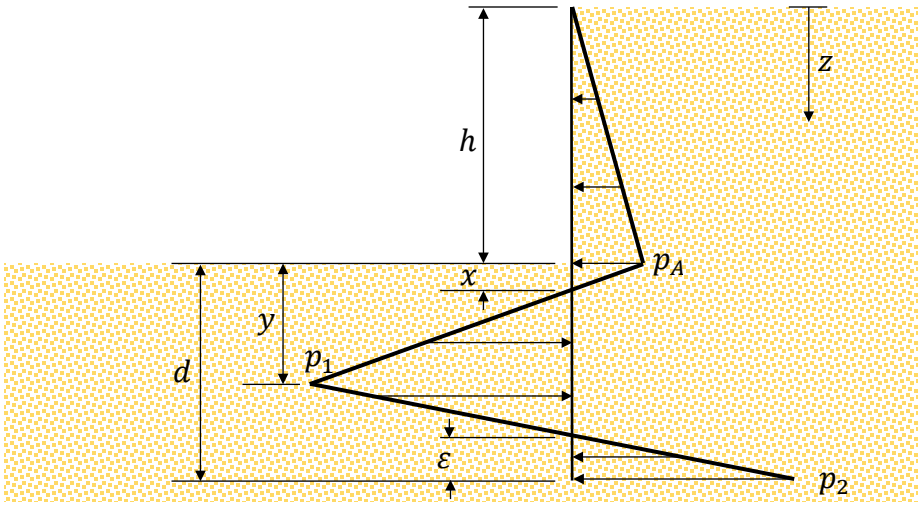

Figure 2.10. Rectilinear net pressure distribution first proposed by Krey (1932) and later modified by others including King (1998)

Several of the variables in Figure 2.10 can be solved using knowledge from previous methods and similar triangles. The value of p_A can be determined by making the assumptions as previous methods, where

$$p_A = K_a \gamma h \tag{12}$$

Through similar triangles, p_1 and p_2 can also be determined:

$$p_1 = p_A \frac{y - x}{x} \tag{13}$$

$$p_2 = \frac{\varepsilon p_1}{d - \varepsilon - y} \tag{14}$$

By solving forces in the horizontal direction and normalizing h, x, y and ε with respect to d, i.e., $h' = \frac{h}{d}, x' = \frac{x}{d}, etc.$, two equations can be determined with three unknowns using both force and moment equilibrium:

$$x' = \frac{y'[(1 - 2\varepsilon') - y'(1 - \varepsilon')]}{h'(1 - \varepsilon' - y') - y'^2 + (1 - 2\varepsilon')} \tag{15}$$

$$0 = [(1 - \varepsilon')h' + (1 - 2\varepsilon')]y'^2 + [(1 - \varepsilon)h'^2 - (1 - 3\varepsilon')]y' - [(1 - 2\varepsilon')h'^2 + (1 - 3\varepsilon')h'] \tag{16}$$

For a given normalized excavation height, h', and assuming an empirical value of $\varepsilon' = 0.35$ based off experimental data, y' and x' can be determined from Equations 15 and 16. This net pressure distribution was found to be in good agreement with centrifuge testing of a small-scale model (King 1995) and therefore appears to be the best method for quantifying lateral earth pressures due to soil self-weight for flexible cantilever retaining walls. As the method from King (1995) shows, the lateral earth pressures in the embedded portion of the wall near the bottom of

sheet pile are considerably more complex than the portion exposed to the excavation at the top of the pile where the method coincides with traditional Coulomb and Rankine theories.

An assumption from every method discussed in this section is that the soil is in a state of failure for earth pressure, either active or passive. In practicality, however, retaining walls obviously must be designed against failure, thus neither active nor passive earth pressures can fully characterize the entire pressure distribution along the wall. Figure 2.11 shows the earth pressure distribution on both sides of the wall taking into account for the actual movements of the retaining wall. Since the wall is designed with a significant factor of safety, wall movements will be limited, and the earth pressure distribution will deviate from the active/passive pressures to the at rest earth pressure, K_o. As was the case for the method from King (1995), the pressure distributions become significantly more complex as depth increases below the elevation of the excavation. Due to this complexity, the focus of this research will be on the portion of the

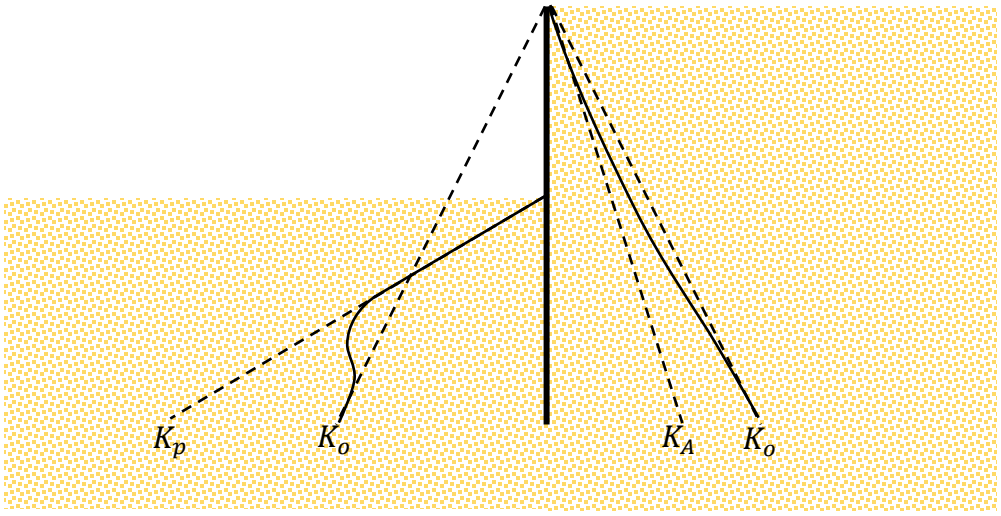

Figure 2.11. Stress distribution along a cantilever wall accounting for actual ground movements (after Atkinson 2007).

flexible cantilever retaining wall that is exposed to the excavation and just below excavation, where the actual earth pressure on the excavation side of the wall is in the passive failure condition, K_p, in Figure 2.11.

The movement of the walls described in Figure 2.11 is dependent on the flexibility of the wall. Terzaghi (1954) discussed that walls that are more flexible would have different properties than walls that are more rigid. This postulate was confirmed by small-scale testing by Rowe (1952). While Rowe (1952) and Terzaghi (1954) pertain to anchored walls, Bowles (1996) asserted that these flexibility dependencies are just as relevant for cantilever walls. Figure 2.12 shows the difference in the deflected shape of the walls depending on their flexibility. Figure 12a depicts a more flexible wall where only bending is present, and no rotation occurs. At some depth, a point of fixity is reached, and no net pressure or wall movement occurs below this depth. This scenario is commonly referred to as the "fixed-earth" support case (Rowe 1952; Terzaghi 1954; Bowles 1996). The corresponding bending moment is qualitatively shown with negative bending moments below the point of fixity. Conversely, Figure 12b shows a more rigid wall where minor

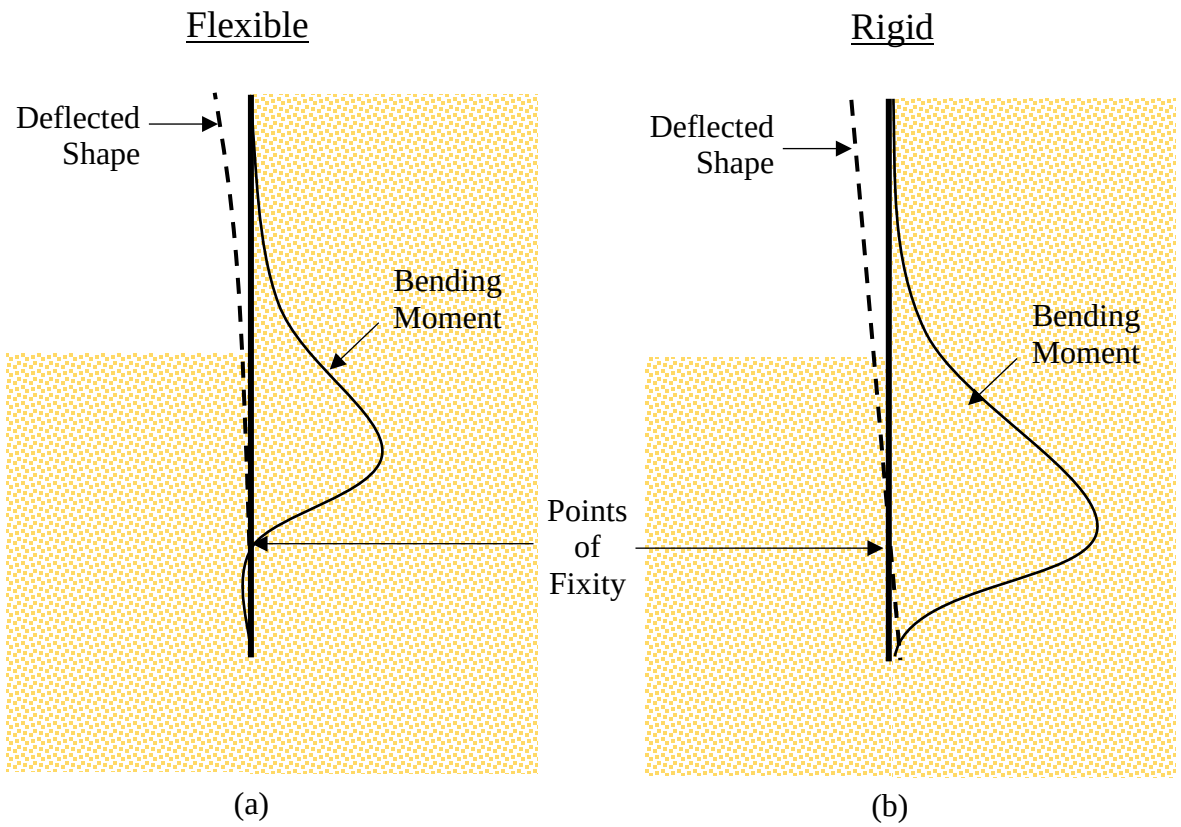

Figure 2.12. Effect of wall flexibility on the deflected shape and bending moment of (a) more flexible wall with fixed-earth support and (b) more rigid wall with free-earth support.

bending occurs and wall rotation dominates the overall movement. At some depth, a point of fixity is reached that acts as an axis of rotation. Below this point of rotation, wall movement and net pressure are present, unlike the flexible walls. This scenario is commonly referred to as the "free-earth" support case (Rowe 1952; Terzaghi 1954; Bowles 1996). The earth pressures presented in Figure 2.10 from King (1995) assume the free earth support.

Important similarities and differences can be observed between the fixed- and free-earth support scenarios. First, both methods assume identical earth pressures and bending moments on the backfill side of the wall above the elevation of the excavation since the deflections of the wall are assumed to be in the active state. Below the elevation of the excavation, however, the two assumptions diverge. For the fixed earth support, the maximum bending moment is both less in magnitude and shallower in location compared to the free-earth support. The lower magnitude of maximum moment is because the more flexible wall allows for greater wall movement. This wall movement allows the soil to reach the passive earth pressure condition at shallower depths, resulting in lower bending moments (Rowe 1952).

To quantify the relative flexibility of the cantilever retaining wall, Rowe (1952) proposed the dimensionless flexibility number, ρ, given as:

$$\rho = \frac{L^4}{EI} \tag{17}$$

where L is the full length of the sheet pile, E is the Young's modulus of the wall material, and I is the area moment of inertia of the sheet pile wall.

In addition to wall flexibility, the compressibility of the soil plays an important role in whether the cantilever wall will model the fixed- or free- earth support scenario. Soil with higher

compressibility or lower relative density require higher wall flexibility to achieve the fixed-support scenario (Rowe 1952). Together, the value of ρ and the compressibility/relative density of the soil determine whether the cantilever wall will behave as the free- or fixed-earth support scenario.

Up to this point, only loading due to the self-weight of the soil has been discussed. In many cases, however, significant surcharge loading on the backfill portion of the retaining wall is present. These surcharge loads can add substantial stresses to a retaining wall, so their effect must be properly quantified.

2.3 Retaining Walls under Surcharge Loading

In addition to the loading on the retaining wall due to self-weight, surcharge loading above the excavation is common and may contribute to significant pressures and bending moments in the retaining wall. Several different methods for quantifying the resultant lateral earth pressures from surcharge loading are discussed in the following section.

2.3.1 Elastic Solutions

Elastic methods to quantify lateral earth pressure due to surcharge loading involve the assumption that, while deformation will occur to the soil adjacent to surcharge loading and the retaining wall, no soil failure occurs. The method also assumes stresses are directly proportional to strains through constitutive equations (i.e., generalized Hooke's law). Most elastic methods pertaining to surcharge loads on retaining walls appear to be based on the original Boussinesq's solution for vertical stresses from point loads. Boussinesq's original solution is given by Equation 17.

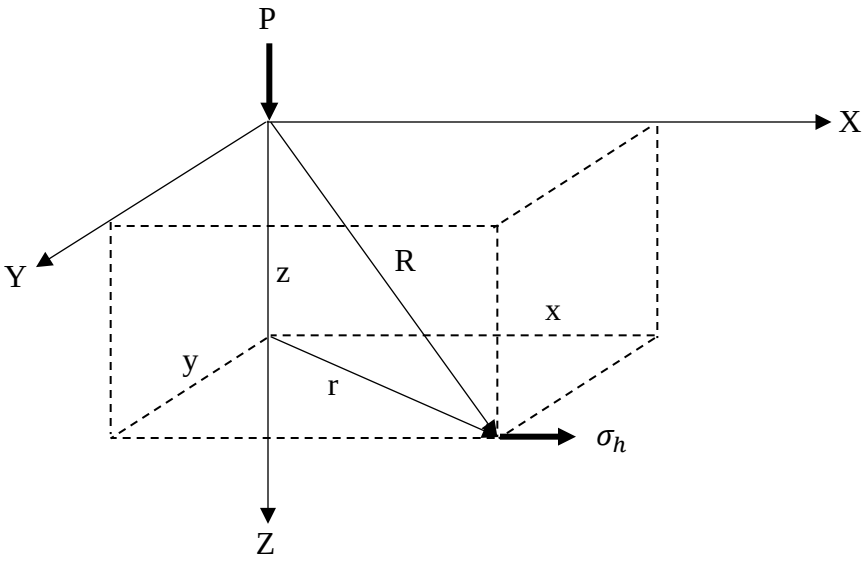

Figure 2.13. Boussinesq's solution for a point load on an elastic material.

$$\sigma_h = \frac{P}{2\pi}\left(\frac{3r^2 z}{R^5} - \frac{1-2\mu}{R(R+z)}\right) \tag{18}$$

where μ is the Poisson's ratio of the material under loading and other variables are defined in Figure 2.12. Equation 18 can then be applied along a vertical line to estimate to estimate the induced pressures applied to the imagined retaining wall. Boussinesq's solution can also be integrated to model strip loads and the value of P can be varied to model non-uniform surcharge magnitudes. Three such Boussinesq-based solutions will be presented here.

Poulos and Davis (1974) compiled several of these Boussinesq-based elastic solutions for modelling the effect of distributed loading on points at some depth and/or lateral distance away from the loading areas on a semi-infinite medium. Figure 2.13 depicts loading from (a) vertical loading, (b) horizontal (shear) loading, and (c) linearly varying vertical loading. The induced horizontal stresses from each of these distributed loading scenarios can be calculated using Equation 19a to 19c, respective to Figure 2.13a to 2.13c (The parameters of the equations are defined in Figure 2.14):

$$\sigma_{x,p} = \frac{q_v}{\pi}[\alpha - \sin(\alpha)\cos(\alpha + 2\delta)] \tag{19a}$$

$$\sigma_{x,q} = \frac{q_h}{\pi}\left[\ln\left(\frac{R_1}{R_2}\right) - \sin(\alpha)\sin(\alpha + 2\delta)\right] \tag{19b}$$

$$\sigma_{x,m} = \frac{m}{2\pi}\left[\frac{x}{b}\alpha - \frac{z}{b}\ln\left(\frac{R_1^2}{R_2^2}\right) + \sin(2\delta)\right] \tag{19c}$$

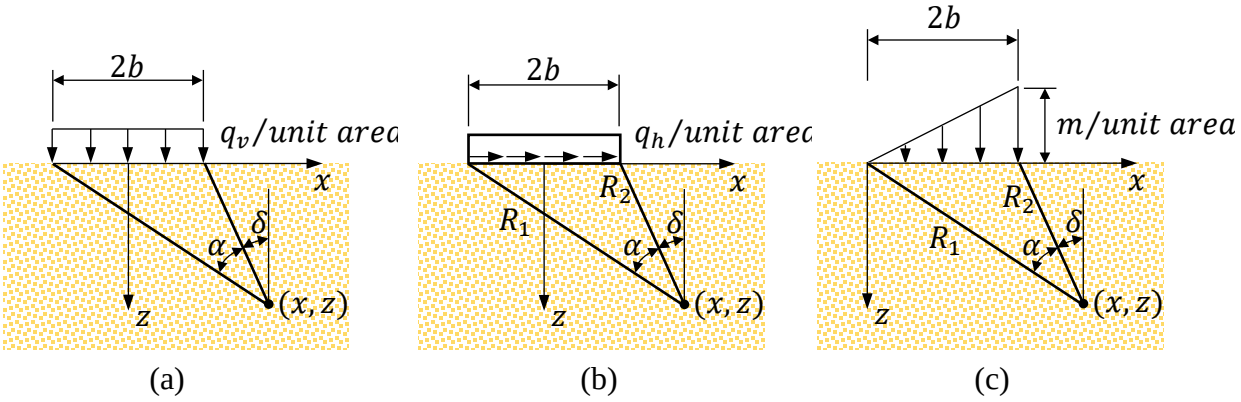

(a) (b) (c)

Figure 2.14. Schematic diagram of elastic solutions for (a) Uniform Vertical Loading (b) Uniform Horizontal Loading and (c) Vertical Loading Increasing Linearly (after Poulos and Davis 1974)

As was the case for the general Boussinesq's solution, Equation 19 can then be applied along a vertical line to estimate the induced pressures that the imagined retaining wall would feel. Because these solutions are intended for semi-infinite space, the assumed conditions for lateral confinement are different than that of a retaining wall, which may lead to significant errors. To get the complete lateral earth pressure, accounting for both the self-weight of the soil and the surcharge, Jarquio (1981) stated that the induced horizontal stress from elastic solutions can then simply be added to the lateral earth pressure from self-weight via Coulomb or Rankine theories (see the previous section for full discussion).

For the case of uniform vertical surcharge (i.e., Equation 19a), several experimental studies have been performed to test the validity of the application of elastic solutions. Results from Spangler

(1956) produced results with values twice than that from Boussinesq's solution for uniform vertical surcharge loads given by Equation 19a. Thus, these results suggest the induced pressures from the vertical surcharge be modified by a factor of two:

$$\sigma_h = \frac{2q_v}{\pi}(\beta - \sin(\beta)\cos(2\alpha)) \tag{20}$$

The validity of implementing the modifying factor in Equation 20 has seen mixed opinions amongst researchers. Terzaghi (1954) suggests that the doubled magnitude in pressure can be explained by the rigidity of the wall producing a mirroring effect of a load placed in front of the wall. Bowles (1996) dismissed this explanation, saying that the mirror load described by Terzaghi (1954) would effectively cancel the pressures from the real load, not double it. Bowles (1996) suggested that the cause of the high observed stress magnitudes may be due to limitations in the setup and sensors at the time of the experiment and parameters like Poisson's ratio and state (dense or loose) will have a significant effect on the induced lateral earth pressure from surcharge loading. In light of these mixed conclusions from previous work, the application of elastic solutions appears questionable.

More recently, Wang (2005) developed elastic solutions to quantify the effects of horizontal and vertical surcharge loads while also accounting for cross-anisotropy of the backfill. The solutions include uniform, linearly varying, and non-linearly varying surcharges that can be superimposed to account for more complex surcharge loading. Although these solutions allow for quantifying a wide variety of surcharges, the process of determining the induced stresses along the wall are complex, cumbersome, and require the input of many elastic parameters, many of which are well beyond the scope of most geotechnical investigations. In light of these limitations, the practical use of these solutions from this study seem infeasible and are beyond the scope of this thesis.

Although elastic models provide simple equations for quantifying the effect of surcharges on retaining walls, there are several shortcomings of applying elastic solutions to yielding retaining walls. First, elastic methods fail to account for soil strength (ϕ) and they do not consider the range of deformation experienced by the soil structure when the surcharge is applied (i.e, active or passive - Steenfelt and Hansen 1981). In addition, applying both the elastic solution for the surcharge and Coulomb's or Rankine's theory for the self-weight of the soil might not be compatible, since the former assumes the soil failure has not occurred, yet the latter assumes soil is at failure. Even small rotations (horizontal deflections of 0.05% to 0.2% of the total wall height for coarse-grained soils) can provide the necessary deformations to reduce confinement to the point of active failure (Naval Facilities Engineering Command 1982)

By applying elastic theory in this way, the magnitude of the resultant force of the lateral earth pressure due to the surcharge at a depth can be greatly overestimated (Steenfelt and Hansen 1981). Similarly, for surcharge occurring at some distance from the yielding retaining wall, the theoretical location of the resultant force tends to be shallower than the actual resultant location. This is because elastic solutions predict lateral pressures due to the surcharge immediately below the top of the retaining wall, regardless of the surcharge-retaining wall spacing (Steenfelt and Hansen 1983). In large-scale experimental testing investigating the effect of surcharge loading on retaining walls (Spangler 1956), there was a distinct lack of surcharge contribution at shallow depths for surcharges placed at a distance from the retaining wall, something not predicted by elastic solutions. Georgiadis and Anagnostopoulos (1998) also confirmed the inaccuracies of elastic solutions in a study where elastic, approximate, and Coulomb-based solutions were compared via a small-scale experimental model. Results showed that elastic methods greatly overestimated lateral earth pressures from vertical surcharges. This will be discussed in detail in

the Plastic Limit Equilibrium Solutions section. Ultimately, adding lateral earth pressures due to surcharge via elastic methods to the pressures from self-weight via Coulomb or Rankine theory for flexible walls can result in potentially unsafe or uneconomical designs, so a different approach is needed.

2.3.2 AASHTO Approximate Solution

The report from Berg et al. (2009) (based on the AASHTO LRFD Bridge Design Specifications) describes approximate methods for modelling the effects of complex surcharge loading on retaining structures. Although these methods were originally formulated for the internal/external stability design of an MSE wall, it is assumed that these can also be applied to other types of walls. The method includes two independent solutions, one for vertical loads and another for horizontal loads. These solutions are then superimposed onto traditional active earth pressure solutions from Coulomb's or Rankine's theories to ultimately quantify the combined horizontal earth pressure along the wall from both the surcharge and self-weight of the soil.

The first solution, shown in Figure 2.14, quantifies the effects of vertical surcharge loads. The induced vertical stress from the vertical load, $\Delta\sigma_v$, is assumed to be maximum at the ground surface and attenuate geometrically at a constant rate of 2:1 with the depth below the ground surface. The induced horizontal stress along the depth of the retaining wall can be computed as:

$$\Delta\sigma_H = K_A \Delta\sigma_H = K_A \left(\frac{Q_v}{D_1}\right) \tag{21}$$

where K_A is the active earth pressure coefficient according to traditional Coulomb and Rankine theories, Q_v is the vertical surcharge load magnitude, D_1 is the effective width of the vertical surcharge = ($b_f + z \; for \; z \leq z_1$ and $\frac{b_f+z}{2} + d \quad for \; z < z_1$), z_1 is the depth where effective

width intersects retaining wall, b_f is the contact width of the surcharge on the ground surface, and d is the distance from the retaining wall to the resultant of Q_v.

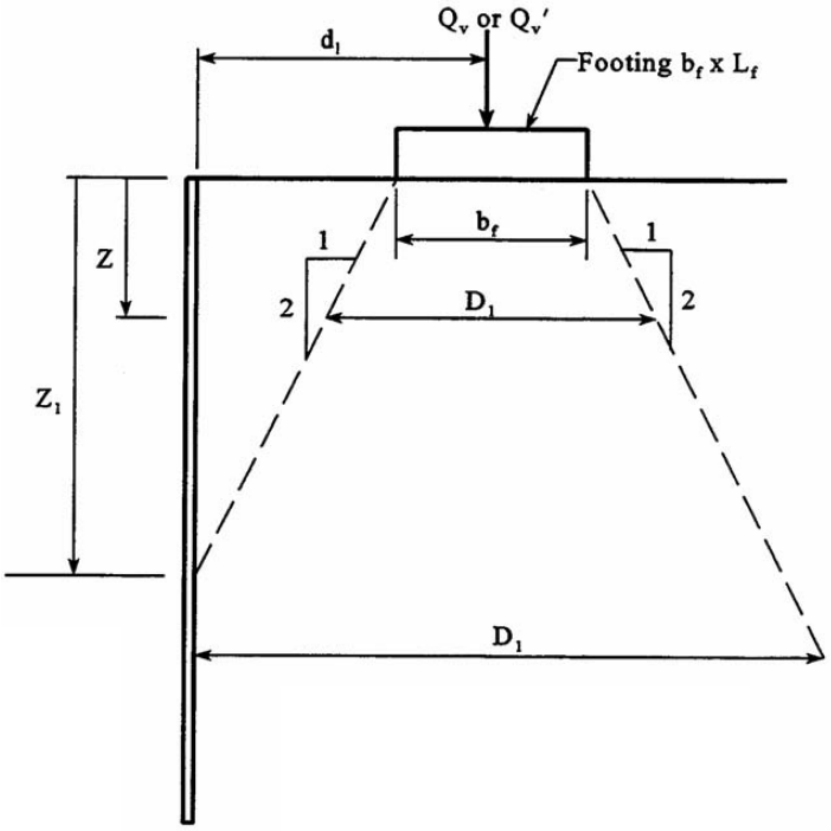

Figure 2.15. AASHTO approximate method for quantifying the effects of distanced vertical surcharges on the lateral earth pressures of retaining walls. (from Berg et al. 2009)

To model the effects of applied horizontal loads, the solution illustrated by Figure 2.15 can be employed. The induced horizontal stress from the horizontal loads, $\Delta\sigma_H$, is assumed to have a maximum value at the ground surface and have a linearly decreasing magnitude with depth. For a given depth, z, the induced stress can be computed as:

$$\Delta\sigma_H = \begin{cases} \left(1 - \frac{z}{l_2}\right)\Delta\sigma_H max & for\ z \le l_2 \\ 0 & for\ z > l_2 \end{cases} \quad (22)$$

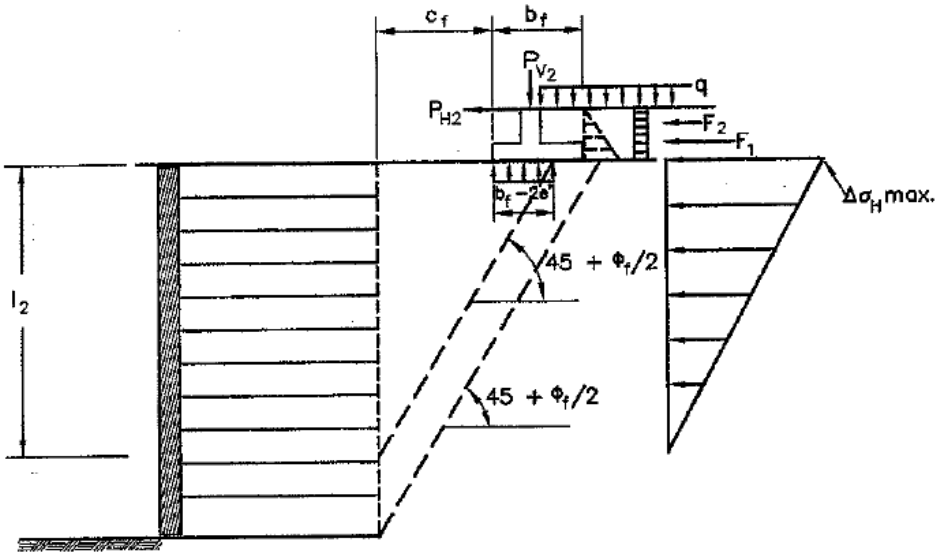

Figure 2.16 Approximate method for quantifying the effects of distanced horizontal surcharges on the lateral earth pressures of retaining walls (from Berg et al. 2009).

where l_2 is the depth that applied horizontal forces influence $\left(= \left(c_f + b_f - 2e'\right) \tan\left(45° + \frac{\phi}{2}\right)\right)$, c_f is the distance between the retaining wall and applied loads, b_f is the effective width of surcharge area, e' is the eccentricity of load on surcharge, ϕ is the friction angle of backfill, $\Delta\sigma_H max = \frac{\Sigma F}{l_2} = \frac{\Sigma(P_{H2}+F_1+F_2)}{l_2}$, P_{H2} is the lateral force due to superstructure or other concentrated lateral loads, F_1 is the lateral force due to earth pressure, and F_2 is the lateral force due to traffic surcharge.

These two methods presented by Berg et al. (2009) have several shortcomings. First, it is unclear how these solutions were formulated. The angle of $45° + \frac{\phi}{2}$ from the horizontal direction in the solution appears to be an application of Coulomb's theory where an inclination of $45° + \frac{\phi}{2}$ produces the maximum thrust. However, this inclination only produces the maximum thrust when the surcharge is effectively infinite; i.e., $b_f \geq \tan\left(45 + \frac{\phi}{2}\right) L$, and there is no distance between the surcharge loading and the retaining wall, i.e., $c_f = 0$ (L is the height of the retaining

wall). If even one of these conditions is not fulfilled, the maximum thrust will occur at an inclination other than $45° + \frac{\phi}{2}$. In addition to the lack of theoretical basis of the method, both methods assume that the induced stresses from the surcharge occur immediately at the top of the retaining wall, regardless of the distance between the surcharge and the retaining wall. Steenfelt and Hansen (1983) previously discussed these seemingly illogical assumptions and suggested that a plasticity-based, limit equilibrium approach may be more appropriate.

2.3.3 Plastic Limit Equilibrium Solutions

An alternative to the theory of elasticity applied in the solutions in the previous section is the theory of plasticity. Whereas elastic solutions assume no failure and deformation, plasticity-based limit equilibrium solutions assume failure, but not deformation. Coulomb's and Rankine's theories are examples of methods based on plasticity theory. As stated earlier, the straight-line failure surfaces assumed in Coulomb's theory results in insignificant deviations in the active condition when compared to curved failure surface models. A major advantage to using Coulomb's theory is that both the surcharge and the self-weight of the soil are directly incorporated into the final solution, unlike elastic methods where superposition of the surcharge and self-weight is required. Two plasticity-based solutions for quantifying the effect of vertical surcharge on lateral earth pressures on retaining walls will be presented here.

For an infinite, uniform, vertical surcharge acting on the backfill portion of the retaining wall, the critical inclination angle and ultimately the active earth pressure coefficient is identical to that of the self-weight only condition. This is because the contribution to the thrust from the self-weight and the contribution from the surcharge are identically related to the inclination angle, α. When solving for the maximum thrust by setting the derivative of thrust, P with respect to α, to zero;

that is $\frac{dP}{d\alpha} = 0$, the unit weight, γ, depth, z, and vertical surcharge, q_v, can be eliminated, identical to Equation 4. This means the critical value for α, α_c, is again only dependent on the friction angle, ϕ, and the wall-soil interfacial friction angle, δ (more information can be found in Appendix B).

Motta (1994) modified Coulomb's wedge-based theory for a vertical surcharge, q_v, of infinite extent situated some distance, d, from the retaining wall, as shown in Figure 2.16. The thrust, P, can be computed as:

$$P = \frac{\left(\frac{1}{2}\gamma z^2 f(\alpha) + q_v(zf(\alpha) - d)\right)\sin(\alpha - \phi)}{\cos(\phi + \delta - \alpha)} = \left(\frac{1}{2}\gamma z^2 f(\alpha) + q_v(zf(\alpha) - d\tan(\alpha)\right) g(\alpha) \quad (23)$$

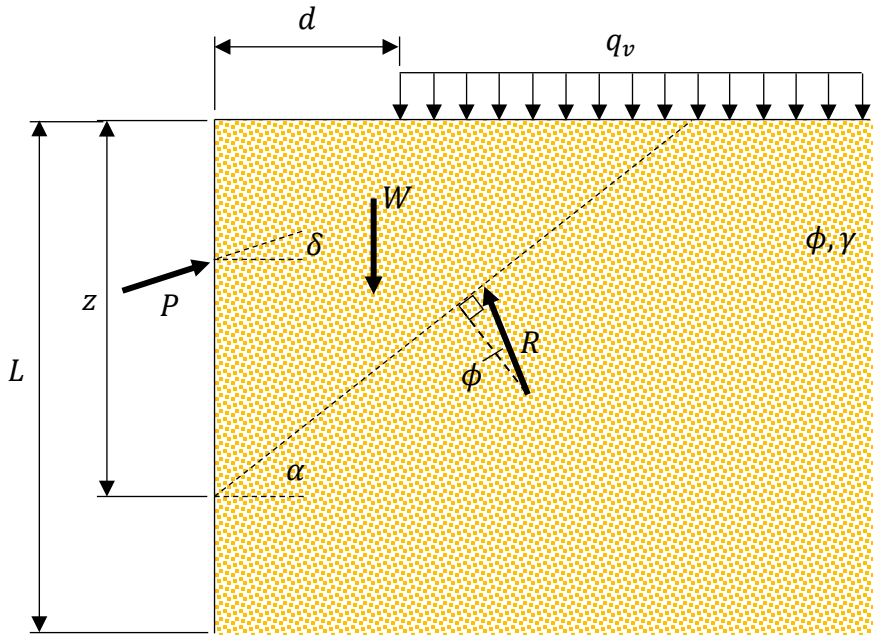

Figure 2.17. Schematic of Coulomb-based solution for distanced, infinite vertical surcharge on backfill portion of retaining wall (after Motta 1994)

where $f(\alpha) = \frac{1}{\tan(\alpha)}$ and $g(\alpha) = \frac{\sin(\alpha-\phi)}{\cos(\alpha-\phi-\delta)}$.

Equation 23 can also be rearranged into a more traditional form:

$$\mathrm{P} = \frac{1}{2}\gamma \mathrm{z}^2 \mathrm{K}_{\mathrm{a},\gamma\mathrm{q}} \tag{24}$$

where $K_{a,\gamma q}$ is the active earth pressure coefficient that takes into account both the self-weight of the soil and the surcharge. This coefficient yields:

$$\mathrm{K}_{\mathrm{a},\gamma\mathrm{q}} = \left[\mathrm{f}(\alpha)\left(1 + \mathrm{n}_\mathrm{q}\right) - \mathrm{n}_\mathrm{q}\lambda\right]\mathrm{g}(\alpha) \tag{25}$$

where $\mathrm{n}_\mathrm{q} = \frac{2\mathrm{q}}{\gamma \mathrm{z}}$ and $\lambda = \frac{d}{z}$.

The contribution of the surcharge to the thrust contains two terms, each with a different dependence on α: $f(\alpha)g(\alpha)$ and $g(\alpha)$. This contribution has a profound effect when finding α_c in that the presence of two terms no longer allows the reduction of γ, z, and q_v as was the case for Equation 5. Consequently, α_c is dependent on ϕ, δ, γ, z, and q_v. In addition, if d is large relative to z so that $\tan(\alpha_c) > \frac{d}{z}$, the critical failure surface lies outside the extent of the surcharge and α_c is only dependent on ϕ and δ (see Equation 10). Considering this, the thrust should be determined via a piecewise function:

$$\mathrm{P} = \max\begin{cases} \left[\frac{1}{2}\gamma \mathrm{z}^2 \mathrm{f}(\alpha) + \mathrm{q}_\mathrm{v}(\mathrm{zf}(\alpha) - \mathrm{d})\right]\mathrm{g}(\alpha) & \text{for } \tan(\alpha) < \frac{\mathrm{d}}{\mathrm{z}} \\ \frac{1}{2}\gamma \mathrm{z}^2 \mathrm{f}(\alpha)\mathrm{g}(\alpha) & \text{otherwise} \end{cases} \tag{26}$$

Greco (2006) introduced a similar model to Motta (1994), except with the distinction that the vertical surcharge, q_v, is only of a finite width, b, as shown in Figure 2.17. The surcharge has a magnitude, q_v, an application width, b, and has a distance from the retaining wall, d. The active thrust, $P(\alpha, z)$, is in equilibrium with the weight, surcharge and reaction for a given depth, z, is by the following piecewise function:

$$P = \max \begin{cases} \left[\frac{1}{2}\gamma z^2 f(\alpha) + q_v b\right] g(\alpha) & \tan(\alpha) < \frac{d+b}{z} \\ \left[\frac{1}{2}\gamma z^2 f(\alpha) + q_v (z f(\alpha) - d)\right] g(\alpha) & \frac{d+b}{z} < \tan(\alpha) < \frac{d}{z} \\ \frac{1}{2}\gamma z^2 f(\alpha) M(\alpha) & \tan(\alpha) > \frac{d}{z} \end{cases} \quad (27)$$

where $f(\alpha) = \frac{1}{\tan(\alpha)}$ and $g(\alpha) = \frac{\sin(\alpha-\phi)}{\cos(\phi+\delta-\alpha)}$.

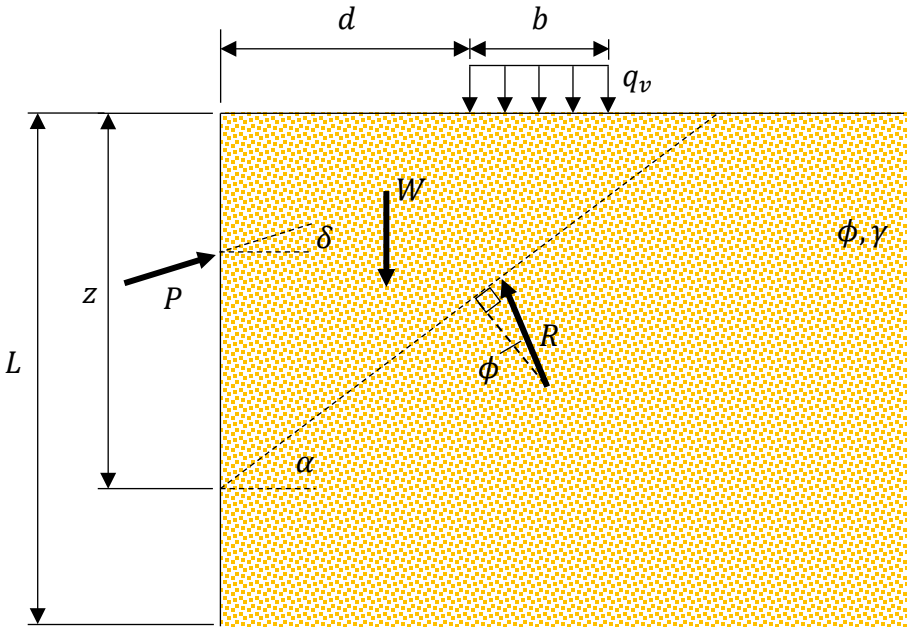

Figure 2.18. Schematic of Coulomb-based solution for distanced, finite vertical surcharge on backfill portion of retaining wall (after Greco 2006)

The piecewise function for $P(\alpha, z)$ is checked for all values of α between ϕ and 90° to find the maximum thrust for a given z, $S(z) = \max[P(\alpha, z)]$. By repeating the process for all depths with a small depth increment, the lateral earth pressure is equal to the numerical differentiation of $S(z)$ with respect to z, or $\frac{\partial S(z)}{\partial z}$.

Georgiadis and Anagnotstopoulos (1998) compared the process proposed by Motta (1994) and Greco (2006) with both elastic solutions (Jarquio 1981) and approximate methods (Cernica 1995

and Beton Kalender 1983) using a small-scale experimental model. A vertical surcharge at a distance from the wall, modelling a strip load, was first applied to the backfill of a cantilever sheet pile wall in dry sand. Sand was then removed in 5-cm steps on the side opposite to the surcharge and bending moments were measured via several strain gauges along the depth of the sheet pile wall. The results from this research found that the maximum bending moment predicted by elastic methods was over five times larger than the observed results. The predicted maximum bending moment from Coulomb's theory, conversely, had a difference of less than 20% of the observed value. Although one approximate method had similar differences between predicted and observed moments, the applicability of this method is questionable since the method lacks any scientific foundation and may not be accurate for conditions other than those present in the experimental model.

As this section has discussed, plasticity-based limit equilibrium solutions are more applicable than those based on elasticity for backfill portions under active failure conditions subjected to vertical surcharge. Because of this, a method based on plasticity is proposed for more complex surcharges including horizontal loading and those from applied moments.

2.4 Small-Scale Retaining Wall Models

Part of this research involves simulating the full-scale Zoo Interchange noise wall prototype with a small-scale experimental model. However, not every effect cannot be properly simulated in the small-scale model and the model itself will have effects that are not present in the prototype. These different effects will be addressed and discussed here.

2.4.1 Determination of Small-Scale Model Dimensions

To generalize the results from experimental testing, several considerations need to be addressed with respect to scale and boundary effects. The dimensions and boundary conditions of the small-scale model will first be discussed. The dimensionless parameters chosen for the experimental testing will then be justified.

Retaining wall prototypes like the system present at the Zoo Interchange are modeled in two dimensions as a cross-section since the width of the wall is generally much greater than the excavation height and is therefore treated as infinite. This also assumes the system behaves with plane strain conditions, as deformations along the width of the wall parallel to the wall face are approximately zero. In the case of small-scale model, however, the system cannot be immediately treated as a two dimensional system since the ratio between the width and height of the active failure wedge is much smaller compared to the prototype. Figure 2.19 shows a simplified schematic of the small-scale retaining model in three dimensions. Here the active

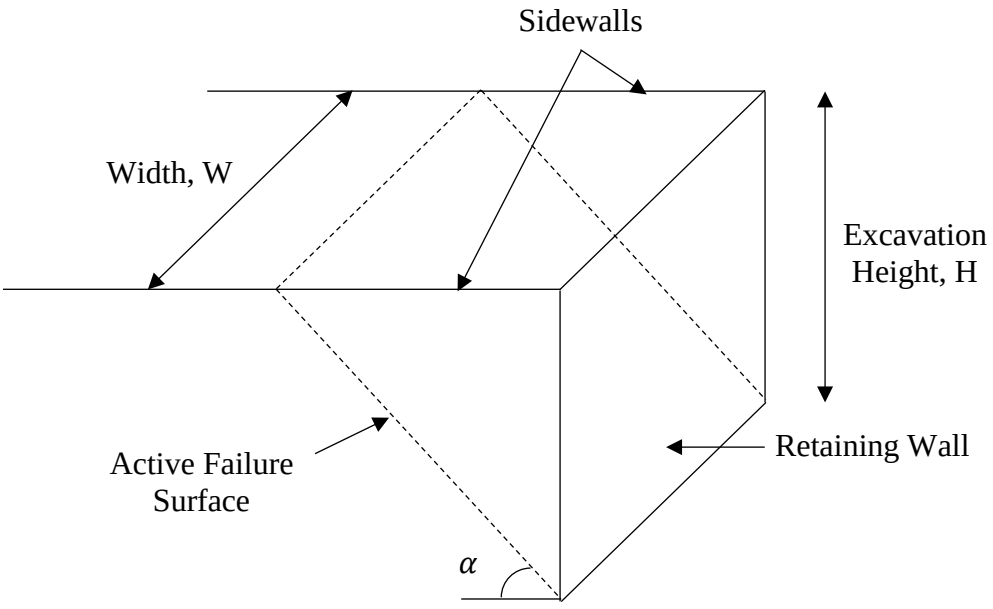

Figure 2.19. Simplified schematic of a retaining wall model in three dimensions.

wedge is assume to originate at the excavation level, so the height of the active wedge is equal to the excavation height.

Two forces act on the retaining wall in the horizontal direction: the active thrust, F_{active}, in the direction toward the retaining wall and a resistive force from friction from both side walls, $F_{friction}$, in the direction away from the retaining wall. These forces can be calculated as:

$$F_{active} = \frac{\gamma K_a H^2 W}{2\tan(\alpha)} \tag{28}$$

$$F_{friction} = \frac{\gamma K_o H^3 \tan(\delta_{sw})}{3\tan(\alpha)} \tag{29}$$

where K_o is the at-rest earth pressure coefficient and K_a is the active earth pressure coefficient, and other variables defined in Figure 2.19. Summing these forces in the horizontal direction, the actual force acting on the retaining wall is $F_{actual} = F_{active} - F_{friction}$. When no sidewall friction is present, $F_{actual} = F_{active}$ and the retaining wall can be treated as two-dimensional.

Figure 2.20 shows the effect of W/H for the wall on F_{actual}/F_{active} when $\phi = 31°$ and the retaining wall was assumed frictionless (i.e., $\alpha = 45° + \frac{\phi}{2}$). Several values of δ_{sw} are plotted to show the effect of the sidewall roughness. As Figure 2.20 shows, for large values of W/H, the boundary effect of the sidewall become negligible (i.e., $F_{actual}/F_{active} \approx 1$) no matter the value of δ_{sw}. This represents the case for the prototype and here the problem can be treated as two-dimensional. However, for the case of the small-scale model, where the ratio between W and H is smaller, the boundary effects of the sidewall may become significant depending on the value of δ_{sw}.

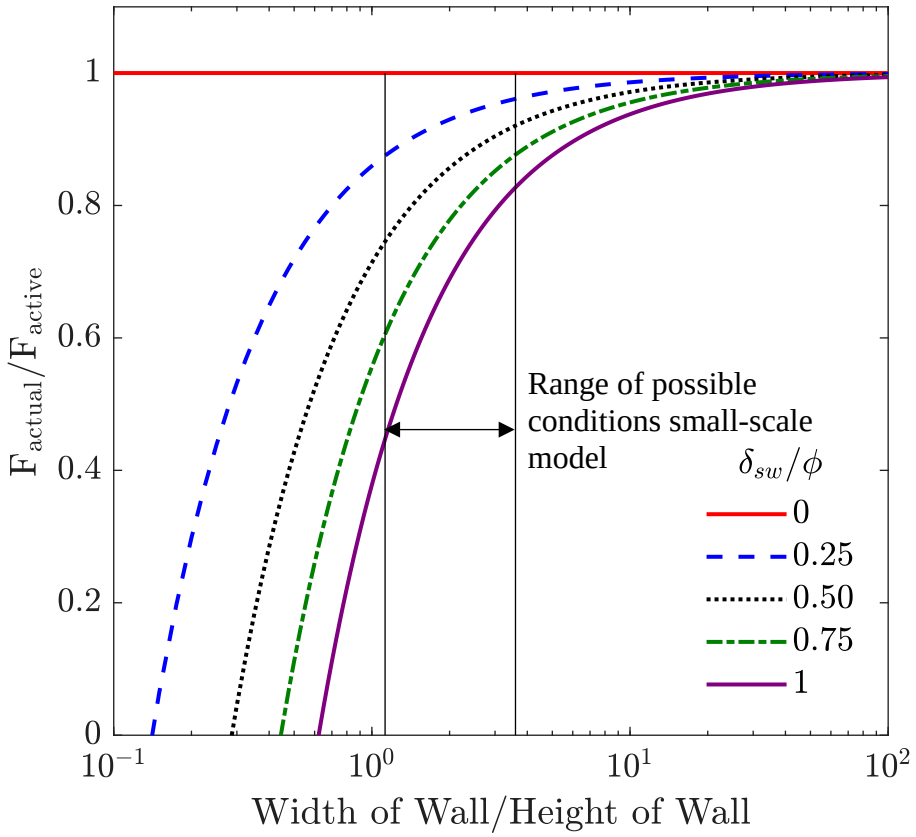

Figure 2.20. Effect of the width-to-height ratio of the retaining wall on the influence of sidewall friction resisting the thrust from the active failure wedge.

To reduce the influence of sidewall friction, two considerations were made: the width-to-height ratio were chosen to be greater than one, and the sidewalls were made of smooth material. The wall was chosen to be 45 cm wide with an excavation height of 12.5 cm, resulting in $W/H = 3.6$. This width to height ratio was chosen to balance the feasibility of testing (filling of the model was done by hand) and mitigating adverse stress effects the small-scale model discussed in Section 2.4.3. Note that the actual height of the failure wedge may range between the excavation height and the full length of the wall, L, so the lower bound of $W/H = 1.125$ is also plotted.

In addition to the consideration of retaining wall dimensions, the value of δ_{sw} was reduced by adding a layer of Teflon to either sidewall. The value of the interfacial friction between Teflon and sand was investigated by Leonards (1965). Based on the results from Leonards (1965), the value of δ_{sw} for this can be estimated as $0.25 \cdot \phi$. With the values of both the minimum value of W/H and an estimate for δ_{sw}, the value for F_{actual}/F_{active} for the small-scale model can be estimated between 0.88 and 0.96, depending on the height of the wedge. Based on these results, slight reductions to lateral pressure and corresponding bending moments can be expected.

2.4.2 Scaling and Similarity

In order to generalize the results of the small-scale model testing, the important physical parameters used in testing must be made dimensionless to have as much similitude as feasible between the small-scale model and the full-scale prototype. Figure 2.21 illustrates the pertinent parameters related to the noise wall-retaining wall system in this research. These parameters are defined as follows: (1) a is the moment arm of the resultant load related to wind, (2) b is the width of the surcharge, (3) d is the distance between the surcharge and the retaining wall, (4) H is the excavation height, (5) q_h is the magnitude of the horizontal surcharge from wind loading,

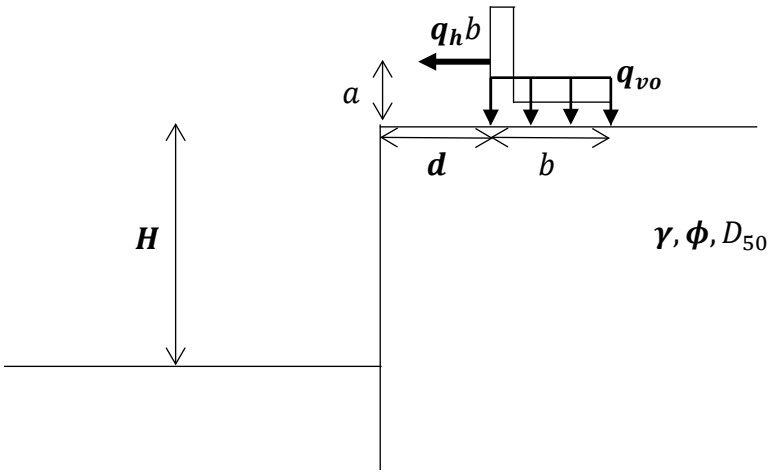

Figure 2.21. Schematic showing the parameters pertinent to the noise wall–retaining wall system used in this research. **Bolded** parameters indicate those chosen for dimensional analysis.

(6) q_{vo} is the vertical surcharge magnitude from dead load of the noise wall, (7) γ is the unit weight of the soil, (8) ϕ is the friction angle of the backfill, and (9) D_{50} is the particle diameter that 50% of the soil's mass is larger than.

Butterfield (1998) provides guidance on performing dimensional analysis, where the minimum number of dimensionless groups, N, is to be determined based on the minimum number of independent primary dimensions, m, and number of variables, n. Based on the variables above, $m = 2$ (Force and Length are the two independent primary dimensions) and $n = 9$, as there are nine variables listed above. From these values, the number of dimensionless groups can be calculated as $N = n - m = 7$ dimensionless groups. These groups are: $\frac{a}{H}$, $\frac{b}{H}$, $\frac{d}{H}$, $\frac{D_{50}}{H}$, ϕ, $\frac{q_{vo}}{\gamma H}$, and $\frac{q_h}{q_{vo}}$.

Of these seven dimensionless parameters, four were chosen for similarity for this research: $\frac{d}{H}$, $\frac{q_{vo}}{\gamma H}$, $\frac{q_h}{q_{vo}}$, and ϕ. The first of these parameters, $\frac{d}{H}$, relates a geometric term from both the noise wall and the retaining wall. Both parameters increase between the model and prototype, so geometric similarity has been achieved. Next, the magnitude of the vertical surcharge from the dead load, q_{vo}, can be related to the vertical effective stress at the excavation level (in this solution we assume dry conditions), γH, to form the dimensionless parameter $\frac{q_{vo}}{\gamma H}$. Since both quantities increase from the model to the prototype, stress similitude has been achieved.

The magnitude of the horizontal surcharge due to the wind load, q_h, was treated differently than the previous two parameters. Instead of relating q_h to a quantity related to the retaining wall, q_h was related to q_{vo}. This is because the ratio $\frac{q_h}{q_{vo}}$ is related to both the shearing loading of the noise wall in the horizontal direction and the moment effect in the vertical direction. In the horizontal

direction, $\frac{q_h}{q_{vo}}$ is equivalent to the total force between the noise wall and the underlying in the tangential direction to the total force in the vertical direction. This ratio cannot exceed the static friction coefficient between the noise wall and underlying soil or sliding failure will occur. In the vertical direction, $\frac{q_h}{q_{vo}}$, is related to the applied moment. This moment is equal to $q_h a$, with an eccentricity equal to $\frac{q_h a}{q_{vo}}$. The value of a was kept constant throughout testing but the eccentricity was altered by changing the value of $\frac{q_h}{q_{vo}}$, ultimately causing a larger moment effect.

The friction angle, ϕ, is the final parameter of interest for the dimensional analysis. Being an angle, ϕ, already is dimensionless and therefore requires no relation with any other parameter. Though this material was not intentionally varied in testing, the actual value of ϕ varied due to dilation effects discussed in the next section.

Three dimensionless parameters were not investigated for this research, $\frac{a}{H}$, $\frac{b}{H}$, and $\frac{D_{50}}{H}$. The first of these parameters $\frac{a}{H}$ is related to the applied moment and ultimately the linearly varying component of the vertical surcharge. However, the applied moment also varies with $\frac{q_h}{q_{vo}}$, so this parameter can be used to test the effect of both horizontal surcharge and the applied moment. The next parameter, $\frac{b}{H}$, is related to the width of the surcharge. This parameter was ignored since this parameter only slightly affects the distribution and magnitude of induced stresses on the wall from the surcharge. Finally, the parameter $\frac{D_{50}}{H}$ is related to the grain size distribution of the backfill. This parameter was ignored because for both the small-scale and large-scale case, the value of this parameter is very small. Because of the small value of $\frac{D_{50}}{H}$ for both cases, the sand can be treated as a continuum for the purpose of design.

2.4.3 Stress Variation and Dilation Effects

The final aspects of small-scale retaining wall models that relates to dimensional analysis are the limitations due to the small stress variation and presence of high dilation. These limitations could have been eliminated by using a model in a centrifuge (similar to that of King 1995 and others), but instead were mitigated and considered when interpreting and generalizing results.

The first of these limitations is related to the small stress variation in the model as compared to those of the prototype. At the top of the retaining wall, the stress is zero in every direction. At the bottom of the retaining wall, the stress is $\gamma L = \rho g L$ in the vertical direction, where γ is the unit weight of the soil, L is the length of the retaining wall, ρ is the density of the soil and g is the acceleration due to gravity. As Figure 2.22 shows, the range of stresses present in the model (red box) is significantly narrower compared to that of the prototype (green box). One method researchers have addressed this issue in the past is to run centrifuge testing, effectively increasing the value of g to something greater than that of the normal value of 9.81 m/s^2 (King 1995). This in turn allows for the same variation in stress variation for shorter wall lengths. For this research, however, a 1g model was used so effects of the lack of stress variation present in the model is not present in the prototype.

One such limitation due to the lack of stress variation in the model is the effect of dilative tendencies of soils at low effective stresses. This limitation in small-scale retaining walls has been identified and discussed by several researchers by several researchers including Bolton

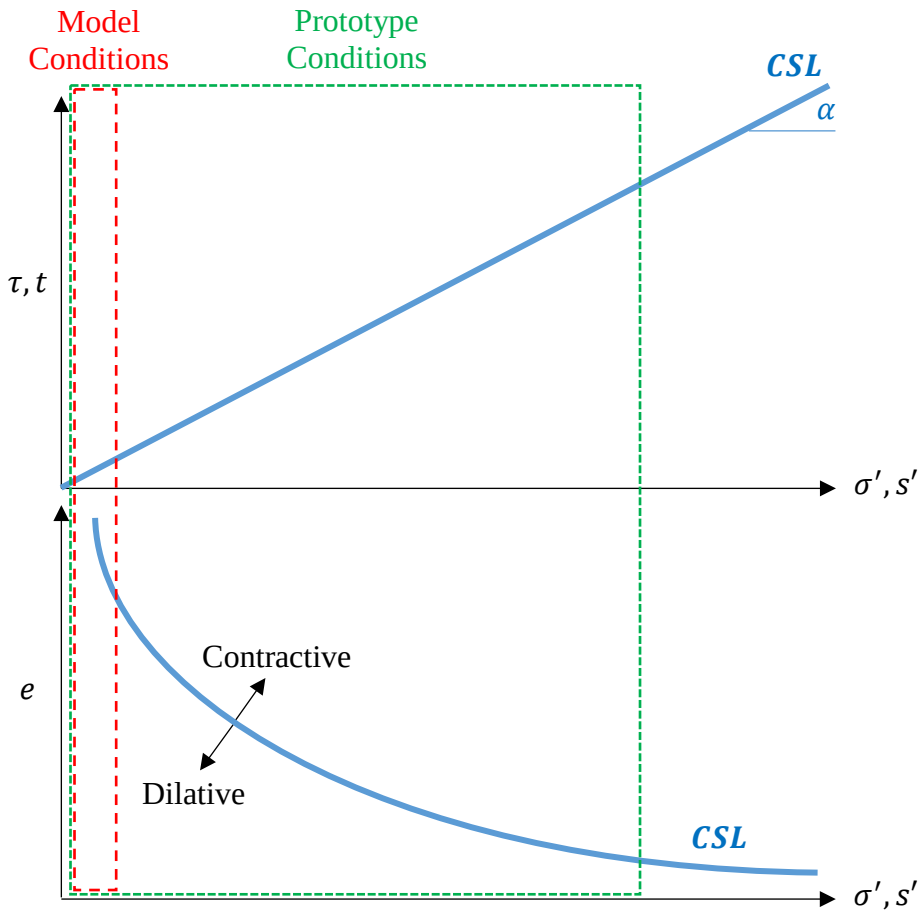

Figure 2.22. Difference in stress variation and dilatancy for the model conditions compared to the prototype conditions. $s' = (\sigma_1' - \sigma_3')/2$ and $t = (\sigma_1 - \sigma_3)/2$

(1985). Bolton (1985) pointed out that two sources of dilation exist: high density of particles and low confinement. The former can be mitigated by placing sand in the model in as loose of a state as possible (i.e., highest void ratio possible). As the bottom plot in Figure 2.22 shows, low confinement can cause dilation even for high void ratio, as is the case in the small-scale model. For the prototype case, however, only a small range of depths near the top of the retaining wall will experience dilation for soils with high void ratios. These dilation effects can be accounted in the actual friction angle ϕ:

$$\phi = \phi_{ss} + \psi \tag{30}$$

where ϕ_{ss} is the constant steady-state friction angle and ψ is the dilation angle. The consequence of the increase in ϕ is primarily a reduction in lateral pressures on the retaining wall and ultimately a reduction in the corresponding bending moment response. This can be illustrated in Figure 2.23, where the results of experimental testing are shown for the fully excavated

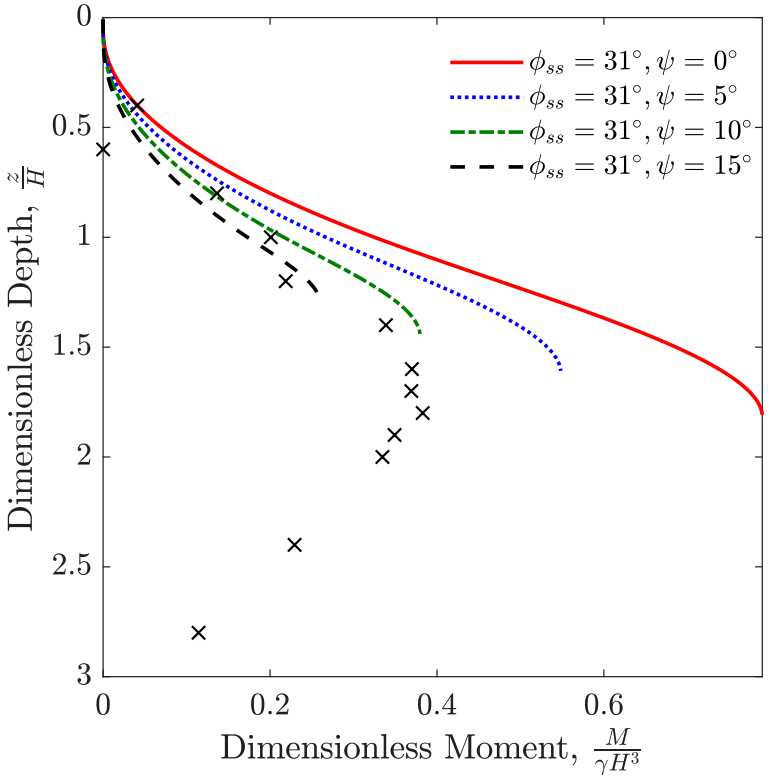

Figure 2.23. Effect of dilation on the bending moment response of the thicker retaining wall when fully excavated with no surcharge loading applied.

(excavation height equal to 12.5 cm) and $\frac{d}{H} = 0.1$, $\frac{q_{vo}}{\gamma H} = 1$, and $\frac{q_h}{q_{vo}} = 0.3$. The addition of 15° of dilation causes a dramatic reduction in bending moment. For the purpose of this document, the value of ϕ angle was estimated based on the comparing the bending moment results with that predicted by Coulomb theory for the unloading condition and reduced by 5° for the high vertical surcharge loading case causing increased confinement and lower dilation. It is recommended that the actual value of ϕ be investigated for future use of this research.

3 Proposed Limit Equilibrium Solution

3.1 Theoretical Solution

To incorporate more complex surcharge loading, the solution given by Motta (1994) and Greco (2006) was modified to include the effects of horizontal loads and applied moments. As Figure 3.1 shows, the modified solution has the addition of a horizontal surcharge, q_h, and the vertical surcharge, $q_v(x)$, is now non-uniform due to the effect of the moment. This non-uniformity is due to the combined effect of a uniform vertical surcharge from the dead load, q_{vo}, and an applied moment from the horizontal load. Since the distributed wind load is applied along the height of the noise wall, its force resultant, $q_h b$, is applied at some height above the base of the

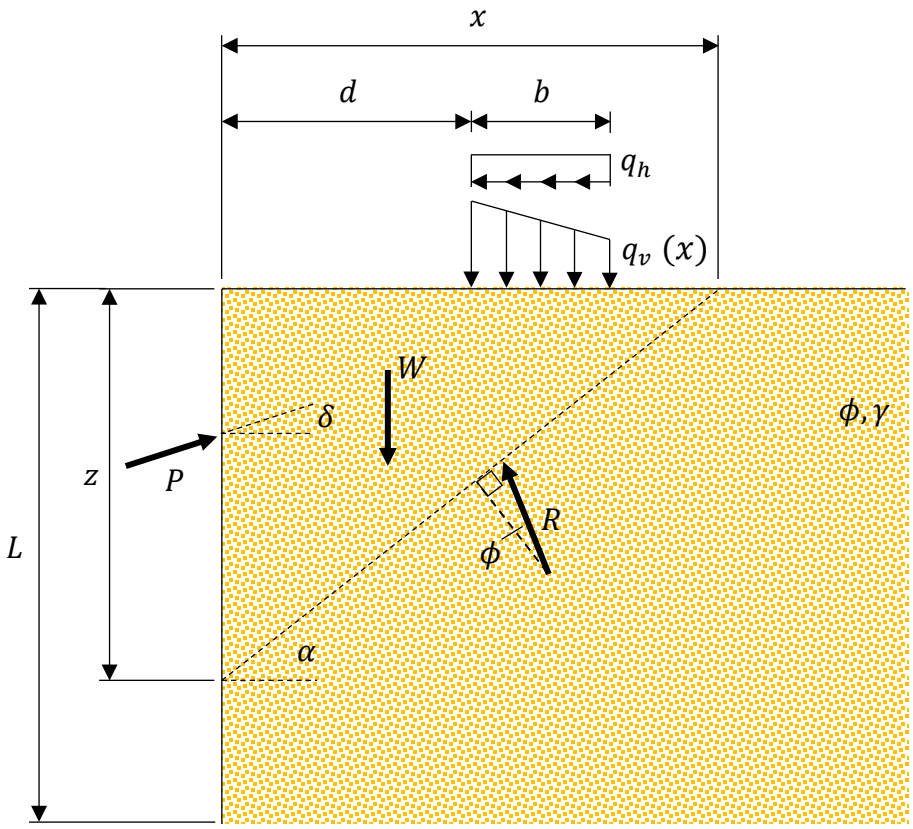

Figure 3.1. Schematic of proposed limit equilibrium solution that considers complex surcharge loading from linearly varying vertical sucharge and uniform horiztonal loading.

noise wall, h, causing a moment, $q_h bh$ (Note: Solving the force equilibrium gives the piecewise function with three sub-functions, similar to the models presented in Chapter 2, for thrust, $P(\alpha, z)$, as:

$$P = \begin{cases} \frac{1}{2}\gamma z^2 f(\alpha) g(\alpha) & \text{if} \quad \alpha > \theta_1 \\ \left[\frac{1}{2}\gamma z^2 f(\alpha) + (z f(\alpha) - d)(A q_{vo} - \tan(\delta)\, q_h)\right] g(\alpha) + \frac{q_h (z f(\alpha) - d)}{\cos(\delta)} & \text{if} \quad \theta_1 > \alpha > \theta_2 \\ \left[\frac{1}{2}\gamma z^2 f(\alpha) + b(q_{vo} - \tan(\delta)\, q_h)\right] g(\alpha) + \frac{q_h b}{\cos(\delta)} & \text{if} \quad \alpha < \theta_2 \end{cases} \quad (31)$$

where $f(\alpha) = \frac{1}{\tan(\alpha)}$, $g(\alpha) = \frac{\sin(\alpha-\phi)}{\cos(\phi+\delta-\alpha)}$, $\theta_1 = \tan^{-1}\left(\frac{z}{d}\right)$, $\theta_1 = \tan^{-1}\left(\frac{z}{d+b}\right)$, and $A = \left[1 + \frac{q_h}{q_{vo}}\left(\frac{6h}{b}\right) - \frac{q_h}{q_{vo}}\left(\frac{12hd}{b^2}\right)\right] - \frac{q_h}{q_{vo}}\left(\frac{6h}{b^2}\right)(zf(\alpha) + d)$.

The process of determining lateral thrust for a given depth, z, in the proposed model is similar to the process for the vertical-only surcharge models by Motta (1994) and Greco (2006). The maximum value of the piecewise function P is determined for α from ϕ to 90° and the horizontal component of the maximum thrust, $P_h(z)$, is calculated as $P_h(z) = P_{max}(z)cos(\delta)$. This process is repeated for all values of z from zero depth to the height of the retaining wall, L. With these values of lateral thrust, the lateral earth pressure, $\sigma_h(z)$, is determined as $\sigma_h(z) = \frac{dP_h(z)}{dz}$ (Steenfelt and Hansen 1983; Georgiadis and Anagnostopoulos 2004).

Since the function for P is piecewise, the sub-function from Equation 31 that results in the maximum value of P will vary throughout the domain of z from zero to L. Two main factors compete based on the value of α: the magnitude of the combined forces of the surcharge and self-weight that decreases with increasing α and the value of the load transfer function, $M(\alpha)$,

that increases with increasing α. While the self-weight magnitude always increases with increasing α and z, the magnitude of the contribution from the surcharge is limited to its maximum when the critical failure surface intersects the ground surface at the far end of the surcharge; i.e., when $x = d + b$. This limitation has important implications for which subfunction of Equation 31 produces the maximum thrust, P, and ultimately the magnitude of the lateral earth pressure on the retaining wall.

Most researchers have estimated the induced stress from the surcharge by simply subtracting the traditional Coulomb and Rankine active earth pressure distributions, $K_A \cos(\delta)\, \gamma z$ (Georgiadis and Anagnostopoulos 1998; Steenfelt and Hansen 1983). Here a more rigorous approach was employed to remove the effect of the contribution to the lateral earth pressure from the self-weight of the soil. From the distribution of the maximum thrust, P_{max}, for each value of z along the height of the wall, the term related to self-weight from Equation 31 was removed:

$$P_q(z) = P_{max}(z) - \frac{1}{2}\gamma z^2 f(\alpha_c) g(\alpha_c) \tag{32}$$

The induced stress from the surcharge was determined via numerical differentiation of $P_q(z)\cos(\delta)$ with respect to depth:

$$\Delta\sigma_{h,q} = \cos(\delta)\left[\frac{P_q(z + dz) - P_q(z)}{\Delta z}\right] \tag{33}$$

At shallow depths (Zone 1 in Figure 3.2a), the critical failure wedge (i.e., the failure wedge resulting in the maximum lateral thrust) does not intersect with the surcharge and the first sub-function in Equation 31 controls. Therefore, the lateral earth pressure Zone 1 is independent of the surcharge and can be determined through Coulomb's and Rankine's theories for self-weight. As depths increase, the failure wedge with the minimum value of $\alpha = \phi$ begins to include a

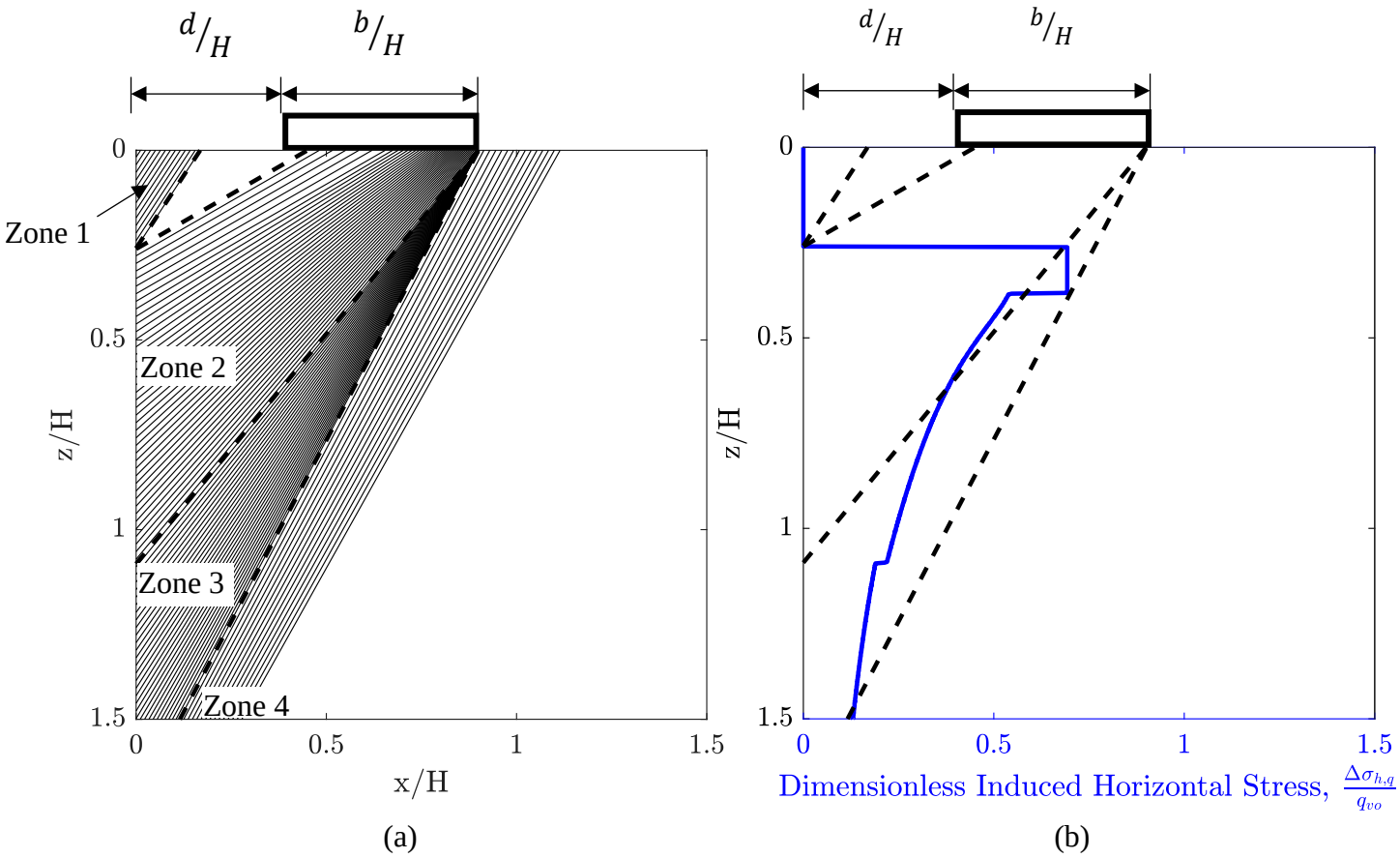

Figure 3.2. Typical results from proposed solution showing (a) critical wedge progression with depth and (b) resulting induced horizontal stress from surcharge. Dashed lines signify characteristic failure surfaces, where abrupt changes in lateral earth pressure occur.

larger portion of the surcharge and ultimately an increasing contribution to the thrust, P. Eventually, a failure wedge that includes a portion of the surcharge footprint produces the maximum thrust (Zone 2 in Figure 3.2a) and the second sub-function in Equation 31 controls. Note that if the critical failure wedge is inclined at the minimum wedge angle $\alpha = \phi$, the

reaction force, R, is vertical and the load transfer function, $g(\alpha)$, is equal to zero in Equation 28. This is reflected in lateral earth pressure, shown in Figure 3.2b, where a section of Zone 2 with a constant lateral earth pressure of magnitude $\frac{q_h}{\tan(\phi)}$ occurs. The critical failure wedges contain an increasing portion of the surcharge area as depth increases until the full extent of the surcharge is reached when $zf(\alpha) = d + b$, marking the transition to Zone 3.

In Zone 3, the lateral extent of the failure wedge remains constant at the far edge of the surcharge $(zf(\alpha) = d + b)$ even with increasing depth, producing a fan-shaped zone (Figure 3.2a). The magnitude of the surcharge remains constant at its maximum value ($q_h b$ and $q_{vo} b$ for the horizontal and vertical surcharge, respectively), but the load transfer function, $g(\alpha)$, increases with depth. As the depth increases, the critical failure surface will eventually begin to extend past the width of the surcharge (Zone 4).

The abrupt changes in the controlling sub-functions and zones cause abrupt changes in the resulting lateral earth pressure. The transition from Zone 1 to Zone 2 marks a sharp increase in lateral earth pressure for two reasons: (1) the surcharge is now contributing to the critical failure wedge and (2) the size and weight of the failure wedge have a pronounced increase from Zone 1 to Zone 2. The transition from Zone 2 to Zone 3 marks a decrease in the slope of the lateral earth pressure, as the wedge keeps a constant width, $d + b$, even as the depth increases. This is because the downward force due to the surcharge is constant, $q_{vo} b$, while the self-weight of the wedge continues to increase due to its dependence on depth, z.

3.2 Effects of Input Parameters in Proposed Solution

As Equation 31 shows, the thrust, P, is dependent on several parameters and therefore, the lateral earth pressure, σ_h, will be dependent on these parameters. A set of parameters were selected to

illustrate their effects on the lateral earth pressure, based on the dimensional analysis presented in Section 2.4.2. These parameters include the distance from the noise wall to the retaining wall, d, the friction angle, ϕ, the magnitude of the uniform vertical load contribution to the vertical surcharge, q_{vo}, and the magnitude of horizontal surcharge, q_h. The parameters, excluding ϕ which is already dimensionless, were made dimensionless to generalize the interpretation of the results. The resulting dimensionless parameters are: the distance relative to the exposed wall height, $\frac{d}{H}$, the magnitude of the uniform vertical surcharge relative to the vertical effective stress at the elevation of the excavation in the backfill, $\frac{q_{vo}}{\gamma H}$, and the magnitude of the horizontal surcharge relative to the uniform vertical surcharge, $\frac{q_h}{q_{vo}}$.

Table 1 summarizes the different dimensionless parameters and the values chosen to illustrate their effects. The underlined values show the parameter value kept constant when other parameters are varied. Figures 3.3 through 3.6 show the effects of $\frac{d}{H}$, ϕ, $\frac{q_h}{q_{vo}}$, and $\frac{q_{vo}}{\gamma H}$ respectively, on the lateral earth pressure from both the self-weight of the soil and surcharge, σ_h. Both the resulting lateral earth pressure and moment are presented as the dimensionless parameters $\frac{\sigma_h}{\gamma H}$ and $\frac{M}{\gamma H^3}$. Appendix A shows the induced horizontal stress from the surcharge, $\Delta\sigma_{h,q}$, that was made dimensionless, $\frac{\Delta\sigma_{h,q}}{q_{vo}}$.

Table 1. Summary of dimensionless parameter values chosen for plotting lateral earth pressures. Bolded values signify constant values when comparing different parameters.

Distance, $\frac{d}{H}$	Vertical Surcharge, $\frac{q_{vo}}{\gamma H}$	Horizontal Surcharge, $\frac{q_h}{q_{vo}}$	Friction Angle, ϕ
0	0.1	-0.3	20°
0.25	**0.5**	0	**30°**
		0.1	
1	1	**0.3**	40°

The figures in the following subsections show that the four dimensionless parameters (i.e., $\frac{d}{H}$, ϕ, $\frac{q_h}{q_{vo}}$, $\frac{q_{vo}}{\gamma H}$) have a profound effect on the lateral earth pressure distributions and corresponding bending moment. These effects include the depth at which the surcharge begins to influence the lateral earth pressure, and overall magnitude and trend of the relative lateral earth pressure, $\frac{\sigma_h}{\gamma H}$. The depth at which the surcharge begins to influence the lateral earth pressure marks the threshold at which a failure plane containing some or all the surcharge provides a greater thrust onto the wall compared to the well-known failure wedge from self-weight alone provided by the traditional Coulomb and Rankine theories.

3.2.1 Relative Distance, $\frac{d}{H}$

Figure 3.3 shows the effect of the distance, d, between the surcharge loading and the retaining wall. The relative distance, $\frac{d}{H}$, has the most profound effect on the depth at which the surcharge begins to influence lateral earth pressures, z_q. This is because the distance, d, is directly related to the minimum depth that a failure wedge contains a portion of the surcharge, $z_{q,min} = d\tan(\alpha_{min})$ (where $\alpha_{min} = \phi$). By increasing the value of $\frac{d}{H}$, the depth at which a failure wedge

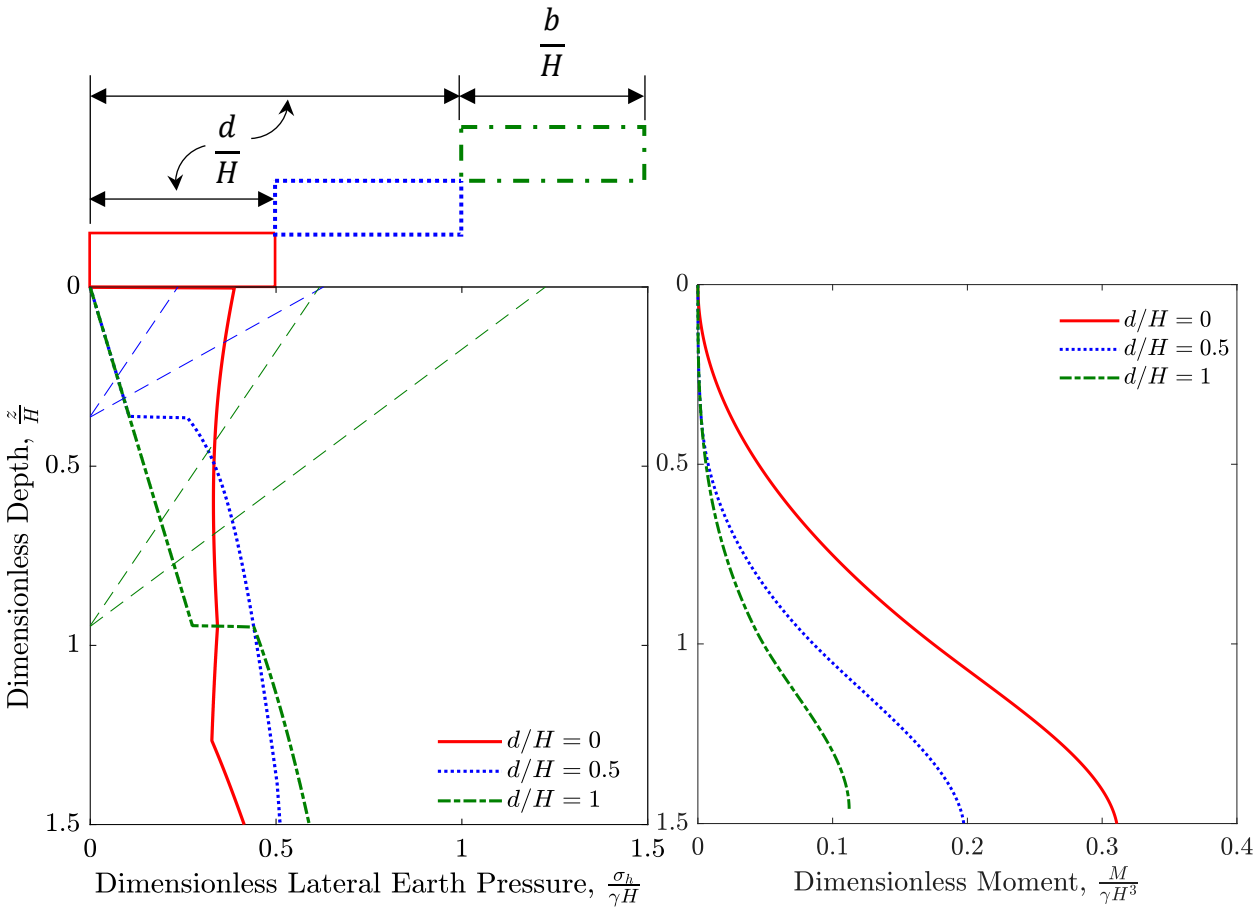

Figure 3.3. Effect of the distance, d, between the retaining wall and the applied surcharge on (a) the lateral earth pressure from both self-weight of the soil and surcharge loading and (b) the corresponding bending moment. Thin, dashed lines correspond to the first two characteristic failure planes.

containing the surcharge overtakes the critical failure wedge from soil self-weight alone is forced to deeper depths, as shown in Figure 3.4a. To the same effect, the distance, d, has important implications on whether the surcharge will affect the lateral earth pressures along the wall at all. If the value of $\mathrm{dtan}(\phi)$ exceeds the depth to point of fixity, the surcharge loading will no longer affect the lateral earth pressures that promote failure of the wall.

In addition to the significant effect on z_q, the parameter, d, also affects the overall magnitude and trend of the relative lateral earth pressure distribution (Figure 3.3a). Near the top of the retaining wall, lower values of d unsurprisingly result in higher earth pressures since a larger

portion of the surcharge loading is included in critical failure wedges at low depths. At deeper depths near $z = H$, however, the relative lateral earth pressure magnitude for further distanced surcharges, eventually exceed the magnitudes from the surcharges at closer proximity to the wall. This is because the critical failure wedges meet the far edge of the surcharge. At this point, the magnitude of the surcharge contribution reaches its maximum. This effect occurs at shallower depths for closer surcharge distances. While the difference between relative surcharge

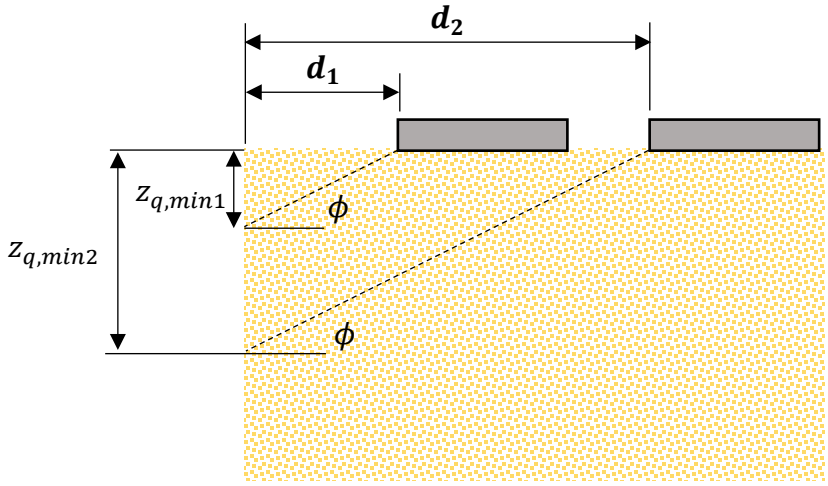

(a)

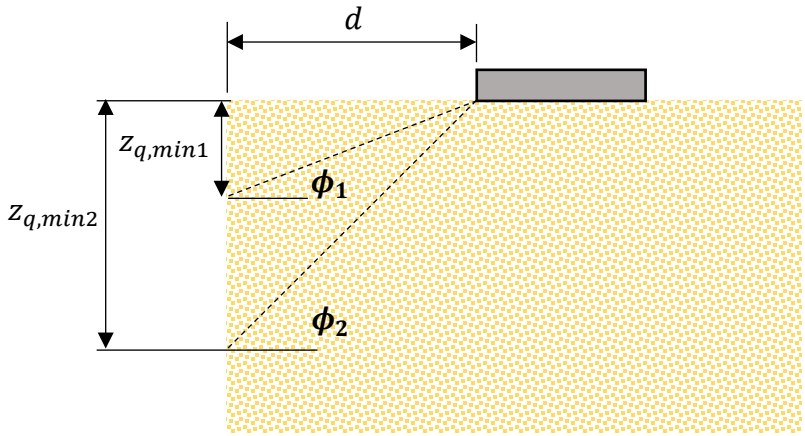

(b)

Figure 3.4. Schematic showing the reliance of the minimum depth to influence, $z_{q,min}$, on (a) distance between retaining wall and surcharge, d and (b) friction angle, ϕ.

magnitudes differs with varying values of d, the greatest effect is at the depth at which the surcharge begins to influence the lateral earth pressures.

The effect of the value of d also has important implications for the corresponding bending moment due to the applied pressures, as shown in Figure 3.3b. Smaller values of d produce significantly larger bending moments and the wall should exhibit detectable changes to the bending moment response. This change in response is shown to be consistent with the results of experimental testing in Chapter 4.

3.2.2 Friction Angle, ϕ

Figures 3.5a and 3.5b shows the effect of varying friction angle, ϕ, on $\frac{\sigma_h}{\gamma H}$ and $\frac{M}{\gamma H^3}$, respectively. The friction angle yields similar effects to the lateral earth pressure as the surcharge distance. As previously mentioned, the minimum depth to surcharge influence, $z_{q,min}$, is directly dependent on ϕ, $d\tan(\phi)$. As Figure 3.4b shows, higher values of ϕ force $z_{q,min}$ to deeper depths. Because typical values for ϕ vary between roughly 20° and 45°, the value of $z_{q,min}$ ranges between roughly $0.35d$ and d, respectively. The friction angle again partially determines whether the surcharge will affect the lateral earth pressure of the wall; if $dtan(\phi)$ is greater than depth on the backfill side of the wall to the pivot point, the surcharge will not affect the wall.

The dependence of $z_{q,min}$ on the value of ϕ also affects the range of depths where $\alpha = \phi$ and a constant lateral earth pressure magnitude, $\sigma_h = q_h/\tan(\phi)$, is applied. Since α has a minimum value of ϕ, lower values of ϕ result in failure wedges encountering the surcharge at shallower depths.

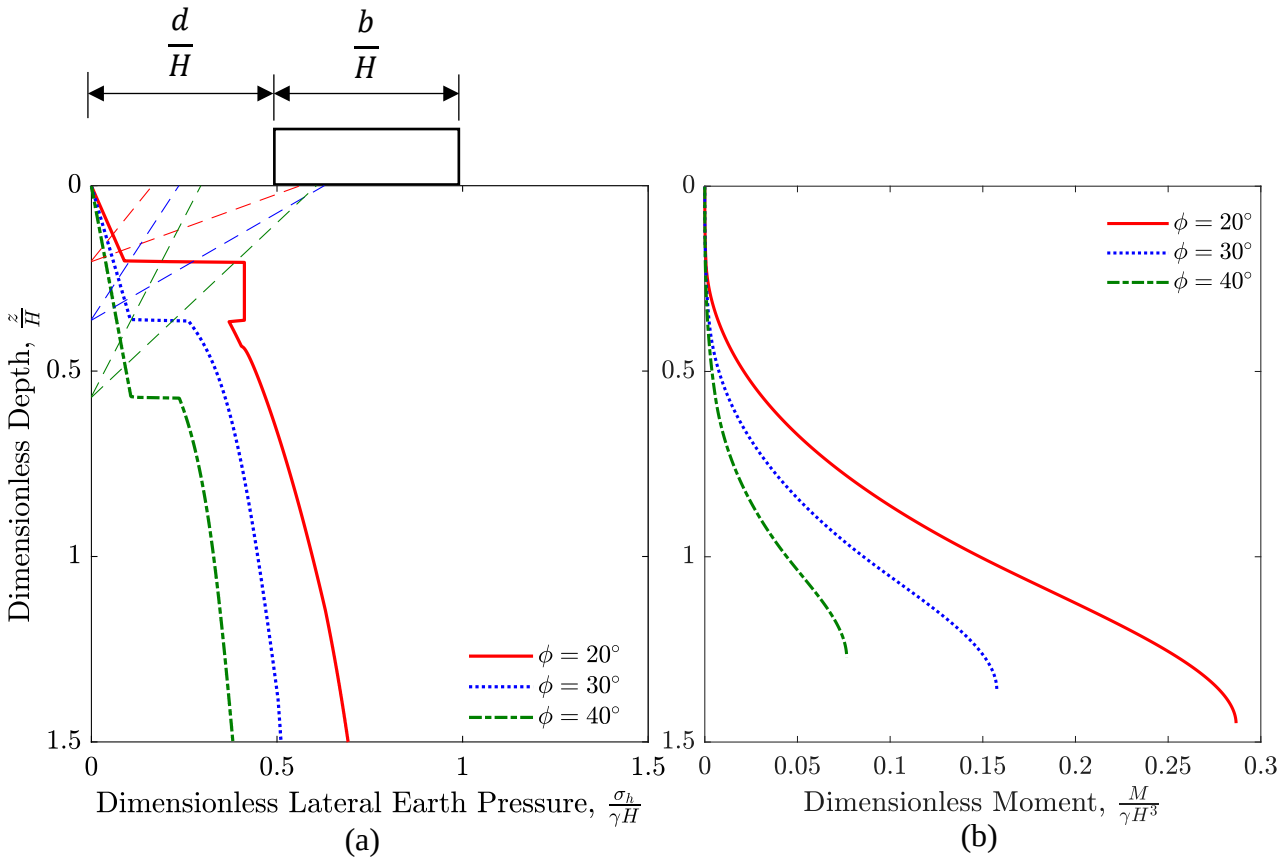

Figure 3.5. Effect of varying friction angle on (a) the lateral earth pressure from both the self-weight of the soil and the applied surcharge for varying friction angle, ϕ and (b) the corresponding bending moment. Thin, dashed lines correspond to the first two characteristic failure planes.

In addition to range of constant lateral earth pressure, the overall magnitude of the relative lateral earth pressure is also greatly affected by ϕ, with lower friction angles resulting in higher pressures. This is rather unsurprising as this concept is both intuitive and widely accepted in the case of self-weight-only loading (i.e., no surcharge loading), where the active earth pressure coefficient, $K_a = \frac{1-\sin(\phi)}{1+\sin(\phi)}$, is larger for higher values of ϕ. As Figure 3.5b shows, changes to the value of ϕ also produce significant changes to the bending moment from the applied lateral pressures. This change in bending moment should thus be detectable in the experimental testing presented in Chapter 4.

3.2.3 Relative Horizontal Surcharge, $\frac{q_h}{q_{vo}}$

Figure 3.6a and 3.6b shows the effect of the horizontal surcharge magnitude, q_h, on the values of $\frac{\sigma_h}{\gamma H}$ and $\frac{M}{\gamma H^3}$, respectively. As Equation 28 shows, the relative horizontal surcharge, q_h/q_{vo}, has one of the more complicated relationships with the thrust due to its effect on both the slope of the linearly varying vertical surcharge (moment loading) and the horizontal surcharge itself. As Equations 31b and 31c show, there are three terms that contain q_h: the $q_{vo}A$ term (related to the moment in Equation 31b), the term $-\tan(\delta)\, q_h$ (related to the reaction between the failure wedge and the adjacent soil mass), and the final term in Equations 31b and 31c (related to the direct contribution of q_h to the thrust).

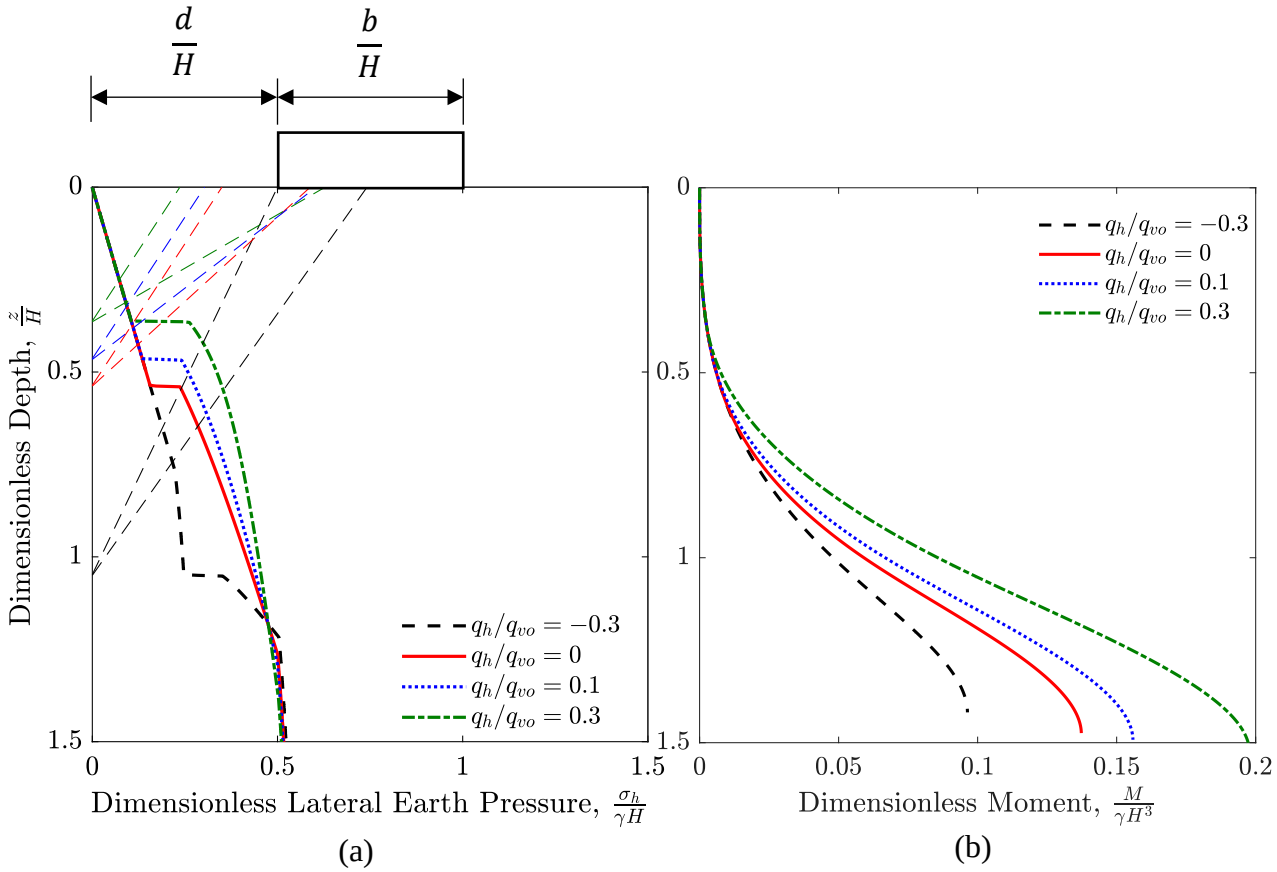

Figure 3.6. Effect of varying horizontal surcharge, q_h on (a) the lateral earth pressure from both the self-weight of the soil and the applied surcharge and (b) the corresponding bending moment. Thin, dashed lines correspond to the first two characteristic failure planes.

For the first term, $q_h A$, higher values of q_h result in a higher contribution from the linearly-varying vertical surcharge and higher values of thrust and lateral earth pressure. As the equation for the variable, A, shows, there are positive and negative terms. These conflicting terms result in a relatively small effect on the thrust and will only have an effect when Equation 31b controls.

The second term, $-\tan(\delta)\, q_h$, is the effect of the horizontal surcharge lessening the reaction force between the failure wedge and the surrounding soil mass. The higher the value of q_h, the more the horizontal surcharge acts to decrease the reaction force of the failure wedge with the surrounding soil and lowers the effect of both the self-weight of the soil and the vertical surcharge. Due to dependence of the second term on roughness of the wall, δ, this term is greatly reduced for smoother walls and disappears for perfectly smooth walls. The final term is the direct contribution of q_h to the thrust, P, with higher values q_h causing larger values of P. Of these three terms, the final term has the greatest effect on the thrust and its contribution relative to the vertical surcharge and the self-weight of the soil will be dependent on the critical failure inclination angle, α_c.

A direct example of this dependence on α_c, is the value of z_q. Although the value of q_h/q_{vo} does not affect $z_{q,min} = dtan(\phi)$, the surcharge does have an effect on when the actual depth to surcharge influence, z_q, with larger values of q_h/q_{vo} resulting in shallower depths of surcharge influence. As the value of α_c is generally low near z_q, the value for the load transfer function, $g(\alpha)$ is small, thus making the final q_h term dominant and the influence of the reaction of the failure wedge with the surrounding soil mass small or even zero when $\alpha_c = \phi$.

This effect is also related to the overall magnitude of σ_h, as shown in Figure 3.6a, where the differences in lateral earth pressures between the different plot lines is greatest near depths equal

to z_q. As expected, higher magnitudes of q_h toward the retaining wall results in higher lateral earth pressure, since the horizontal surcharge will contribute to higher values of the horizontal thrust. As depths increase, however, the value of α_c increases and the contribution of q_h relative to the vertical surcharge and the self-weight of the soil decreases, as shown by the plot lines converging at $\frac{z}{H} \cong 1.2$ in Figure 3.6a.

In the case of wind loading on noise-wall barriers, the direction of loading can occur both toward or away from the retaining wall, resulting in either positive or negative values of q_h, respectively. For the case where q_h/q_{vo} is negative (i.e., the horizontal surcharge is directed away from the retaining wall) there is a dramatic increase in value of z_q. This is because the horizontal surcharge acts to stabilize the wedge, decreasing the thrust, P, for wedges that contain a portion of the surcharge. According to this proposed limit equilibrium formulation, negative values of q_h will not cause increases to the lateral earth pressures. This predicted lack of adverse effect was found to be consistent with the results of experimental testing presented in Chapter 4 of this thesis.

3.2.4 Relative Vertical Surcharge, $\frac{q_{vo}}{\gamma H}$

The relative vertical surcharge, $\frac{q_{vo}}{\gamma H}$, is the final parameter from the proposed solution that significantly affects lateral earth pressure (Figure 3.7a) and corresponding bending moment (Figure 3.7b). The effects of the vertical surcharge magnitude without any horizontal surcharge have been studied extensively (e.g., Motta 1994; Georgiadis and Anagnostopoulos 1998), and Figure 3.7a shows that the addition of horizontal surcharges and applied moment effects have similar effects to z_q and the overall magnitude of σ_h as the previous models done by others. Higher magnitudes of q_{vo} result in shallower depths at with the surcharge begins to influence, z_q. Similar to the discussion for q_h, this is because high vertical surcharges allow failure wedges

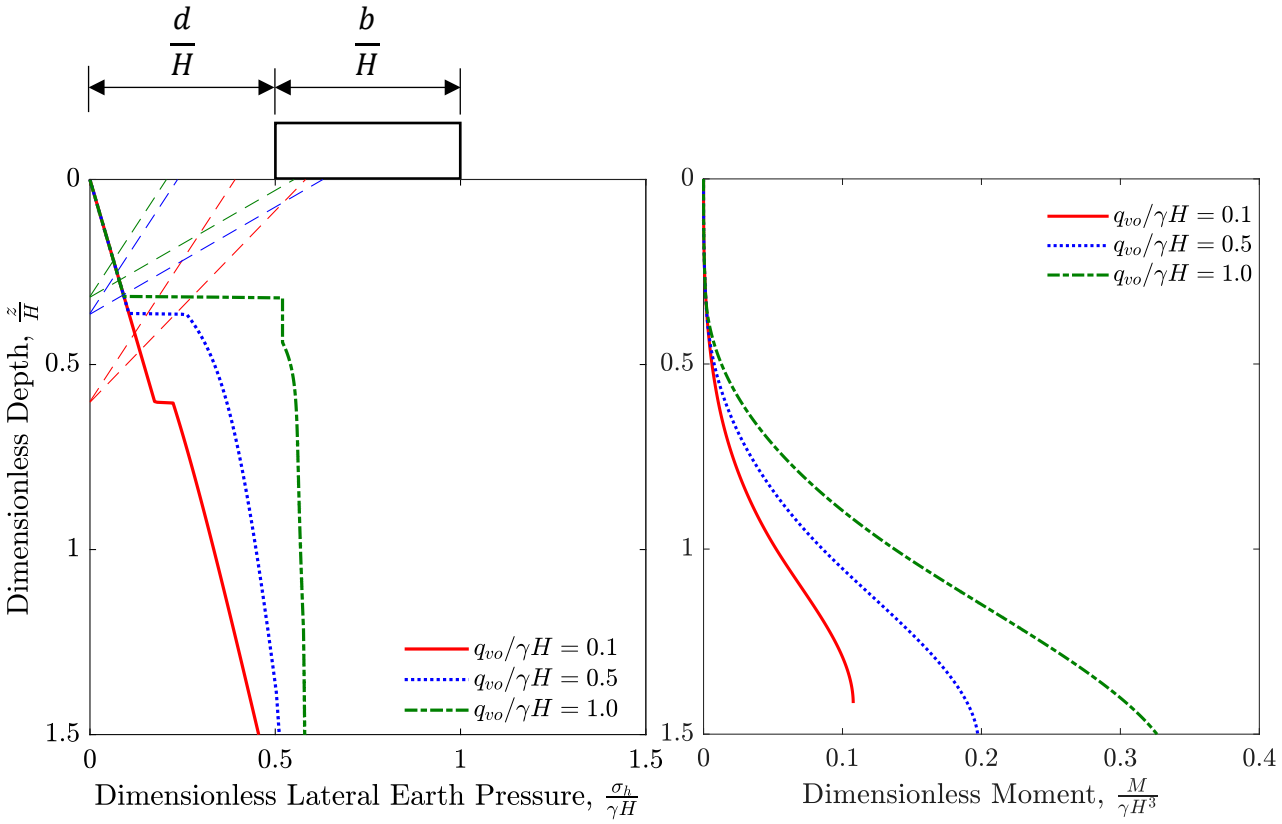

Figure 3.7. Effect of varying vertical surcharge magnitude, q_{vo}, on (a) the lateral earth pressure from both the self-weight of the soil and the applied surcharge and (b) the corresponding bending moments. Thin, dashed lines correspond to the first two characteristic failure planes.

containing the surcharge to overtake the values of thrust from self-weight-only failure wedges at shallower depths. The effect of higher q_{vo} magnitudes causing higher overall magnitudes of σ_h is rather intuitive, since higher values of q_{vo} will contribute to higher values of thrust, P.

3.3 Lessons Learned

A limit equilibrium formulation to account for horizontal and vertical surcharges is proposed based on similar solutions from Motta (1994) and Greco (2006) for vertical surcharge loading only. The effects of four primary input parameters in dimensionless form ($\frac{d}{H}$, ϕ, $\frac{q_h}{q_{vo}}$, and $\frac{q_{vo}}{\gamma H}$) were presented. Key conclusions include:

a) Decreasing relative distance, $\frac{d}{H}$, significantly decreased the depth that the surcharge begins to influence, z_q. The value of $\frac{d}{H}$ had a small effect on the maximum value of the relative horizontal stress, $\frac{\sigma_h}{\gamma H}$, with the greatest influence at depths near z_q.

b) Decreasing friction angle, ϕ, caused both shallower values of z_q and higher values of $\frac{\sigma_h}{\gamma H}$.

c) Increasing relative horizontal surcharges, $\frac{q_h}{q_{vo}}$, resulted in shallower values of z_q and higher values of $\frac{\sigma_h}{\gamma H}$ near z_q. This effect diminished with depth and the value of $\frac{q_h}{q_{vo}}$ had almost no effect for relative depths, $\frac{z}{H} \cong 1.2$. Negative values of $\frac{q_h}{q_{vo}}$ made z_q significantly deeper and dramatically decreased the values of $\frac{\sigma_h}{\gamma H}$ above $\frac{z}{H} \cong 1.2$.

d) Increasing relative vertical surcharge magnitude, $\frac{q_{vo}}{\gamma H}$, resulted in shallower values of z_q and higher values of $\frac{\sigma_h}{\gamma H}$ near z_q. Unlike q_h, higher vertical surcharge magnitudes produced higher values of $\frac{\sigma_h}{\gamma H}$ for $\frac{z}{H} > 1.5$.

e) For each of these trends, a noticeable change in bending moment occurred and should be clearly seen in the bending moment response of experimental testing.

As discussed in Chapter 2, flexible, cantilever retaining walls resist an induced movement of wall via earth pressures alone (e.g., see Figure 2.10). It is hypothesized that the threshold at which surcharge loading will induce horizontal stress on a retaining wall is a complex relationship of $\frac{d}{H}$, ϕ, $\frac{q_h}{q_{vo}}$, and $\frac{q_{vo}}{\gamma H}$. If the combination of these parameter produces a z_q deeper than the point of fixity (Figure 2.12), the surcharge does not influence the retaining wall. This hypothesis is examined via the experimental testing presented in Chapter 4.

4 Experimental Testing

4.1 Introduction

A 1-g (non-centrifuge) small-scale retaining wall model was constructed and used to evaluate changes in stress state caused by application of horizontal and vertical surcharge loads. The physical model was constructed and subsequently tested in an attempt to validate the proposed limit equilibrium formulation presented in Chapter 3. A variety of surcharge positions and magnitudes were tested. Experimental strain gauge results were converted into bending moment from the known flexural rigidity of the retaining wall. These results were ultimately compared to values predicted by the proposed formulation, a formulation based on the theory of elasticity, and the approximate AASHTO method.

4.2 Model Setup and Testing Procedure

A 450-mm-wide by 600-mm-tall by 900-mm-long wooden container (Figure 4.1) was filled with dry sand and used aluminum sheet metal to model a flexible retaining wall. The response of the wall was monitored with a series of strain gauges fixed on the excavation side of the wall. This sheet metal was partially embedded into the sand, acting as a flexible, cantilever retaining wall. Strain gauge spacing varied between 12.5 mm and 50 mm. The uneven distribution of strain gauges with depth was designed to capture the response of the wall in areas of interest (i.e., near the elevation of the excavation of the retaining wall). Two thicknesses, 0.8 mm (0.032 in) and 2 mm (0.08 in), of aluminum sheet metal were used for low- and high-surcharge magnitudes relative to the self-weight of the soil, respectively. The differing thicknesses also enabled the research team to assess how both relatively flexible and relatively rigid walls respond to complex surcharge loading.

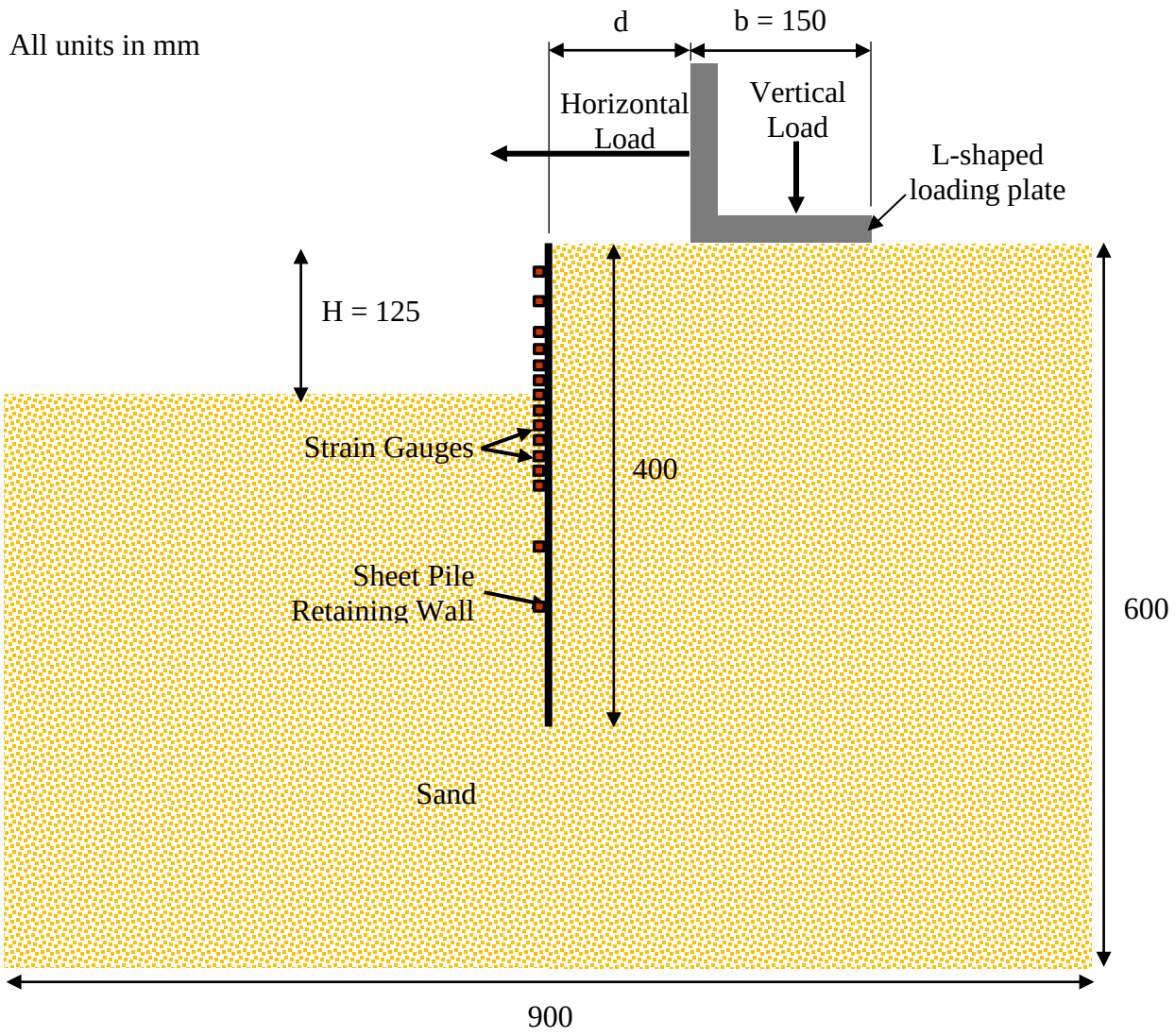

Figure 4.1. Schematic diagram of experimental setup.

To limit the effect of friction between the sidewalls of the model and the sand inside, PFTE (commercially known as Teflon) films were applied to each sidewall. The dry sand had a critical state friction angle of 31° (as determined via the angle of repose according to Cornforth 1973; Bolton 1986; Santamarina 2001). Due to the low confining pressures from the small-scale of the model, significant dilation was expected, resulting in peak behavior and higher acting friction angles (Bolton 1986), and confirmed by direct shear testing. The unit weight of the sand was estimated by measuring the weight of material placed per 100-mm increment, with an average value of 15.5 kNm^{-3}.

Testing began by filling of the model with sand in a series of 100-mm lifts with the sheet metal fixed in place. Sand was slowly placed via a funnel, effectively putting the material in loosest possible state. Once the model was filled, baseline strain readings were taken. Sand on the excavation half of the model was then removed in 50-mm and 25-mm lifts via vacuum until the final excavation elevation. Strain gauge data were collected at each lift height. After the excavation was completed, an L-shaped loading plate (Figure 4.1) was placed, effectively applying a vertical surcharge. The initial distance, d, between the L-shaped plate and the retaining wall was 150 mm.

An increasing horizontal load was then applied in the direction *away* from the sheet pile wall, via a pulley system. The horizontal load effectively applied both a horizontal surcharge and moment in the direction away from the sheet pile wall. The magnitude of the horizontal load began at 10% of the vertical load and progressively increased to 20%, 30%, 40% of the vertical load (Note: no readings were taken for the 30%-vertical load for the low vertical surcharge testing). Strain data were collected after each increment of horizontal load. The process was then repeated with 10%, 20%, 30%, and 40% of the weight of the noise wall applied in the direction *toward* the sheet pile. The process of vertical loading and consecutive horizontal loading was repeated for distances of 50 mm and 10 mm between the noise wall and the retaining wall until massive deformation of the sheet pile was observed.

4.3 Data Processing

Before any data could be analyzed, the strain gauge measurements were calibrated. To begin the calibration process, the self-weight of the aluminum sheet metal with applied strain gauges was measured. The sheet metal was then placed with one end tightly clamped to form a cantilever (Figure 4.2), and strain measurements were taken to determine the strain due to self-

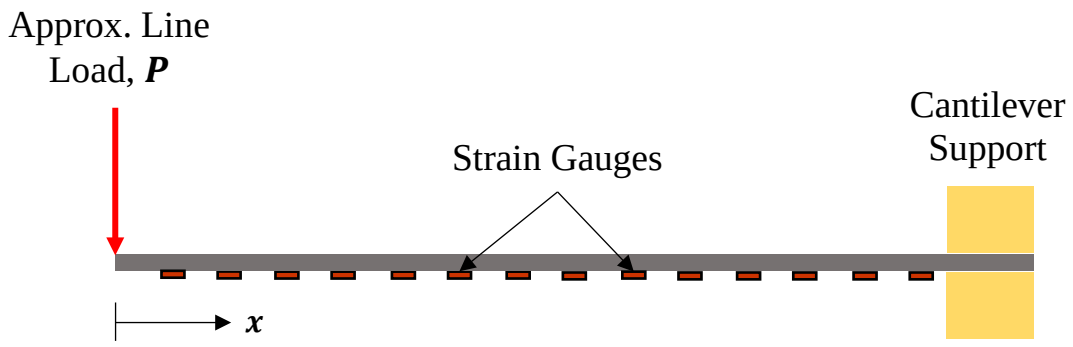

Figure 4.2. Set up to calibrate raw strain data.

weight, ε_{sw}. Next, a line load of magnitude, P, was applied at the very end of the cantilever and strain measurements were again taken. This measurement, ε_{P+sw}, includes strain from both the line load and the self-weight of the sheet metal. The strain due to the point load only, ε_P, is then:

$$\varepsilon_P = \varepsilon_{P+sw} - \varepsilon_{sw} \tag{34}$$

The value of ε_P measured in the setup can then be compared to theoretical strain due to line loading, $\varepsilon_{P,theo}$. The theoretical strain due to the point load can be determined from beam theory as:

$$\varepsilon_{P,theo} = \frac{12Px}{Et^3} \tag{35}$$

where x is the distance from the point load to the strain gauge being corrected, E is the Young's modulus of aluminum equal to 69 GPa, and t is the thickness of the sheet metal. Finally, the correction factor, CF, for calibration is given by:

$$CF = \frac{\varepsilon_{P,theo}}{\varepsilon_P} \tag{36}$$

In theory, the value of CF should be constant for any magnitude of P (provided the strain limit of the material is not exceeded). To ensure this was the case, the calibration process was repeated for multiple magnitudes of P and the value for CF was indeed found to be constant. With the value of CF for each strain gauge, the raw strain values, ε_{raw}, from data collected during experimental testing could then be corrected by:

$$\varepsilon_{corr} = CF\varepsilon_{raw} \tag{37}$$

where ε_{corr} is the calibrated strain value for a given strain gauge. This calibration process was peformed for each of the two retaining wall thicknesses.

As previously mentioned, the goal of this experimental testing program was to compare the measured strain data with the applied pressures from each of the three methods for quantifying the effects of the surcharge loading. To make this comparison, the measured strain and the predicted lateral pressures must be converted to like quantities. Bending moment was chosen to be the optimal quantity for comparison, as it can be easily determined from both lateral pressures along the wall and from the deformation (bending strain) these pressures cause on the sheet pile.

To convert the calibrated strain values measured during testing into the corresponding bending moment response, strain is first converted to stress from bending along the depth of the sheet pile, $\sigma_{bending}(z)$, via Hooke's Law:

$$\sigma_{bending}(z) = E\varepsilon_{corr}(z) \tag{35}$$

The bending stress from Equation 35 can then be related to moment by:

$$M(z) = \frac{2I\sigma_{bending}(z)}{t} = \frac{2EI}{t}\varepsilon_{corr}(z) \tag{36}$$

where $M(z)$ is the bending moment at depth, z, along the sheet pile, I is the area moment of inertia, and $\varepsilon_{corr}(z)$ is the calibrated strain for the strain gauge at depth, z.

The predicted lateral pressures from each of the methods is converted into bending moment via beam theory. Applied lateral pressures, σ_h, along the depth of the wall produce an internal force in the form of shear, V, and internal couple in the form of bending moment, M. These are related by:

$$V(z) = \int_0^z \sigma_h dz \approx \frac{1}{2}[\sigma_h(z) + \sigma(z - \Delta z)]\Delta z + V(z - \Delta z) \tag{37}$$

and

$$M(z) = \int_0^z V dz \approx \frac{1}{2}[V(z) + V(z + \Delta z)]\Delta z + M(z - \Delta z) \tag{38}$$

Since $V(z)$ and $M(z)$ are equal to zero at the top of the retaining wall, Equations 37 and 38 can be repeated iteratively along the depth of the sheet pile to produce the bending moment distribution, $M(z)$.

4.4 Results from Experimental Testing

After strain measurements were calibrated via the process presented in Section 4.3, comparisons were made between results from different loading conditions. The results presented here include data from both smaller surcharge magnitude testing ($\frac{q_{vo}}{\gamma H} = 0.1$), and testing done under larger surcharge magnitudes ($\frac{q_{vo}}{\gamma H} = 1$). For the smaller surcharge magnitude testing, the thinner, more flexible sheet pile wall was used in order to allow for finer sensitivity strain measurement

expected from smaller load changes. Conversely, the larger surcharge magnitudes employed the thicker, more rigid sheet pile wall in order to withstand the larger loads without yielding.

For each of the model walls, the sand was placed in the loosest possible state. Despite being placed in the loosest possible state, the very low confining pressures present in the small-scale model resulted in significant dilation effects. For the testing under lower vertical surcharge magnitudes, the actual value of ϕ used for comparing the different induced stress methods was $41°$ (i.e., $10°$ of dilation). For the testing under higher surcharge method, the actual ϕ used was $36°$ (i.e., $5°$ of dilation). These values of dilation angles are consistent with results from Bolton (1986), as the dilative component is significant even for low void ratio material but decreases with increasing confining stress.

Typical results from experimental testing are shown in Figure 4.3 through 4.7, in the form of dimensionless bending moments, $\frac{M}{\gamma H^3}$, versus dimensionless depth, $\frac{z}{H}$. Figures 4.3 and 4.4 show the effect of distance between the surcharge and retaining wall, d, for the high and low vertical surcharge magnitudes, respectively. In each of the two figures, decreasing d resulted in a higher bending moment response. These observations were expected from the results presented for the proposed limit equilibrium formulation (Figure 3.3b). Note that for Figure 4.4, there are outliers presented for dimensionless bending moment at $\frac{d}{H} = 0.2$. There is no known explanation for these values, other than possibly improper bonding between the strain gauge and sheet metal used for the thicker wall. Thus, data from this strain gauge were removed for subsequent figures. Figure 4.5 illustrates the effect of the direction of the horizontal surcharge, q_h, with negative values corresponding to horizontal surcharges applied away from the retaining wall and positive values representing surcharges toward the retaining wall. Negative values of q_h resulted in no

significant changes to the bending moment response, whereas positive values of the same magnitude resulted in large changes in the values for bending moment. The lack of change to the bending moment for negative values of q_h deviates from the results from the proposed limit equilibrium model (Figure 3.6b).

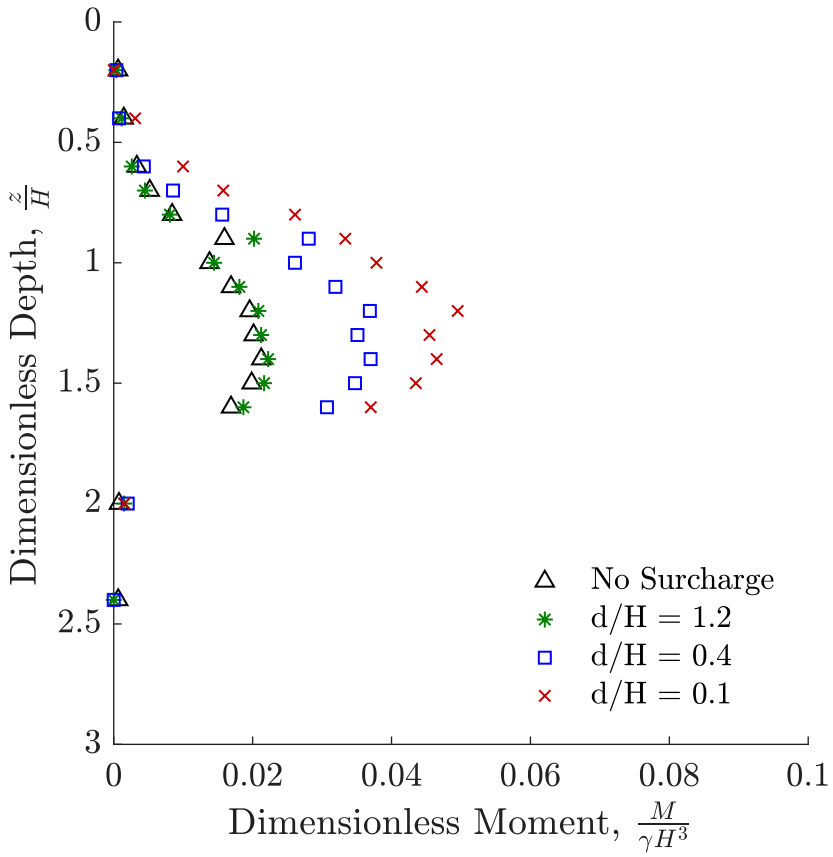

Figure 4.3. Typical results showing the effect of distance, $\frac{d}{H}$, for a constant $q_{vo}/\gamma H = 0.1$ and $q_h/q_{vo} = 0.4$.

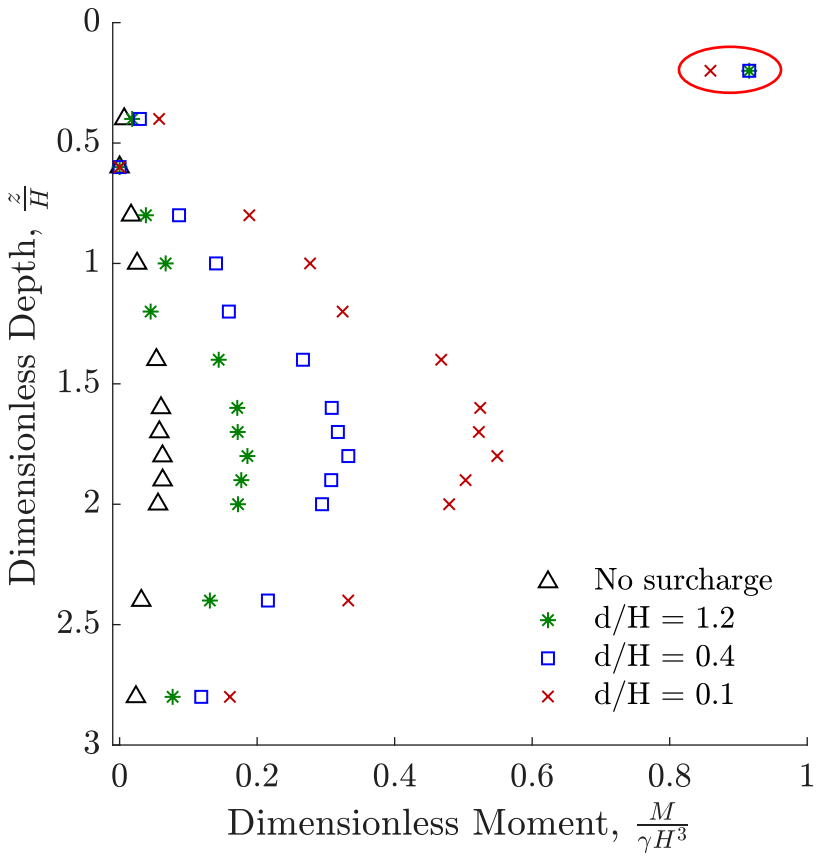

Figure 4.4. Typical results showing the effect of distance, d, for a constant $q_{vo}/\gamma H = 1$ and $q_h/q_{vo} = 0.4$. Outliers circled in red.

While Figure 4.5 exhibited the directional effects of q_h, Figure 4.6 illustrates the effect of the magnitude of q_h for horizontal surcharges directed toward the sheet pile wall (i.e., positive values of q_h). The bending moment response was negligible for small values of $\frac{q_h}{q_{vo}}$, but for relative values of 0.3 and 0.4, large changes to the bending moment are observed. Finally, Figure 4.7 shows the difference in bending moment response between the two tests run under different surcharge magnitudes. As expected, the higher surcharge magnitudes resulted in a larger bending moment response. These trends are in agreement with a similar a set of tests conducted by Georgiadis and Anagnostopoulos (1998), so the addition of the horizontal surcharge does not appear to change the effect of the vertical surcharge.

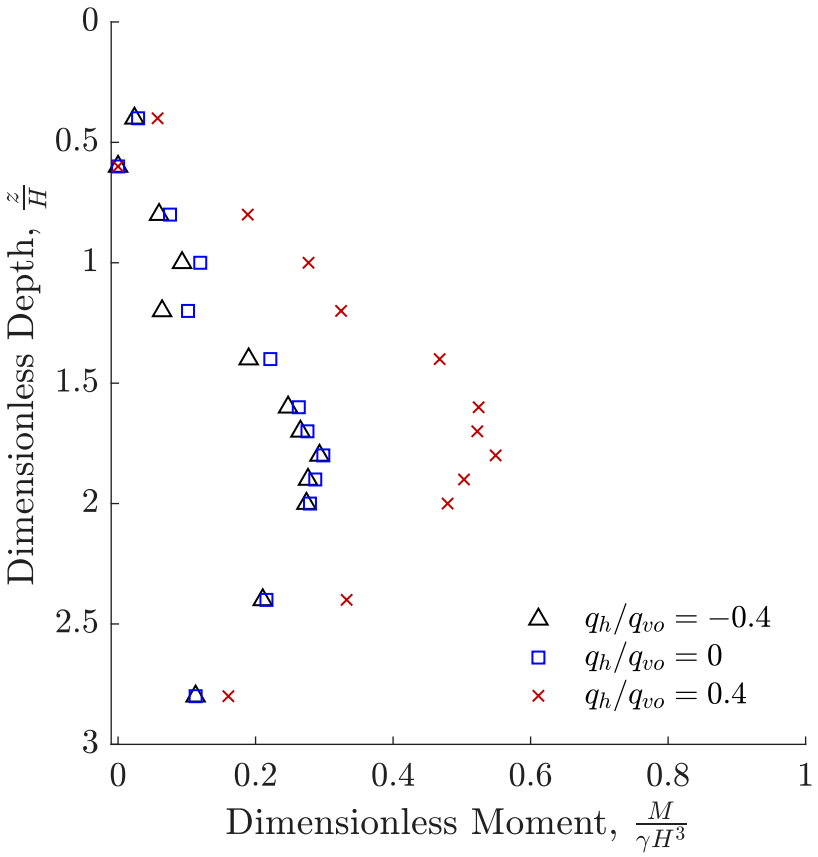

Figure 4.5. Effect of relative horizontal surcharge direction, the sign of $\frac{q_h}{q_{vo}}$, for a constant vertical surcharge, $\frac{q_{vo}}{\gamma H} = 1$, and distance, $\frac{d}{H} = 0.1$. Positive values of $\frac{q_h}{q_{vo}}$ represent horizontal surcharges toward the sheet pile wall, whereas negative values represent surcharges away from the sheet pile wall.

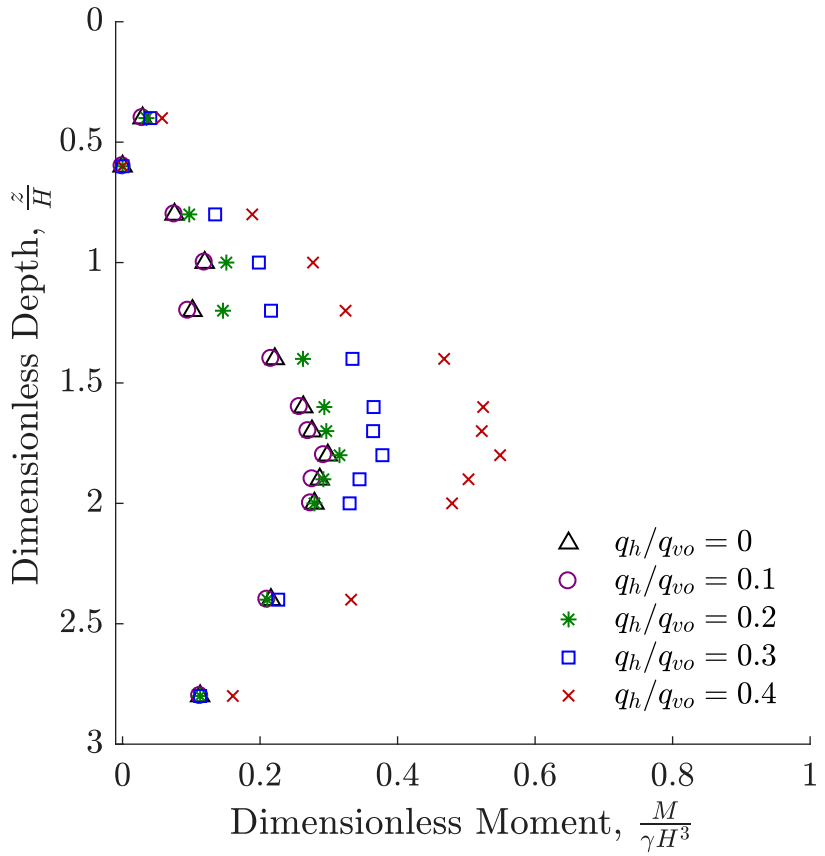

Figure 4.6. Effect of relative horizontal surcharge magnitude, $\frac{q_h}{q_{vo}}$, for a constant relative vertical surcharge, $\frac{q_{vo}}{\gamma H} = 1$, and distance, $\frac{d}{H} = 0.1$.

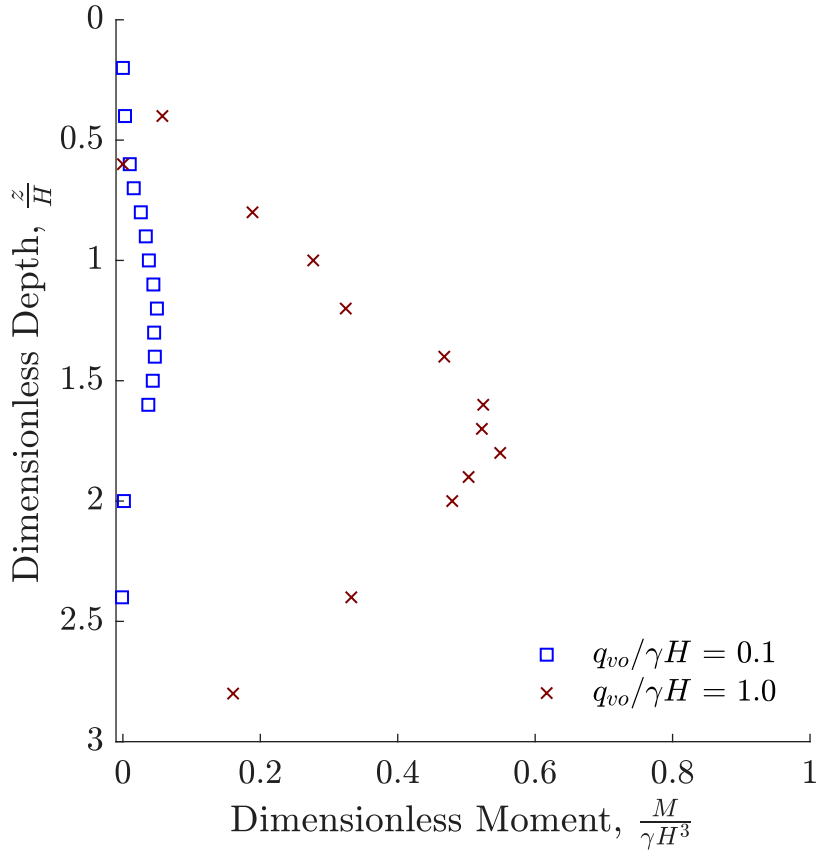

Figure 4.7. Effect of relative vertical surcharge magnitude, $\frac{q_{vo}}{\gamma H}$, for a constant relative horizontal surcharge magnitude, $\frac{q_h}{q_{vo}} = 0.4$, and distance, $\frac{d}{H} = 0.1$.

4.5 Comparison of Predicted and Measured Bending Moment Response

To quantify the effects of the combined surcharge from both vertical and horizontal loading, three main methods were considered: the proposed limit equilibrium solution, an elastic method and an approximate method from AASHTO. The proposed limit equilibrium method is described in detail in Chapter 3 and incorporates the effects of both horizontal/vertical surcharges, applied moments, and the self-weight of the soil simultaneously. To calculate the induced horizontal stress for the surcharge, the effect of the self-weight of the soil was removed, as described in Section 3.1. The elastic method uses a combination of individual elastic solutions provided in

Poulos and Davis (1974) for uniform vertical, uniform horizontal, and linearly varying vertical surcharges (see Section 2.3.1 for more details). These elastic solutions were then superimposed onto active pressures from traditional Coulomb or Rankine solutions to account for soil self-weight. The AASHTO approximate method uses two approximations to estimate the induced lateral pressures from surcharge: one for the effect of the vertical surcharge and the other for the effect of the horizontal surcharge. These induced lateral earth pressures were then added to the lateral earth pressure from self-weight calculated from Coulomb or Rankine's solutions, like the elastic method. The AASHTO approximate method does not consider the effect of applied moment. Figures 4.8 and 4.9 show a typical comparison of the induced horizontal stresses from the surcharge for each of these three methods for small and large values of d, respectively.

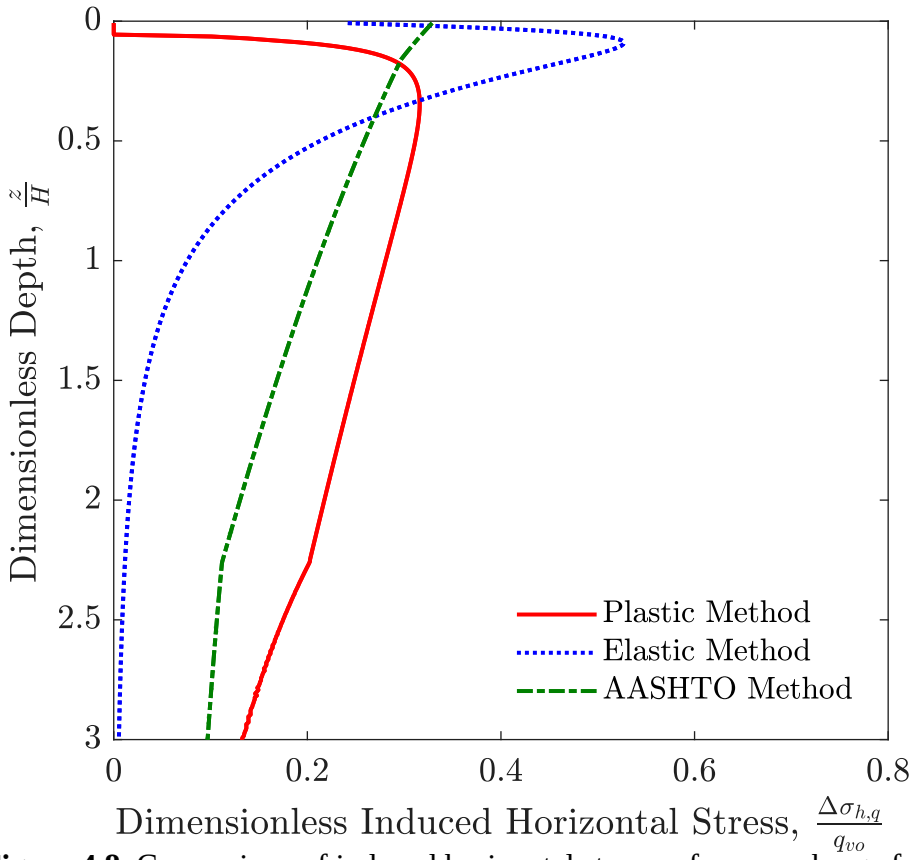

Figure 4.8. Comparison of induced horizontal stresses from surcharge for each method for $\frac{d}{H} = 0.1$, $\frac{q_h}{q_{vo}} = 0.1$, and $\frac{q_{vo}}{\gamma H} = 1$.

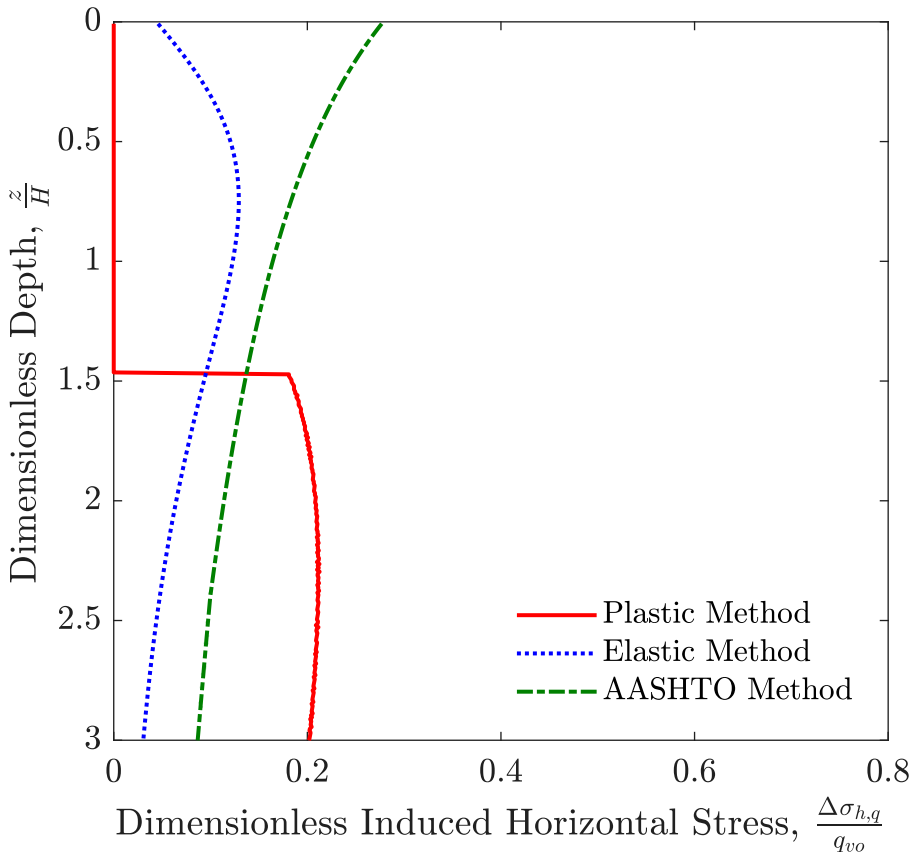

Figure 4.9. Comparison of induced horizontal stresses from surcharge for each method for $\frac{d}{H} = 1.2$, $\frac{q_h}{q_{vo}} = 0.1$, and $\frac{q_{vo}}{\gamma H} = 1$.

The bending moment response from lateral earth pressure methods, with both the self-weight and the surcharge, were compared with the results of the experimental testing. The predicted bending moments from each of the three methods were determined by relating lateral pressure to internal shear force and internal shear force to bending moment, both by way of numerical integration as described in Section 4.3. For depths below the excavation, i.e., $\frac{z}{H} > 1$, the traditional passive pressures from Coulomb and Rankine's theories were assumed, but corrected on the excavation side of the retaining wall as recommended by Caquot and Kerisel (1948). The net lateral earth pressures were then used for integration below the excavation. Since the net lateral earth pressure distribution near the bottom of flexible cantilever retaining walls is complex (Figure 2.12), the

bending moment response for each of the methods is only plotted up to the point of maximum bending moment.

A typical comparison of predicted dimensionless bending moments with experimental testing are shown in Figure 4.10 and 4.11 for small and large values of d, respectively (see Appendix D for the entirety of comparisons). As Figure 4.10 illustrates, the AASHTO method and the proposed plastic limit equilibrium solution from Chapter 3 provide comparable, accurate predictions for $\frac{d}{H} = 0.1$, and the elastic method significantly overpredict. For larger values of $\frac{d}{H}$, however, only the plastic limit equilibrium solution provides an accurate prediction and both the AASHTO and elastic methods significantly overpredict the observed response (Figure 4.11). Table 2 compares

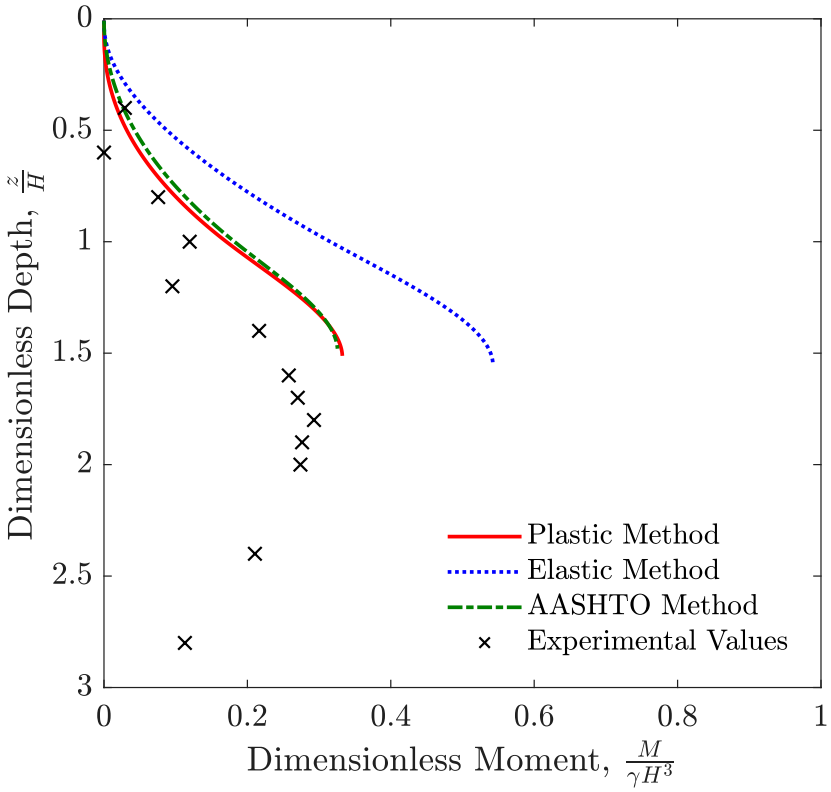

Figure 4.10. Comparison of observed and predicted dimensionless moments for each of the three methods for $\frac{d}{H} = 0.1$, $\frac{q_h}{q_{vo}} = 0.1$, and $\frac{q_{vo}}{\gamma H} = 1$.

the measured maximum bending moment observed during experimental testing with the maximum bending moment predicted by each of the three methods.

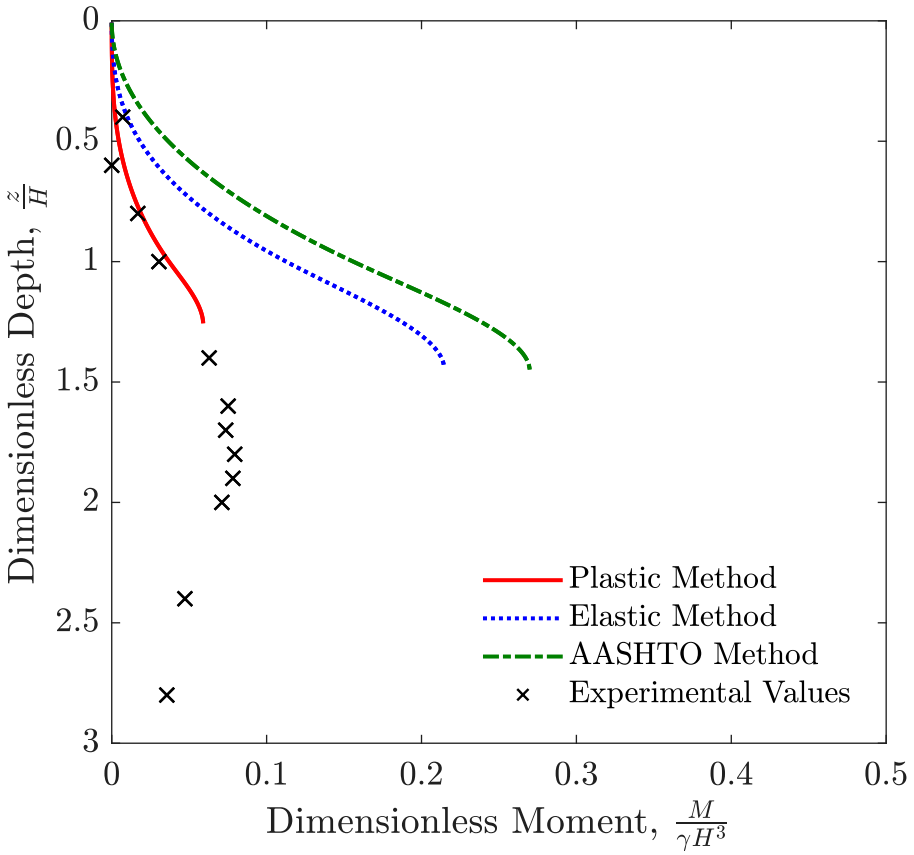

Figure 4.11. Comparison of observed and predicted dimensionless moments for each of the three methods for $\frac{d}{H} = 0.1$, $\frac{q_h}{q_{vo}} = 0.1$, and $\frac{q_{vo}}{\gamma H} = 1$.

Table 2. Comparison of the measured and predicted maximum bending moments for each of the methods.

Relative Distance, d/H	Relative Horizontal Surcharge, q_h/q_{vo}	Relative Vertical Surcharge, $q_{vo}/\gamma H$	Maximum Dimensionless Bending Moment, $\frac{M}{\gamma H^3}$			
			Experimental Measurement	Proposed Limit Equilibrium Method	Elastic Method	AASHTO Method
1.2	0.3	1	0.12	0.06	0.39	0.40
1.2	0.1	1	0.08	0.06	0.21	0.27
0.4	0.3	1	0.22	0.31	0.75	0.50
0.4	0.1	1	0.18	0.18	0.40	0.29
0.4	0.1	0.1	2.5×10^{-2}	4.4×10^{-2}	6.8×10^{-2}	5.8×10^{-2}
0.1	0.3	1	0.38	0.54	1.00	0.58
0.1	0.1	1	0.29	0.33	0.54	0.33
0.1	0.1	0.1	3.9×10^{-2}	5.7×10^{-2}	8.1×10^{-2}	5.9×10^{-2}

4.6 Discussion

When comparing the three methods, the proposed limit equilibrium method most accurately predicted the bending moments from experimental measurements and ultimately the lateral earth pressures from complex surcharge loading, regardless of the distance between the surcharge and retaining wall. The AASHTO method also provides accurate predictions when the surcharge is right at the wall, but is not accurate for the intermediate and large values of d ($\frac{d}{H} = 0.4$ and $\frac{d}{H} = 1.2$, respectively). One reason that the proposed method provides better prediction originates from how the method treats the distance, d, between the surcharge and the retaining wall. While the AASHTO and elastic method both predict induced stresses from the surcharge immediately below the top of the wall regardless of the value of d, the proposed method predicts a delay in

induced stress from the surcharge and the noise wall will not affect the lateral earth pressures for some depth. This difference results in dramatic differences in bending moments predicted by each method, as shown in Figure 4.11 (more comparisons made in Table 2 and Appendix D).

Since the proposed limit equilibrium solution has been shown to most accurately model the effect of the surcharge loading, this solution can be used to explain three notable trends found in the experimental testing. First, closer distances between the surcharge loading and the retaining wall (i.e., smaller values of d) result in higher bending moments as shown in Figures 4.3 and 4.4. As Figure 3.3 shows, smaller values of d do not produce higher induced stresses from the surcharge, but rather result in shallower depths at which the surcharge begins to influence lateral earth pressures. This shallower depth of influence ultimately leads to higher values of bending moment.

The next trend that can be seen from experimental testing is that the addition of horizontal loading *towards* the retaining wall causes a significant increase to the bending moments from lateral earth pressure (Figure 4.5 and Figure 4.6). As higher surcharge loads are transmitted from the noise wall to the underlying soil, more lateral thrust and ultimately higher lateral pressures to the retaining wall are produced. Conversely, horizontal loading *away* from the retaining wall has no discernible effect, positive or negative, on bending moment, as shown in Figure 4.5. This was the case for all combinations of d and q_{vo}, as show in in Appendix C. This observation does not match the results of the proposed limit equilibrium formulation from Chapter 3 (Figure 3.6). The limit equilibrium formulation predicts horizontal loads directed away from the retaining wall will lessen the lateral earth pressure and therefore result in smaller values for bending moment. This suggests that the proposed limit equilibrium solution does not sufficiently model the effects of the horizontal loading when the loading is directed away from the retaining wall and therefore

should not be used for this loading case. However, for the case of wind loading on noise wall barriers, the wind loading may be in either direction, and the most adverse load is desired for design. Since the loading case that produces the highest bending moments from lateral earth pressures is clearly when the horizontal loading is applied towards the retaining wall according to these results, the failure of the proposed solution in accurately predicting the surcharge effects is of no consequence.

The final trend exhibited by experimental results is that increasing the vertical surcharge magnitude, q_{vo}, produces much larger bending moments (Figure 4.7). As was the case for the horizontal surcharge, higher vertical surcharge loading transmits higher lateral pressures to the retaining wall. These results match those from similar experimental testing on the effect of vertical surcharge loading (Georgiadis and Anagnostopoulos 1998).

Apart from the three general trends above, other important observation can be made as well. As discussed in Section 2.2, wall flexibility plays an important role on the behavior of cantilever retaining wall (Figure 2.12). Two wall flexibilities were used during testing: a thin, more flexible wall for the lower surcharge magnitude testing ($\frac{q_{vo}}{\gamma H} = 0.1$) and a thicker, more rigid wall for the higher surcharge magnitude testing ($\frac{q_{vo}}{\gamma H} = 1$). As Figures 4.7 shows, the two walls have distinctly different bending moment responses. Although two variables are varied here (the flexural rigidity and the surcharge magnitude), bending moment distribution can be compared. The more flexible wall reaches its maximum moment at $\frac{d}{H} = 1.2$ and the bending moment response drops to near zero by $\frac{d}{H} = 2.4$. Conversely, the more rigid wall reaches its maximum moment at much deeper depth of around $\frac{d}{H} = 1.8$ and the bending moment response persists to the bottom of the sheet pile. Recalling the wall flexibility discussion in Figure 2.12, the

experimental tests for the flexible and rigid walls behave in accordance to the fixed- and free-earth support scenarios, respectively. As retaining walls are designed to be relatively stiff to restrict deflections at the top of the wall, the results for the rigid wall are more applicable to the expected behavior of prototype cantilever retaining walls under combined horizontal and vertical surcharge loading.

Apart from the effects of wall flexibility, information was obtained regarding the threshold of whether the surcharge influences the retaining wall. Figure 4.3 shows that the loading case where $d/H = 1.2$ and $\frac{q_{vo}}{\gamma H} = 0.2$ has no discernible effect on the bending moment even with $\frac{q_h}{q_{vo}}$ at its maximum value of 0.4. However, for the higher vertical surcharge magnitude ($\frac{q_{vo}}{\gamma H} = 1$ in Figure 4.3), there is a significant change in bending moment for the same value of $\frac{d}{H}$. This suggests two things: (1) a threshold exists where beyond a certain combination of parameters, namely d, ϕ, q_h, and q_{vo}, the surcharge will no longer influence the lateral pressures along the retaining wall and (2) geometry alone, i.e., the value of d, does not solely control this threshold.

This threshold can be explained by the differing depths at which the surcharge begins to influence the retaining wall between the high and low magnitude vertical surcharge. Figure 4.10 shows the induced horizontal stresses for each of the vertical surcharge magnitudes when $\frac{d}{H} = 1.2$. No significant change in bending moment was recorded when $\frac{q_{vo}}{\gamma H} = 0.1$ (dotted blue line), but a significant change in bending moment was recorded for $\frac{q_{vo}}{\gamma H} = 1$ (solid red line) because the depth at which the surcharge begins to influence the retaining wall is shallower. This also suggests that the threshold at which the surcharge begins to induce stress on the retaining wall lies somewhere between $\frac{z}{H} \cong 1.6$ where the surcharge does influence and $\frac{z}{H} \cong 2.2$ where the

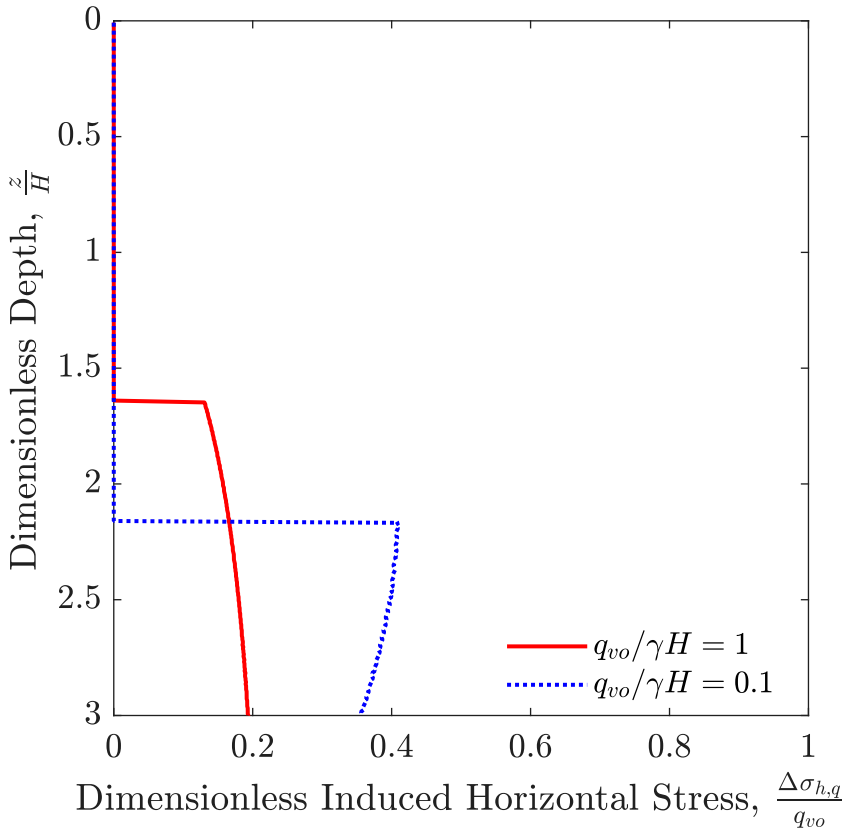

Figure 4.12. Induced stresses when $\frac{d}{H} = 1.2$ for each of the vertical surcharge magnitudes.

surcharge does not influence the bending moment. It is important to note that the surcharge can influence the retaining wall even when the depth to influence is below the elevation of the excavation, i.e., $\frac{z}{H} = 1$. Ultimately, it is of the opinion of the author that the threshold depth of influence is at the point of fixity at which the flexible retaining wall either rotates or is fixed according to the free- or fixed-earth support case, respectively (Figure 2.12). This pivot point lies somewhere below the excavation but above the bottom of the pile. The rationale for this point is that if the surcharge influences above the point of fixity, the induced stresses from the surcharge will promote movement of the top of the sheet pile wall toward the excavation. If the surcharge begins to influence below the point of fixity, the induced stresses from the surcharge will either have no effect for the fixed-earth case or promote rotation of the top of the sheet pile away from

the excavation effectively stabilizing the retaining wall for the free-earth case. More research should be conducted to confirm this hypothesis.

4.7 Lessons Learned

A small-scale, 1-g retaining wall model was used to test the effects of several parameters related to horizontally and vertically loaded surcharge placed near a model sheet pile wall. These parameters included the distance between the surcharge and the retaining wall, d, the horizontal surcharge magnitude, q_h, and the vertical surcharge magnitude, q_{vo}. To isolate each of these variables, combinations of each of these parameters was tested. Measurements were made via strain gauges placed at various depths along the model sheet pile wall and were converted to bending moments. The bending moment results from the experimental testing were compared with the predicted bending moments from net lateral earth pressures from three different methods: the proposed limit equilibrium solution from Chapter 3 and the elastic and AASHTO methods described in Chapter 2. Key conclusions are as follows:

a) Due to the very low confining pressures present in the small-scale model, significant dilative effects were observed. This is a limitation of the experimental model that does not simulate the confining pressures expected in prototype cantilever retaining walls.
b) Smaller values of d, larger values of q_h, and larger values of q_{vo} produced larger bending moments.
c) When q_h was negative, i.e., the horizontal loading was directed away from the retaining wall, no significant change in bending moment was recorded.
d) When comparing the observed experimental bending moment results with bending moments predicted via the three methods, the proposed limit equilibrium solution provided accurate predictions for all surcharge distances (d). The AASHTO method

provided accurate predictions when the noise wall was at the retaining wall (small values of d) but greatly overpredicted the response for intermediate and large surcharge distances. The elastic method gave the least accurate predictions for all load cases.

e) The relative flexibility of the wall had a significant effect on the bending moment response between the more flexible wall under lower magnitude vertical surcharge loading and the more rigid wall under the higher magnitude vertical surcharge. The bending moment response of the more flexible wall reflected the fixed-earth support response, while the more rigid wall better reflected the free-earth response presented in Figure 2.12. These results were consistent with the results of Rowe (1952).

f) It is the opinion of the author that the threshold that decides whether the surcharge will or will not influence the retaining wall is governed by the depth at which the surcharge begins influencing the wall. This depth is a complex function dependent primarily on the horizontal and vertical surcharge magnitudes, q_h and q_{vo}, respectively, and the distance between the surcharge loading and the retaining wall, d. If this depth is above the point of fixity for the wall, the surcharge will influence the retaining wall. If this depth is below the point of fixity, the surcharge will not adversely affect the lateral earth pressures on the retaining wall.

5 Conclusions

The goal of this thesis was to determine a more accurate method of evaluating the effect of horizontal surcharges and non-uniform vertical surcharge loading behind flexible cantilever retaining walls. A literature review was performed that began with lateral earth pressures from the self-weight only and progressed into applied lateral pressures from surcharge loading. As a result of this literature review, a plasticity-based, limit equilibrium solution was proposed that accounted for horizontal and non-uniform vertical surcharges.

The proposed limit equilibrium solution was determined to have four main controlling dimensionless parameters: the distance, $\frac{d}{H}$, between the surcharge and the retaining wall, the friction angle, ϕ, the magnitude of the applied horizontal surcharge, $\frac{q_h}{q_{vo}}$, and the magnitude of the applied vertical surcharge, $\frac{q_{vo}}{\gamma H}$. Analysis of the effects of these parameters found that decreasing d or ϕ, and increasing q_h or q_{vo} caused increased lateral pressures and corresponding bending moments, according this proposed limit equilibrium solution.

A small-scale experimental model was constructed and used to assess the validity of the proposed limit equilibrium solution. Two walls were tested with a different flexibility, each instrumented with a set of strain gauges to quantify the bending moment response. The more rigid wall was used for higher vertical surcharge loading and the more flexible wall was used for lower vertical surcharge loading. The measured bending moment response for different loading conditions (i.e., varying combinations of $\frac{d}{H}$, ϕ, $\frac{q_h}{q_{vo}}$, and $\frac{q_{vo}}{\gamma H}$) were then compared to bending moment distributions predicted by the proposed limit equilibrium solution, an elastic solution, and an approximate method from Berg et al. (2009) based on the AASHTO LRFD Bridge

Design Specifications. It was confirmed that the proposed solution most accurately predicted the bending moment response from the applied surcharge loading for any distance between the surcharge and the retaining wall, d. It is ultimately recommended that (1) the proposed limit equilibrium solution be used to quantify the lateral pressures from the horizontal/vertical surcharge loading and (2) that any predicted induced stresses above the point of fixity be used for lateral earth pressure analysis.

References

Berg, R. R., Barry, R. C., and Samtani, N. C. (2009). *Design and Construction of Mechanically Stabilized Earth Walls and Reinforced Soil Slopes – Volume 1*, U.S. Department of Transportation, Report FHWA-NHI-10-024. Washington, D.C.

Bica, A.V.D, and Clayton, C. R. I. (1989). "Limit equilibrium design methods for free embedded cantilever walls in granular materials." *Proceedings of the Institution of Civil Engineers, 86(5)*, 879-898.

Bolton, M. D. (1986). "Strength and dilatancy of sands." *Geotechnique*, 36(1), 65-78.

Bowles, J. E. (1996). *Foundation Analysis and Design*, McGraw-Hill. Fifth Edition

Butterfield, R. (1999). "Dimensional analysis for geotechnical engineers." *Geotechnique*, 49(3), 357-366.

Caquot, A. & Kerisel, J. (1948). Tables for the Calculation of Passive Pressure, Active Pressure and Bearing Capacity of Foundation. Gauthier-Villars, Paris.

Cornforth, D. H. (1973). "Prediction of Drained Strength of Sands from Relative Density Measurements." *Evaluation of Relative Density and its Role in Geotechnical Projects Involving Cohesionless Soils*, STP523-EB, ASTM International, West Conshohocken, PA.

Coulomb, C. A. (1776). "Essai sur une application des regles des Maximis et Minimis a quelques problemes de Statique relatifs a l'Architeture." *Memoirs Academie Royal Pres. Division Sav. 7*, Paris, France (in French).

Federal Highway Administration (FHWA). (2001). “Keeping the Noise Down – Highway Traffic Noise Barriers.” *Highway Traffic Noise*. <https://www.fhwa.dot.gov/environment/noise/noise_barriers/>. (Mar. 24, 2019).

Federal Highway Administration (FHWA). (2019). “State Specific Summary Tables - Wisconsin.” *Highway Traffic Noise*. <https://www.fhwa.dot.gov/environment/noise/noise_barriers/>. (April 16, 2019).

Georgiadis, M. and Anagnostopoulos, C. (1998). “Lateral Pressure on sheet pile walls due to strip load, *J. Geotech. Geoenviron. Eng.*, ASCE, 124(1), 95-98.

Greco, V. R. (2006). “Lateral earth pressure due to backfill subject to a strip of surcharge.” *Geotechnical and Geological Engineering*. 24(3), 615-636.

Hansen, J. B. (1953). “Earth Pressure Calculation, The Danish Technical Press.” *The Institution of Danish Civil Engineers Copenhagen*.

Jarquio, R. (1981). “Total lateral surcharge pressure due to a strip load.” *J. Geotech. Engrg. Div.*, ASCE, 107(10), 1424-1428.

Kaseloo, P. A., Tyson, K. O. (2004). *Synthesis of Noise Effects on Wildlife Populations*. Federal Highway Administration, Report No. FHWA-HEP-06-016, McLean, Virginia.

King, G. J. W. (1995). “Analysis of Cantilever Sheet-Pile Walls in Cohesionless Soil.” *J. Geotech. Engrg*. 121(9), 629-635.

Krey, H. (1932). Errduck, Erdwiderstand und Trgfahigkeit des Baugrundes. W. Ernst & Sohn, Berlin.

Leonards, G. A. (1965). *Experimental study of static and dynamic friction between soil and typical construction materials*. Air Force Weaponry Laboratory, Report No. AFWL-TR65-161.

Misra, B. (1980). “Lateral pressures on retaining walls due to loads on surface of granular backfill.” *Soils and Found*. Tokyo, Japan, 20(2), 33-44.

Motta, E. (1994). “Generalized Coulomb active-earth pressure for distanced surcharge.” *J. Geotech. Engrg.*, ASCE, 120(6), 1072-1079.

Naval Facilities Engineering Command. (1982). “Foundations and Earth Structures.” *NAVFAC Design Manual DM-7.2*. Alexandria, VA.

Poncelet, J. V. (1840) “Mémoire sur la stabilité des revêtements et de leurs fondations, par M. Poncelet,...” Bachelier.

Poulos, H. G., and Davis, E. H. (1974). *Elastic solutions for soil and rock mechanics*. John Wiley.

Rankine, W. J. M. (1857). “II. On the stability of loose earth.” *Philosophical transactions of the Royal Society of London*, (147), 9-27.

Rowe, P. W. (1952). “Anchored Sheet-Pile Walls.” *Proceeding of the Institute of Civil Engineers*. 1(1), 21-70.

United States Steel (USS). (1984). *Steel Sheet Pile Design Manual.*

Santamarina, J. C., and Cho, G. C. (2001). “Determination of Critical State Parameters in Sandy Soils – Simple Procedure.” *Geotechnical Testing Journal*. American Society of Testing and Materials, 24(2), 185-192.

Singh, D., Kumari, N., and Sharma, P. (2017). “A Review of Adverse Effects of Road Traffic Noise on Human Health.” Fluctuations and Noise Letters, 17(1). 1830001-1-1830001-12.

Spangler, M. G. (1956). “Lateral Pressures on Retaining Walls Due to Backfill Surface Loads.” *Highway Research Board Bulletin*. (141). 1-18.

Steenfelt, J.S., and Hansen, J.B. (1983) “Discussion of ‘Total lateral surcharge pressure due to strip load,’ by R. Jarquio.” *J. Geotech. Engrg.*, ASCE, 109(2), 271-273.

Terzaghi, K. (1951). *Theoretical Soil Mechanics*, Chapman and Hall, Limited. London.

Terzaghi, K. (1954). “Anchored Bulkheads.” *Transactions of the ASCE*, 119(1), 1243-1280.

Wang, C. D. (2005). “Lateral stress caused by horizontal and vertical surcharge strip loads on a cross-anisotropic backfill.” *International Journal for Numerical and Analytical Methods in Geomechanics*, 29(14), 1341-1361.

Appendix A: Derivation of Proposed Limit Equilibrium Solution

1. Determine Maximum Thrust, P_{max}, for given depth, z and $\phi \leq \alpha \leq 90°$

Known Relationships

$$R_h = R\sin(\alpha - \phi) \qquad R_v = -R\cos(\alpha - \phi)$$

$$W = \frac{1}{2}\gamma z^2 \cot(\alpha)$$

$P_v = Psin(\delta) \qquad P_h = Pcos(\delta)$

Case 1: Failure Wedge Includes Entire Footprint of Surcharge

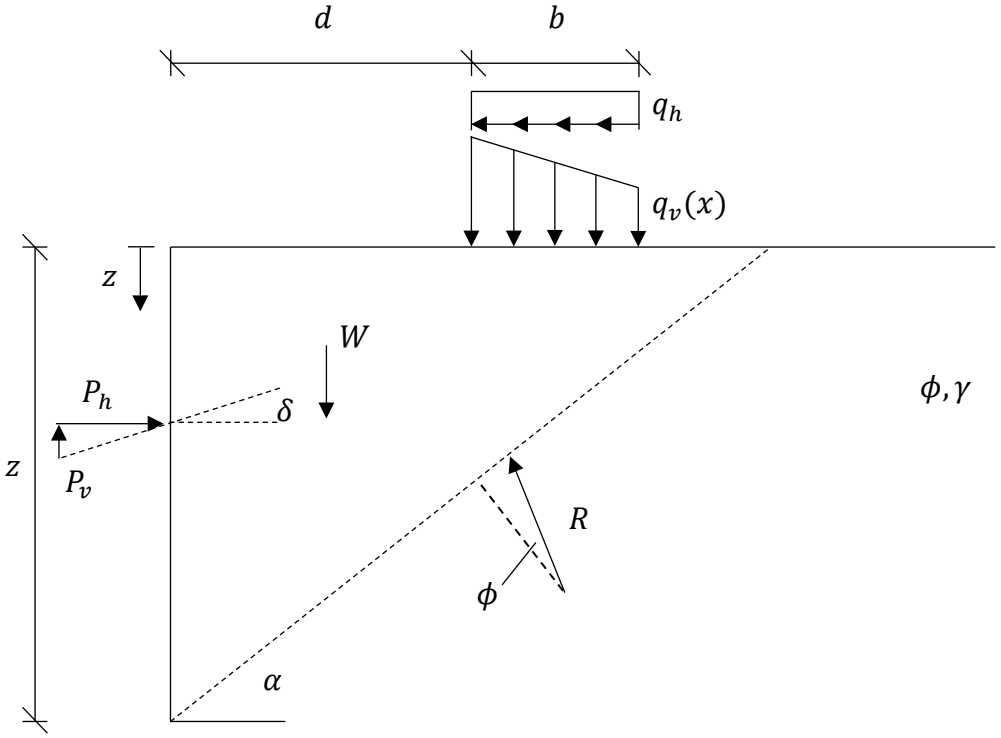

$$\sum F_h = 0 = P_h + q_h b - R_h = P_h - q_h b - Rsin(\alpha - \phi)$$

$$\therefore P = \frac{Rsin(\alpha - \phi) + q_h b}{\cos(\delta)} \tag{1}$$

$$\sum F_v = 0 = P_v - W - q_{vo}b + R_v = P_h \tan(\delta) - W - q_{vo}b + Rcos(\alpha - \phi)$$

$$\therefore P = \frac{W + q_{vo}b - Rcos(\alpha - \phi)}{\sin(\delta)} \tag{2}$$

Setting equations (1) and (2) equal gives:

$$Rsin(\alpha - \phi) + q_h b \quad = \frac{W + q_{vo}b - Rcos(\alpha - \phi)}{\tan(\delta)}$$

Solving for R yields:

$$R = \frac{W + q_{vo}b - q_h b \tan(\delta)}{\tan(\delta)\cos(\alpha - \phi) + \sin(\alpha - \phi)}$$

Substituting into Equation (1):

$$P = \frac{(W + q_{vo}b - q_h btan(\delta))\sin(\alpha - \phi)}{\cos(\delta)\,(\tan(\delta)\cos(\alpha - \phi) + \sin(\alpha - \phi))} + \frac{q_h b}{\cos(\delta)}$$

$$= \big(W + q_{vo}b - q_h btan(\delta)\big)\frac{\sin(\alpha - \phi)}{\cos(\alpha - \phi - \delta)} + \frac{q_h b}{\cos(\delta)} \tag{3a}$$

Note that Equation 3 is only valid for values of α that result in the failure surface intersecting the ground surface at or beyond the far edge of the surcharge, i.e., Case 1. Thus, Equation 3 must be modified to incorporate values of α that result in failure surfaces that include only a portion of the surcharge (Case 2) or excludes the footprint of the surcharge entirely (Case 3).

Case 2: Failure Wedge Includes Portion of Surcharge:

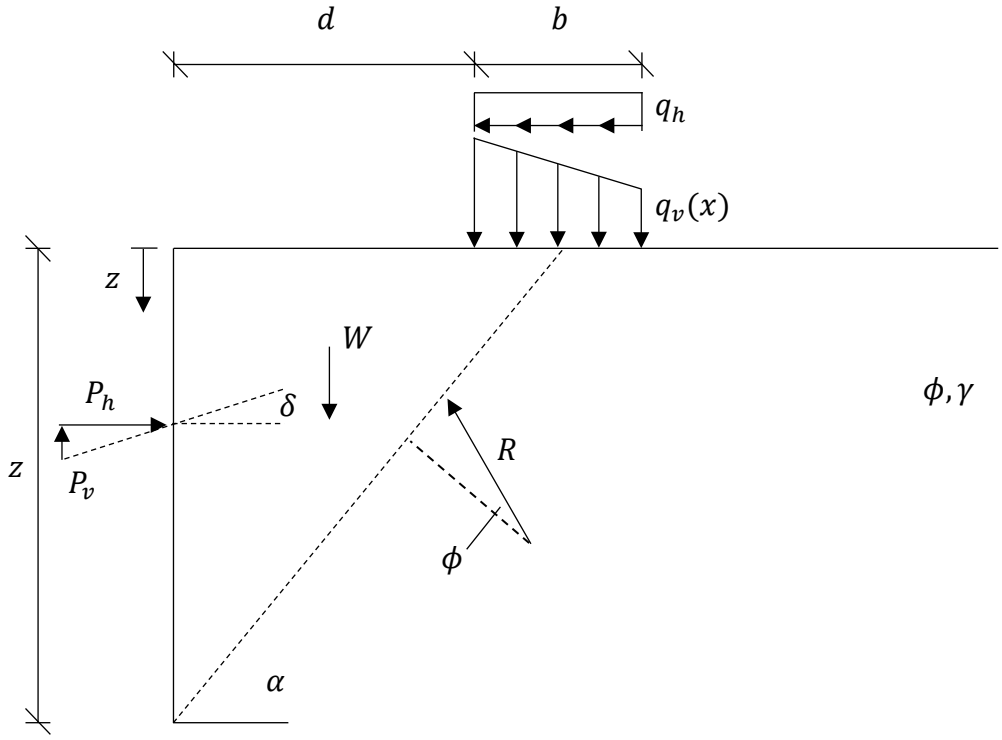

When a portion of the surcharge is included in the wedge, the length of this surcharge portion is equal to:

$$\mathrm{zcot}(\alpha) - \mathrm{d} = x - d$$

Solving for equilibrium leads to

$$\sum F_h = 0 = P_h + q_h z cot(\alpha) - R_h = P_h - q_h z cot(\alpha) - R sin(\alpha - \phi)$$

$$\therefore P = \frac{R sin(\alpha - \phi) + q_h b}{\cos(\delta)} \quad (1)$$

$$\sum F_v = 0 = P_v - W - \int_d^{zcot(\alpha)} q_v(x) + R_v$$

$$= P_h \tan(\delta) - W - \int_d^{zcot(\alpha)} q_v(x) + Rcos(\alpha - \phi)$$

$$\therefore P = \frac{W + \int_d^{zcot(\alpha)} q_v(x) - Rcos(\alpha - \phi)}{\sin(\delta)} \quad (2)$$

Linearly varying vertical surcharge, $q_v(x)$:

$$e = \frac{q_h}{q_{vo}} h = Fh \qquad q_{min} = q_{vo}\left(1 - \frac{6e}{b}\right) \qquad q_{max} = q_{vo}\left(1 + \frac{6e}{b}\right)$$

where:

e = eccentricity from applied moment

h = height of resultant of horizontal force, e.g., wind load

q_{min}, q_{max} = minimum and maximum magnitude of vertical load

Slope: $\frac{q_{min} - q_{max}}{B} = q_{vo}\left(1 - \frac{6e}{B} - 1 - \frac{6e}{B}\right) = q_{vo}\left(-\frac{12e}{B}\right)$

$$q_v(x) = q_{vo}\left[\left(1 + \frac{6Fh}{b} - \frac{12Fhd}{b^2}\right) - \frac{12Fhx}{b^2}\right]$$

$$\int_d^x q_v(x) = \int_d^{zcot(\alpha)} q_v(x) = q_{vo}\left[\left(1 + \frac{6Fh}{b} - \frac{12Fhd}{b^2}\right)(x - d) - \frac{6Fh}{b^2}(x^2 - d^2)\right]$$

$$= (x - d) q_{vo}\left[\left(1 + \frac{6Fh}{b} - \frac{12Fhd}{b^2}\right) - \frac{6Fh}{b^2}(x + d)\right]$$

$$= (x - d) q_{vo} A$$

where $A = \left[\left(1 + \frac{6Fh}{b} - \frac{12Fhd}{b^2}\right) - \frac{6Fh}{b^2}(x+d)\right]$

Setting Equation (1) equal to (2) and solving for P:

$$P = \left[\frac{1}{2}\gamma z^2 f(\alpha) + (zf(\alpha) - d)(Aq_{vo} - \tan(\delta)\, q_h)\right] g(\alpha) + \frac{q_h(zf(\alpha)-d)}{\cos(\delta)}$$

Case 3: Failure Wedge Excludes Surcharge

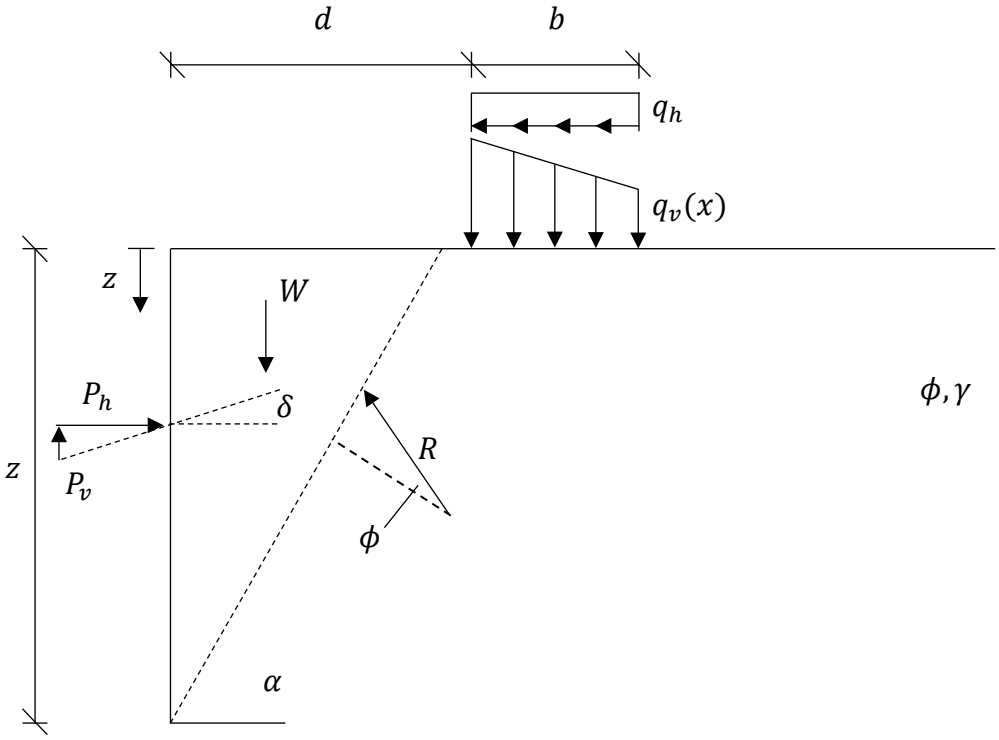

The simplest of all three cases, only self-weight contributes to the thrust, P.

$$\sum F_h = 0 = P_h - R_h = P_h - R\sin(\alpha - \phi)$$

$$\therefore P = \frac{R\sin(\alpha - \phi)}{\cos(\delta)} \qquad (1)$$

$$\sum F_v = 0 = P_v - W + R_v = P_h \tan(\delta) - W + R\cos(\alpha - \phi)$$

$$\therefore P = \frac{W - Rcos(\alpha - \phi)}{\sin(\delta)} \quad (2)$$

Setting (1) and (2) equal and solving for P:

$$P = \frac{1}{2}\gamma z^2 \mathrm{f}(\alpha)\mathrm{g}(\alpha)$$

2. Calculate $P_{h,max}$

$$P_{h,max} = P_{max}\cos(\delta)$$

3. Repeat steps 1 and 2 for all values of z along retaining wall

4. Numerically differentiate $P_{h,max}(z)$ with respect to z to find lateral earth pressure, $\sigma_h(z)$

Appendix B: Effect of Input Parameters on Induced Horizontal Stresses

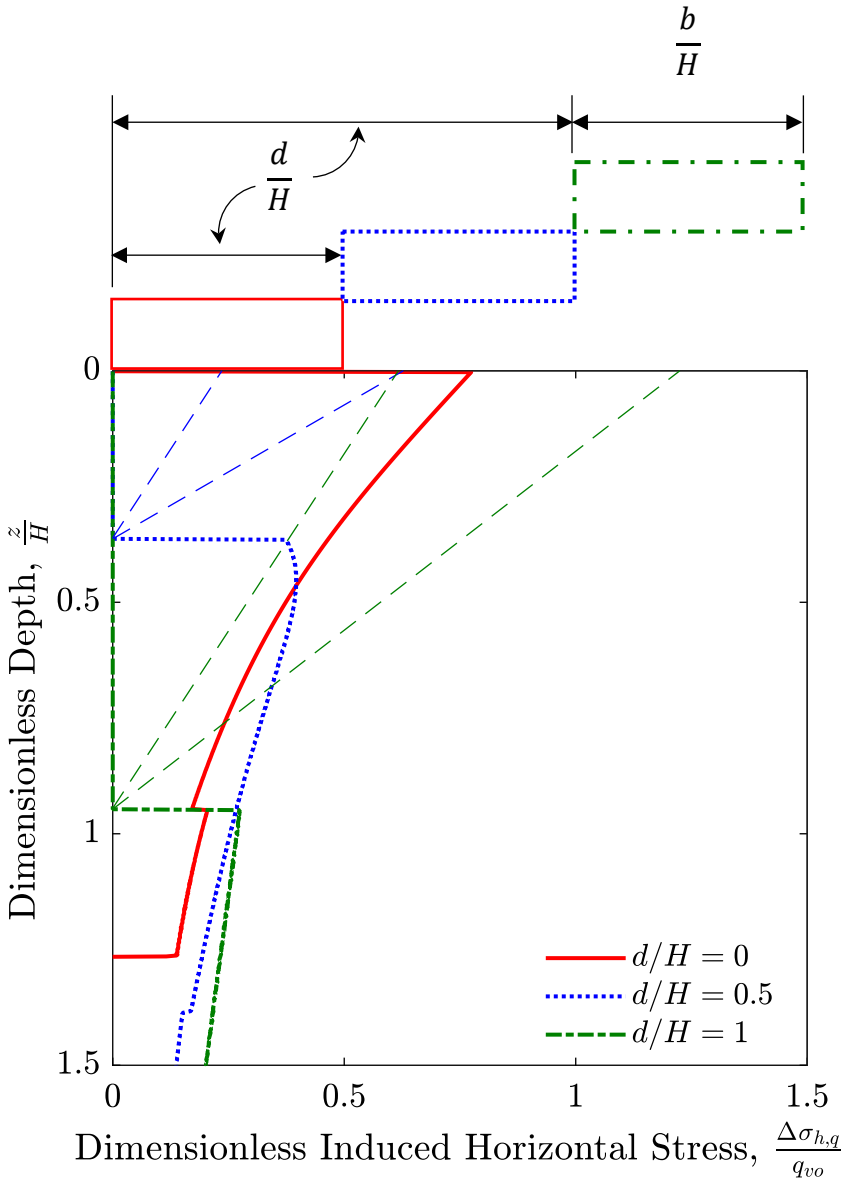

Figure B.1. Effect of distance, $\frac{d}{H}$, on the induced horizontal stress for $\phi = 30°$, $\frac{q_h}{q_{vo}} = 0.3$, $\frac{q_{vo}}{\gamma H} = 0.5$.

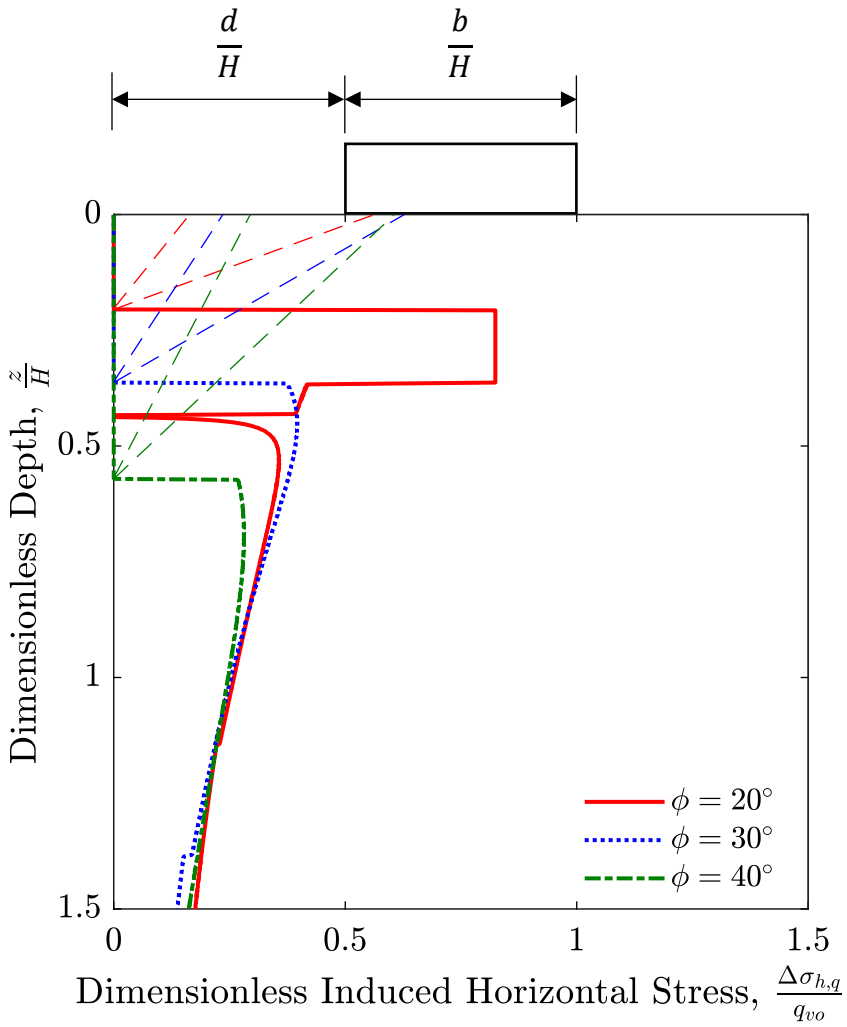

Figure B.2. Effect of friction angle, ϕ, on the induced horizontal stress for $\frac{d}{H} = 0.5$, $\frac{q_h}{q_{vo}} = 0.3$, $\frac{q_{vo}}{\gamma H} = 0.5$.

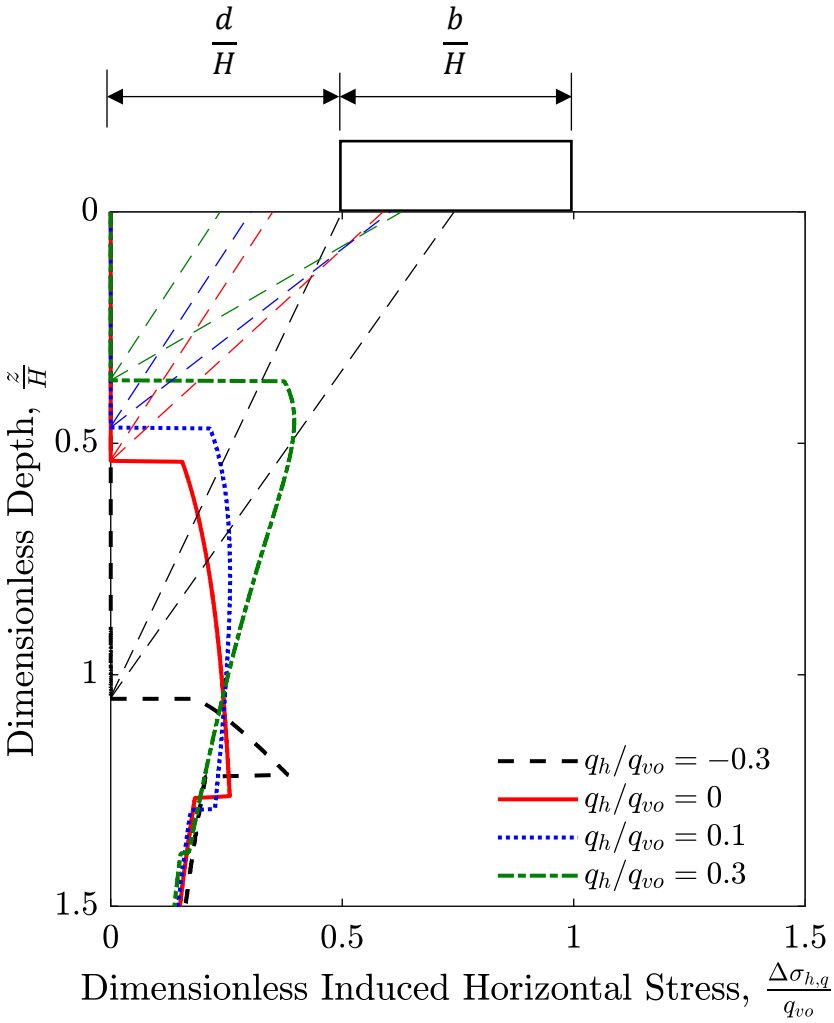

Figure B.3. Effect of horiztonal surcharge magnitude, $\frac{q_h}{q_{vo}}$, on the induced horizontal stress for $\frac{d}{H} = 0.5$, $\phi = 30°$, $\frac{q_{vo}}{\gamma H} = 0.5$.

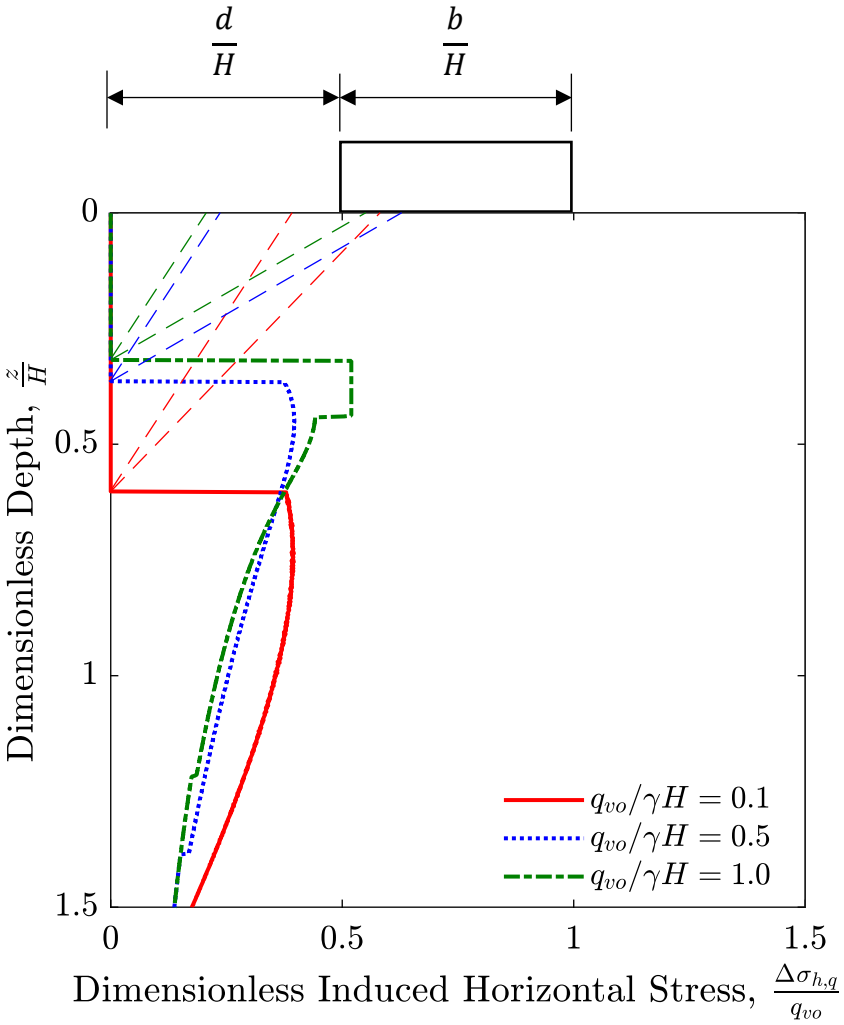

Figure B.4. Effect of vertical surcharge magnitude, $\frac{q_{vo}}{\gamma H}$ on the induced horizontal stress for $\frac{d}{H}$, $= 0.5$ $\phi = 30°$, and $\frac{q_h}{q_{vo}} = 0.3$.

Appendix C: Experimental Results - Bending Moment Response

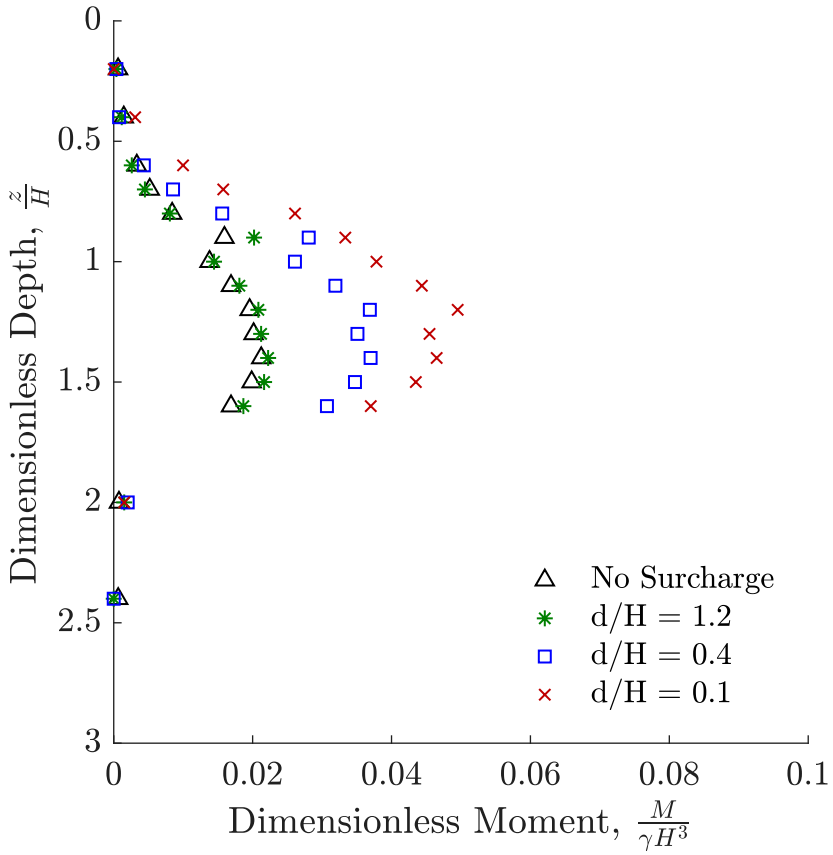

Figure C.1. Results showing effect of distance, $\frac{d}{H}$, for a constant $\frac{q_{vo}}{\gamma H} = 0.1$ and $\frac{q_h}{q_{vo}} = 0.4$.

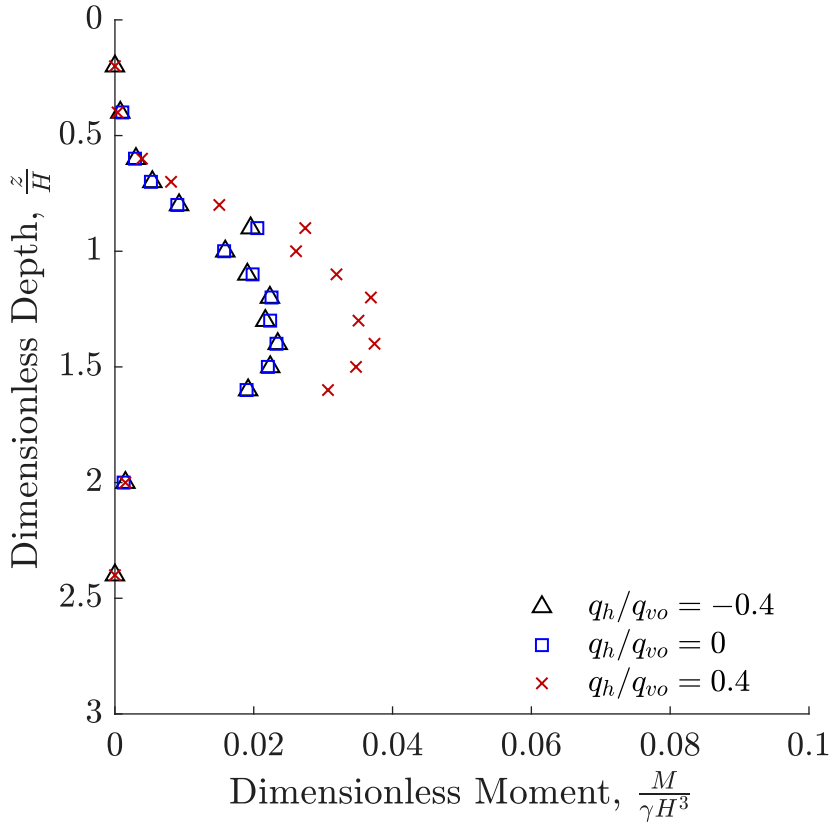

Figure C.2. Results showing effect of q_h direction for a constant $\frac{d}{H} = 0.4$ and $\frac{q_{vo}}{\gamma H} = 0.1$

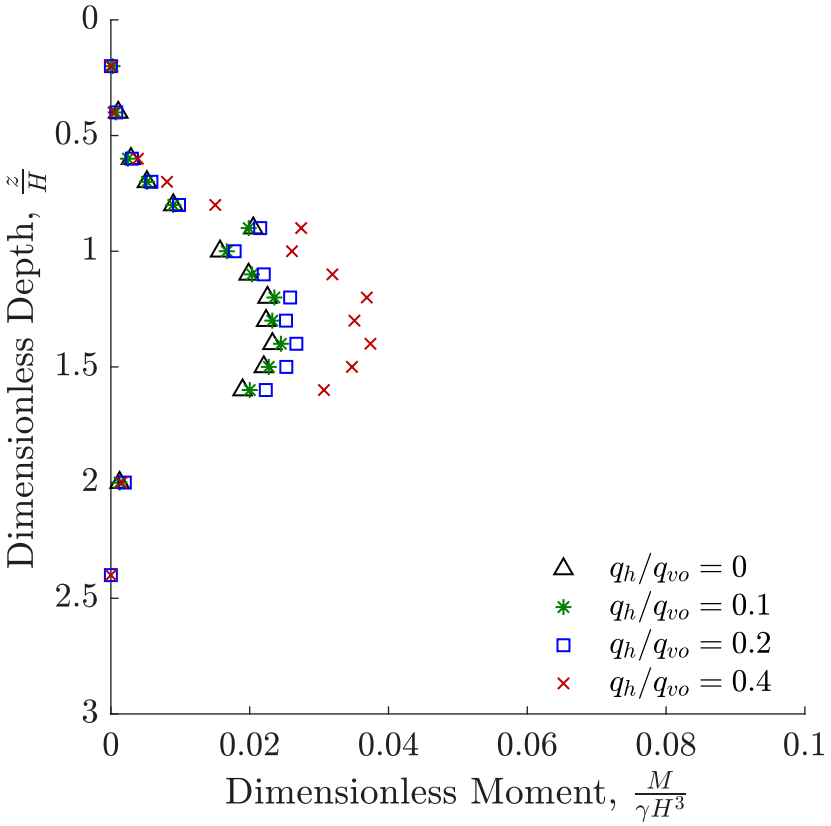

Figure C.3. Results showing effect of positive q_h magnitude for a constant $\frac{d}{H} = 0.4$ and $\frac{q_{vo}}{\gamma H} = 0.1$

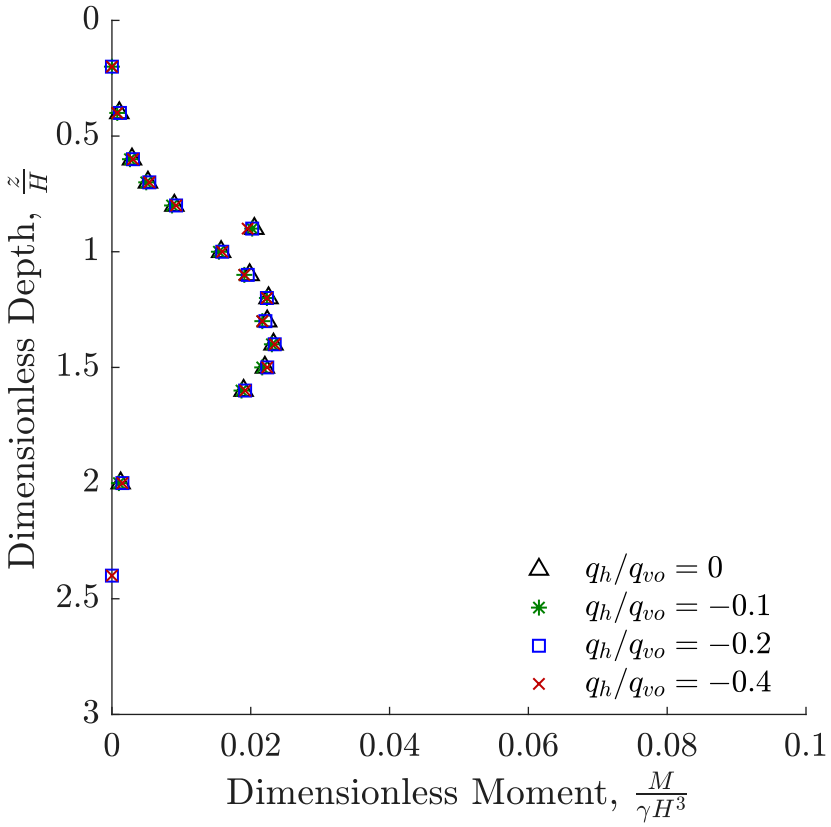

Figure C.4. Results showing effect of negative q_h magnitude for a constant $\frac{d}{H} = 0.4$ and $\frac{q_{vo}}{\gamma H} = 0.1$

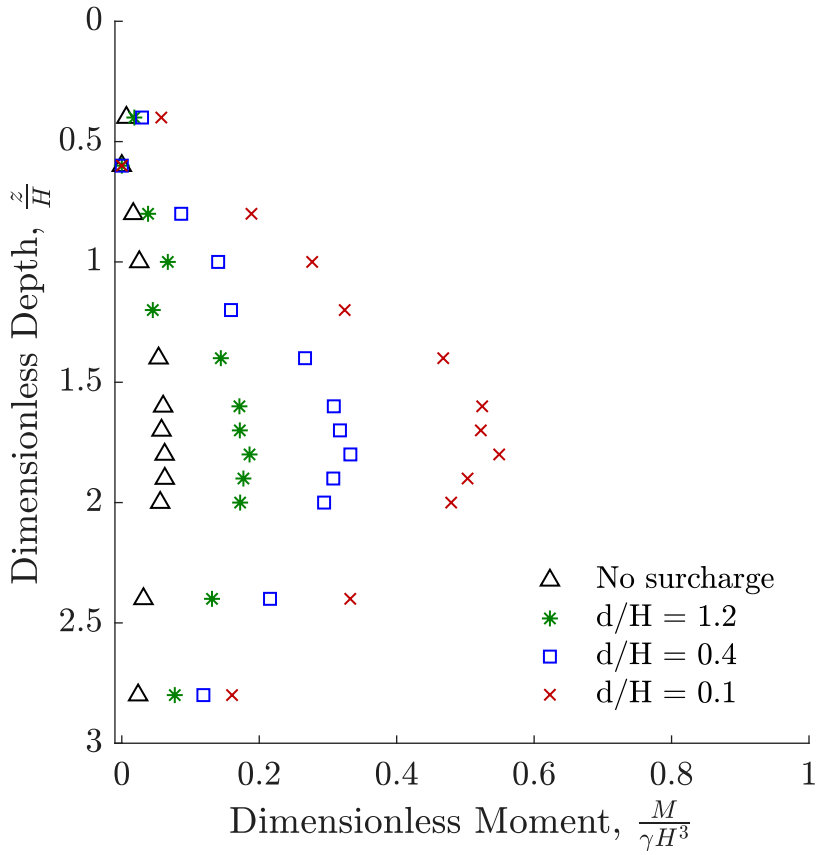

Figure C.5. Results showing effect of distance, $\frac{d}{H}$, for a constant $\frac{q_{vo}}{\gamma H} = 1$ and $\frac{q_h}{q_{vo}} = 0.4$.

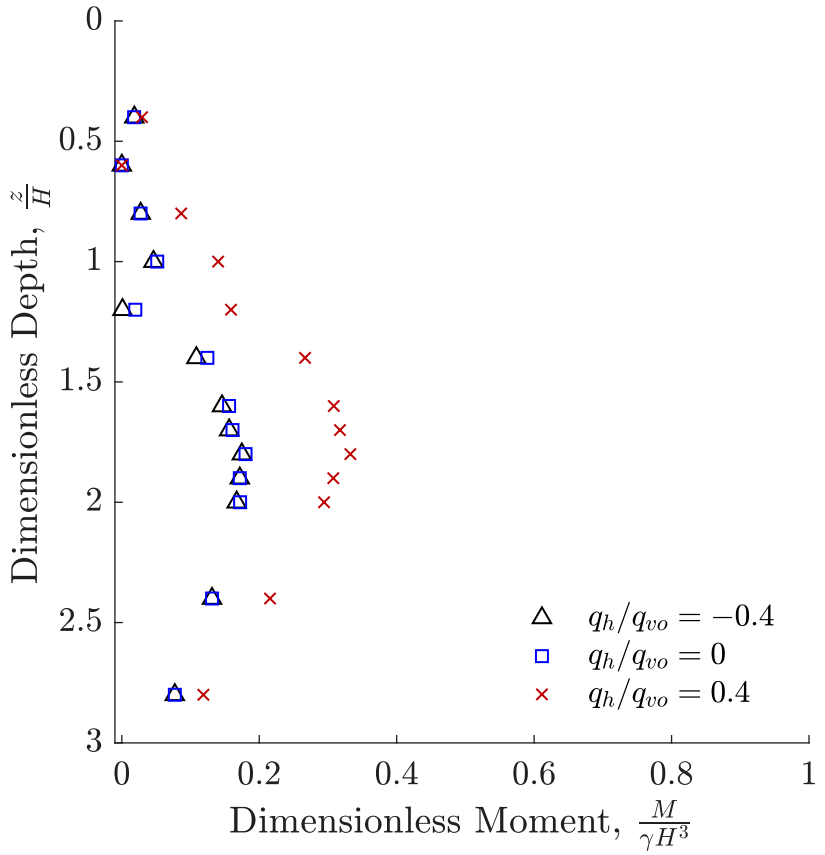

Figure C.6. Results showing effect of q_h direction for a constant $\frac{d}{H} = 0.4$ and $\frac{q_{vo}}{\gamma H} = 1$

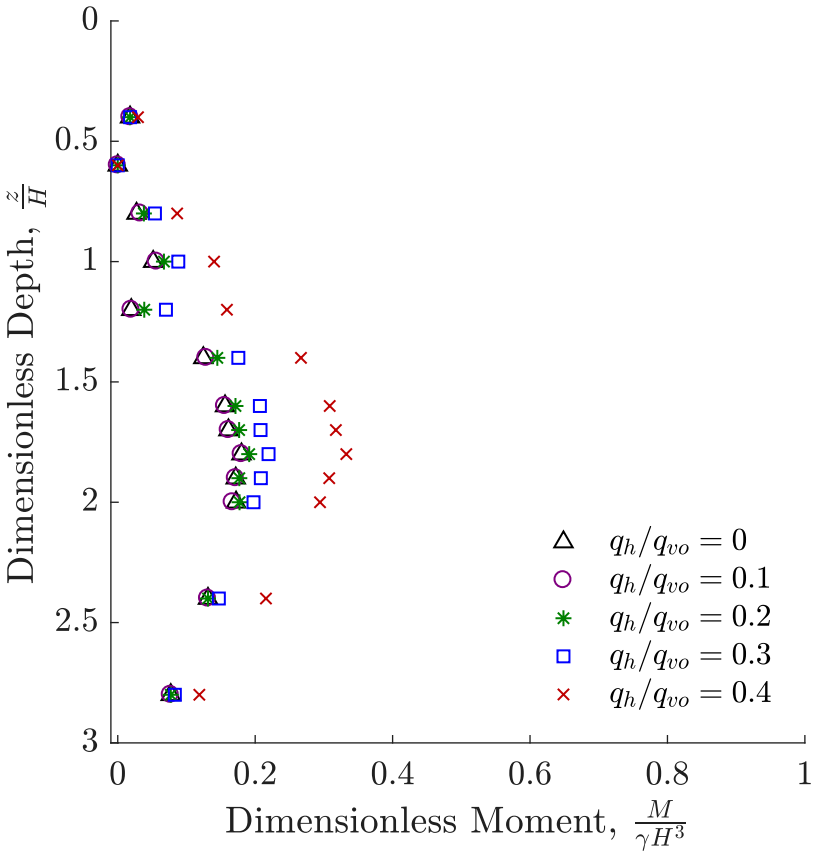

Figure C.7. Results showing effect of positive q_h magnitude for a constant $\frac{d}{H} = 0.4$ and $\frac{q_{vo}}{\gamma H} = 1$

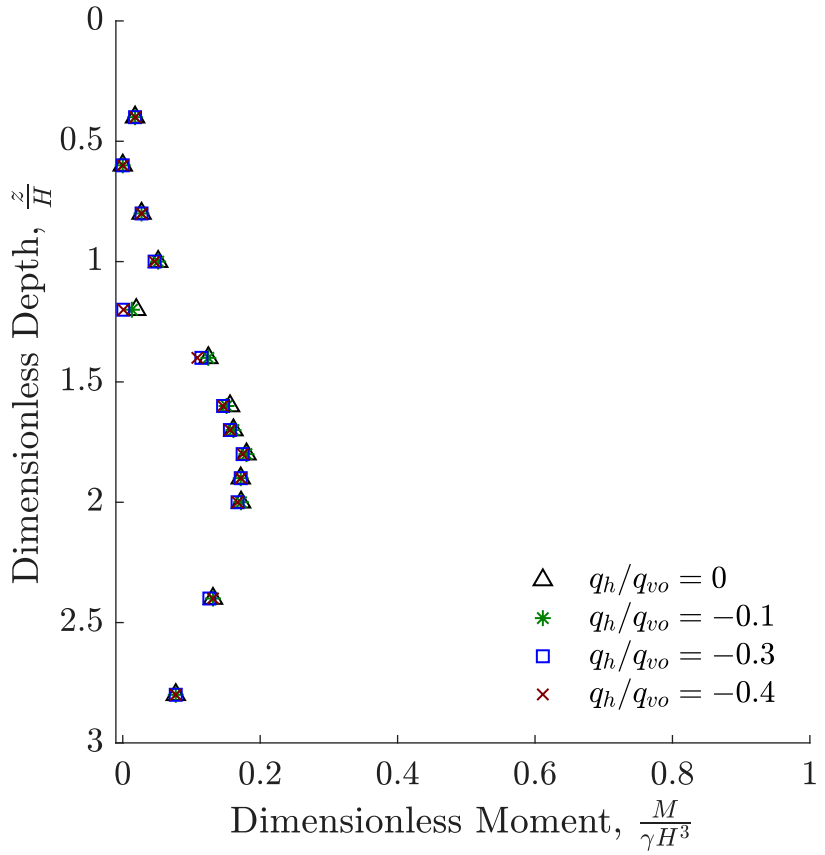

Figure C.8. Results showing effect of negative q_h magnitude for a constant $\frac{d}{H} = 0.4$ and $\frac{q_{vo}}{\gamma H} = 1$

Appendix D: Comparison of Methods for Surcharge Lateral Pressures

Induced Horizontal Stresses from Surcharge

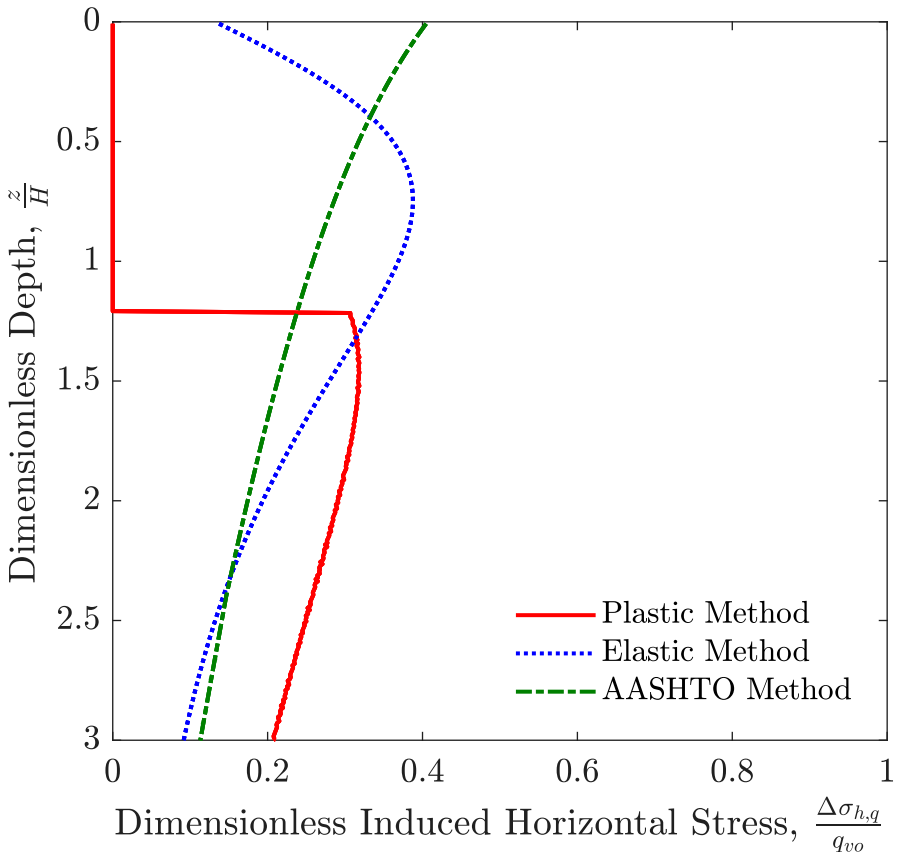

Figure D.1. Comparison of induced horizontal stresses from surcharge for each method for $\frac{d}{H} = 1.2$, $\frac{q_h}{q_{vo}} = 0.3$, and $\frac{q_{vo}}{\gamma H} = 1$.

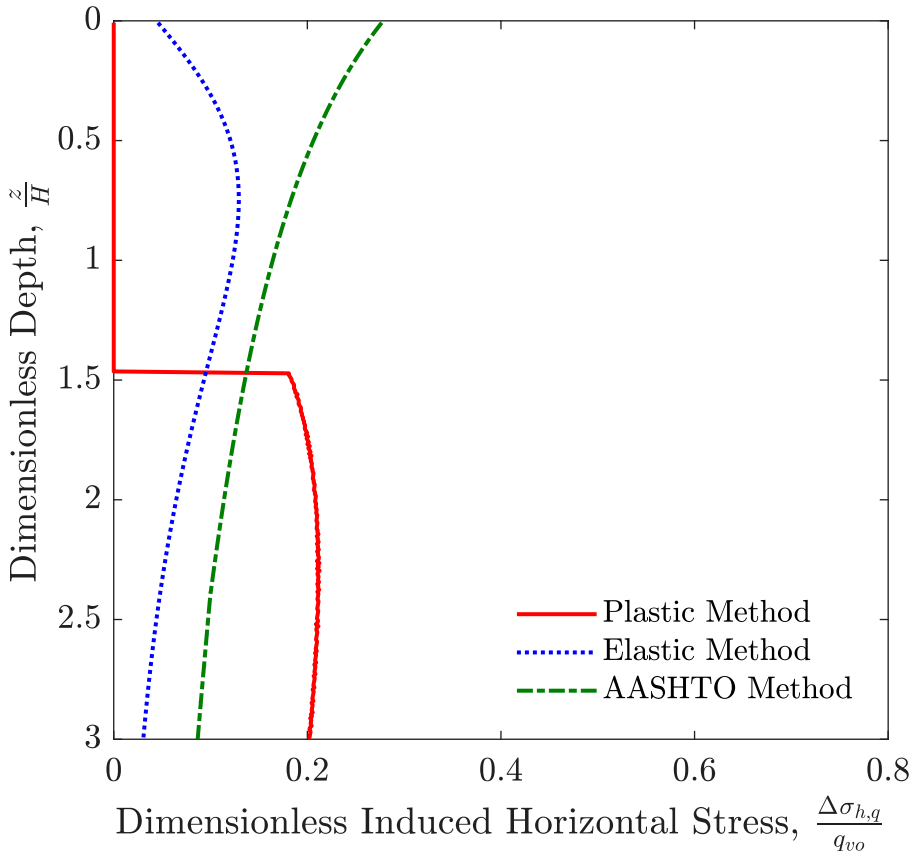

Figure D.2. Comparison of induced horizontal stresses from surcharge for each method for $\frac{d}{H} = 1.2$, $\frac{q_h}{q_{vo}} = 0.1$, and $\frac{q_{vo}}{\gamma H} = 1$.

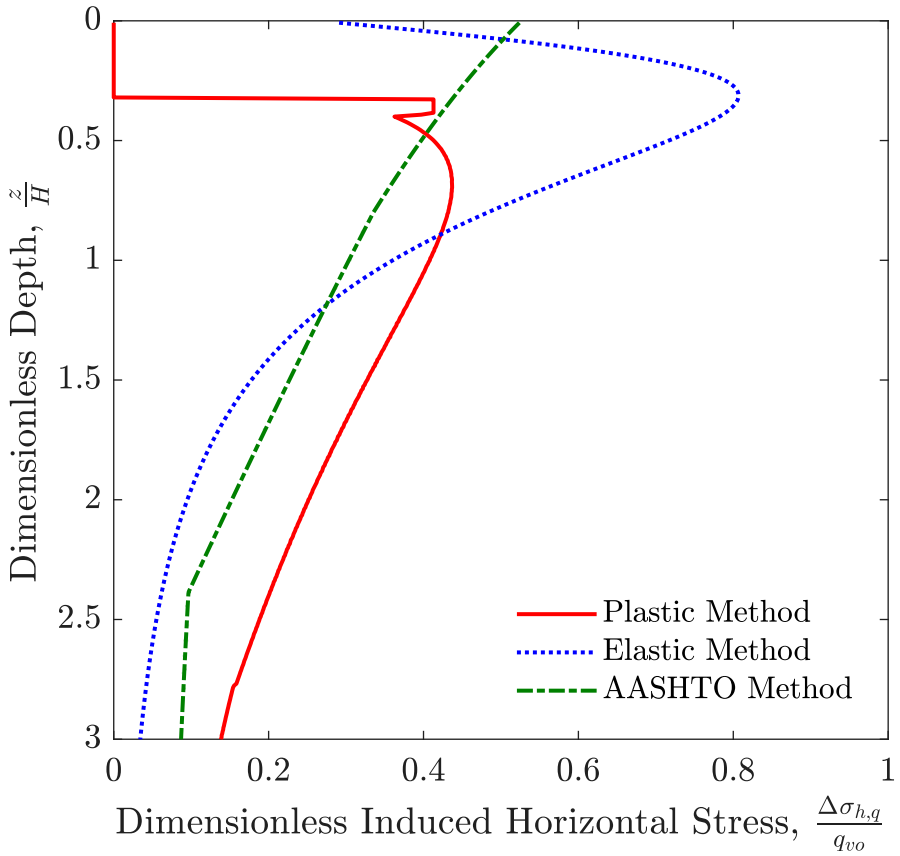

Figure D.3. Comparison of induced horizontal stresses from surcharge for each method for $\frac{d}{H} = 0.4$, $\frac{q_h}{q_{vo}} = 0.3$, and $\frac{q_{vo}}{\gamma H} = 1$.

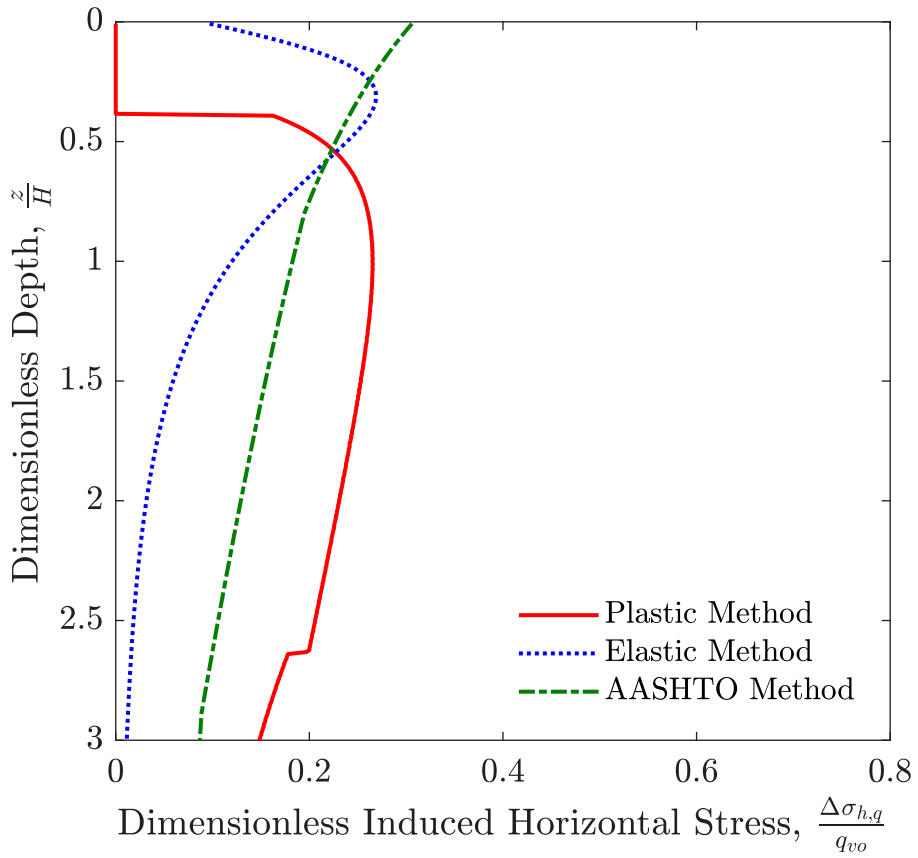

Figure D.4. Comparison of induced horizontal stresses from surcharge for each method for $\frac{d}{H} = 0.4$, $\frac{q_h}{q_{vo}} = 0.1$, and $\frac{q_{vo}}{\gamma H} = 1$.

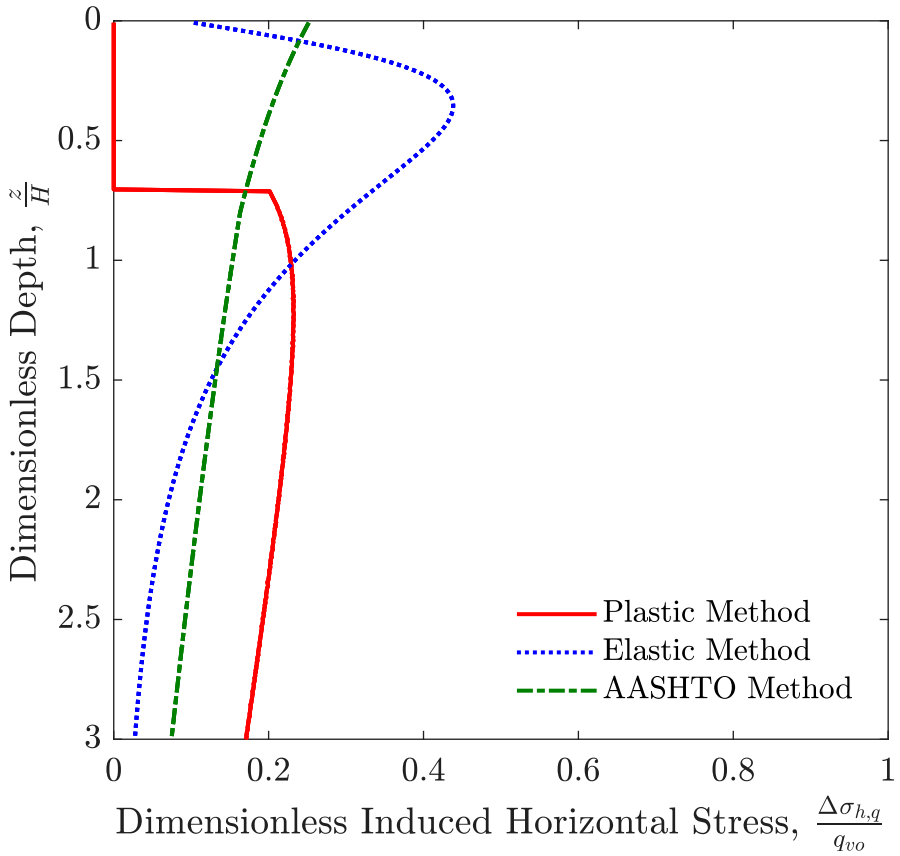

Figure D.5. Comparison of induced horizontal stresses from surcharge for each method for $\frac{d}{H} = 0.4$, $\frac{q_h}{q_{vo}} = 0.1$, and $\frac{q_{vo}}{\gamma H} = 0.1$.

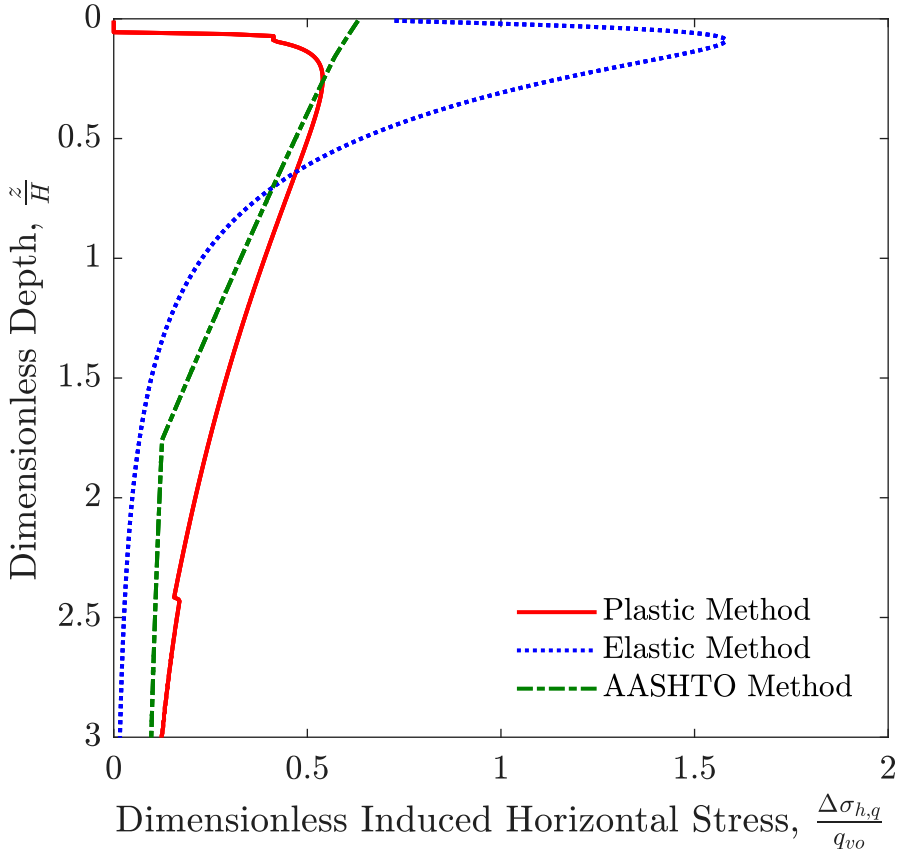

Figure D.6. Comparison of induced horizontal stresses from surcharge for each method for $\frac{d}{H} = 0.1$, $\frac{q_h}{q_{vo}} = 0.3$, and $\frac{q_{vo}}{\gamma H} = 1$.

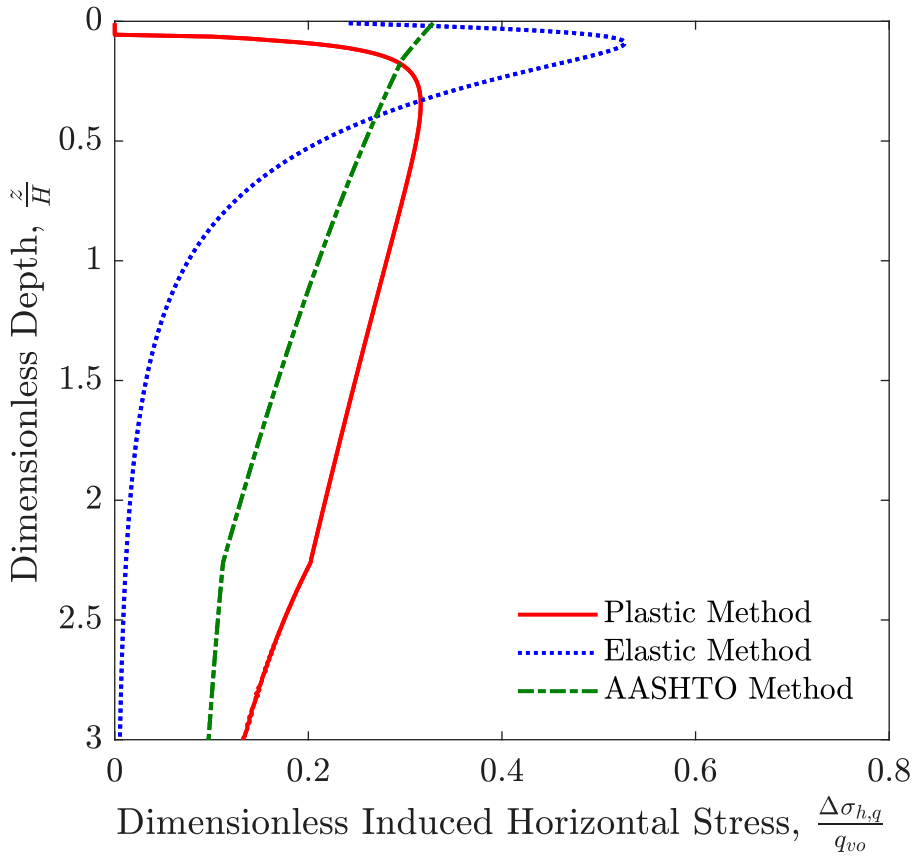

Figure D.7. Comparison of induced horizontal stresses from surcharge for each method for $\frac{d}{H} = 0.1$, $\frac{q_h}{q_{vo}} = 0.1$, and $\frac{q_{vo}}{\gamma H} = 1$.

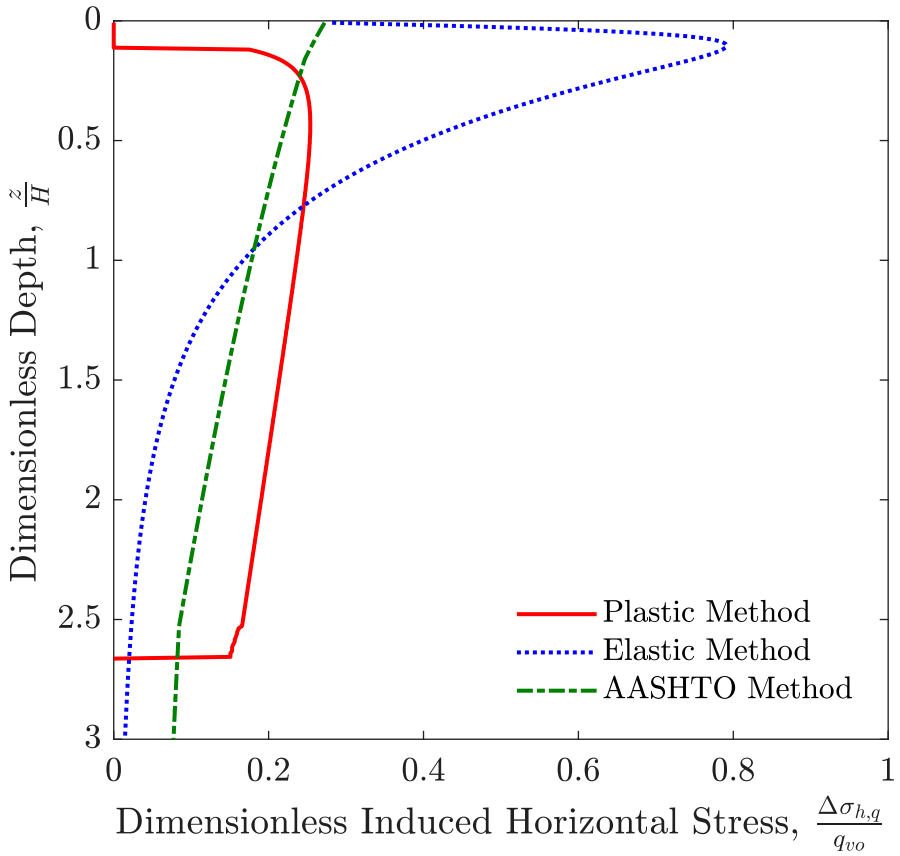

Figure D.8. Comparison of induced horizontal stresses from surcharge for each method for $\frac{d}{H} = 0.1$, $\frac{q_h}{q_{vo}} = 0.1$, and $\frac{q_{vo}}{\gamma H} = 0.1$.

Comparison of Measured and Predicted Bending Moments

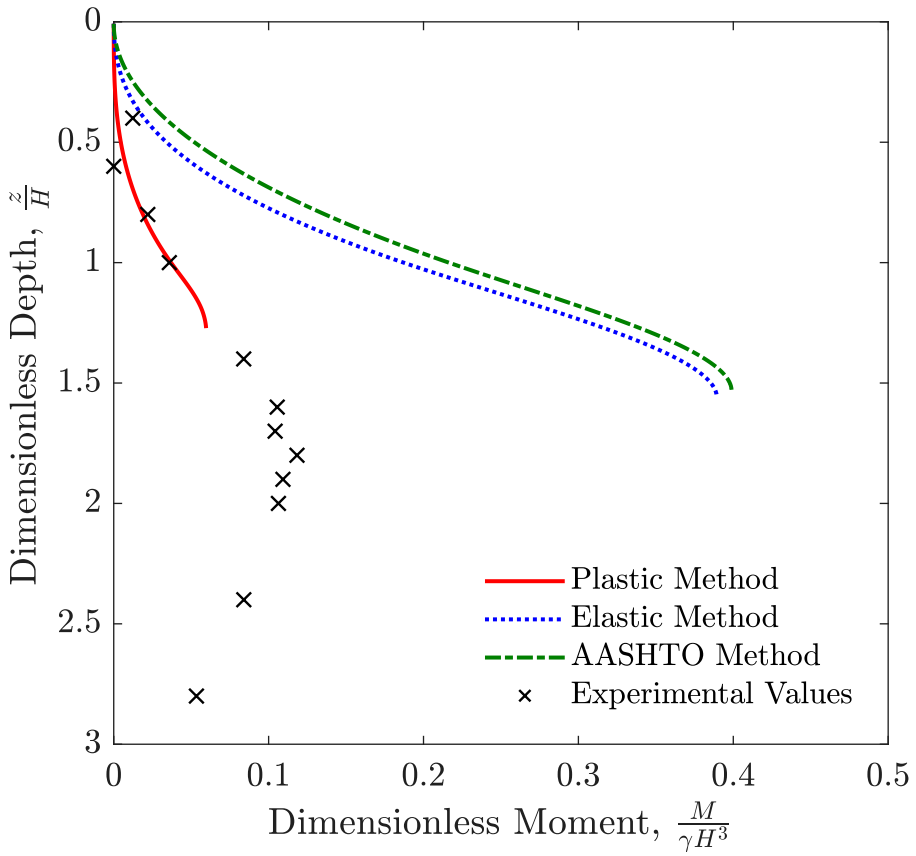

Figure D.9. Comparison of observed and predicted dimensionless moments for each of the three methods for $\frac{d}{H} = 1.2$, $\frac{q_h}{q_{vo}} = 0.3$, and $\frac{q_{vo}}{\gamma H} = 1$.

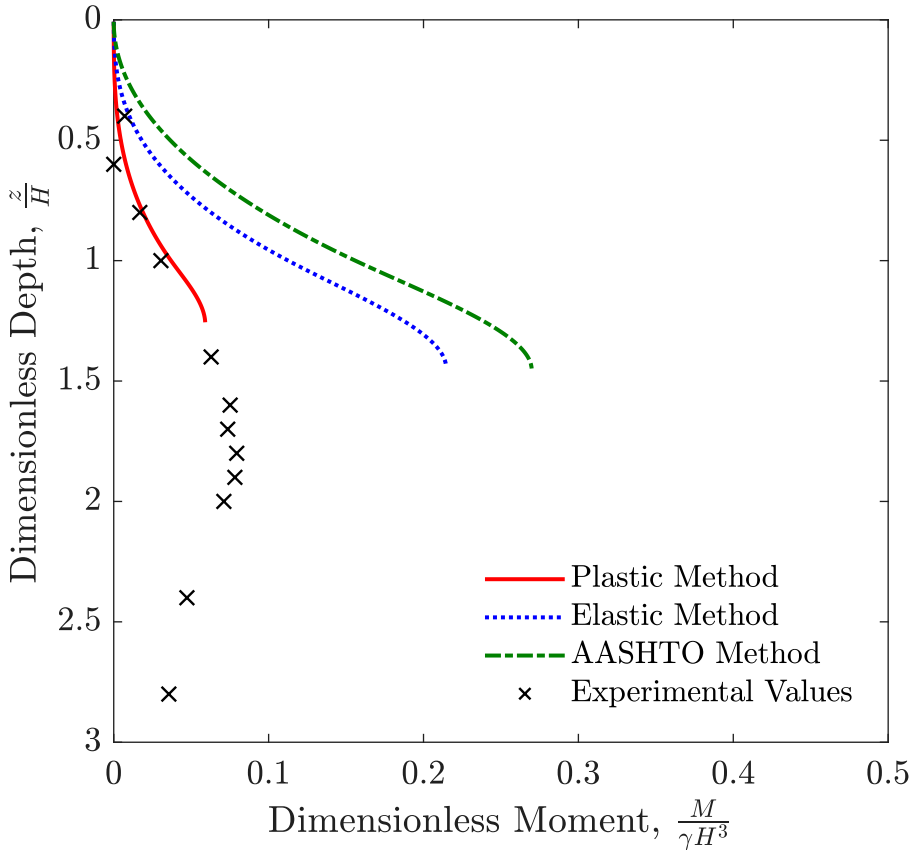

Figure D.10. Comparison of observed and predicted dimensionless moments for each of the three methods for $\frac{d}{H} = 1.2$, $\frac{q_h}{q_{vo}} = 0.1$, and $\frac{q_{vo}}{\gamma H} = 1$.

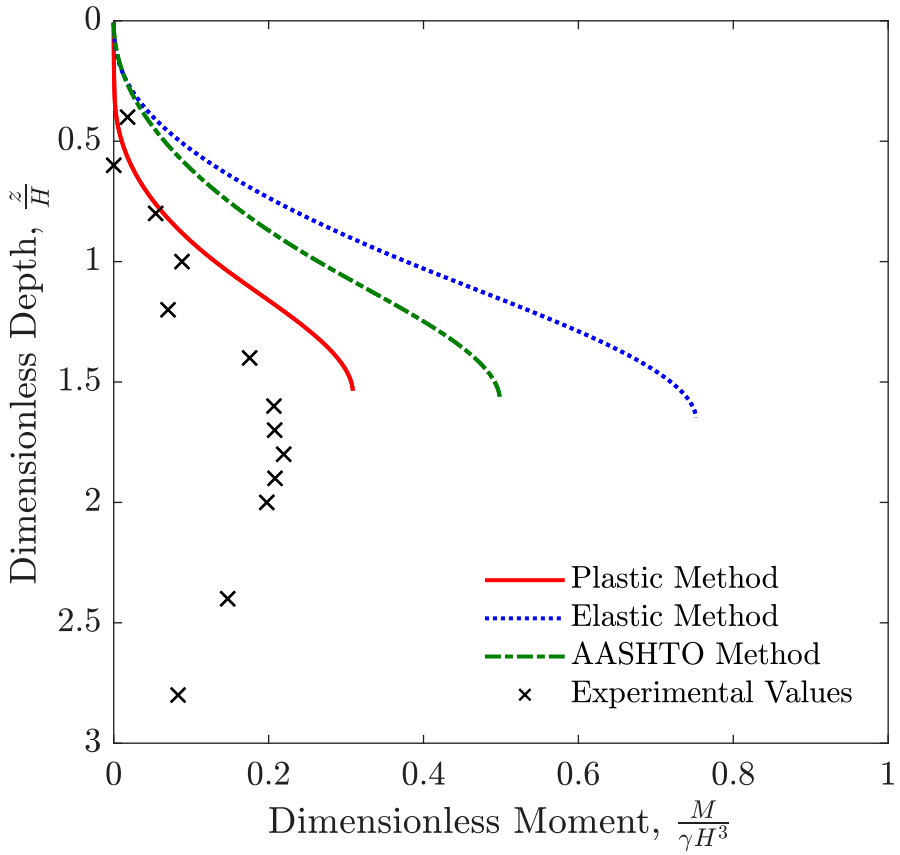

Figure D.11. Comparison of observed and predicted dimensionless moments for each of the three methods for $\frac{d}{H} = 0.4$, $\frac{q_h}{q_{vo}} = 0.3$, and $\frac{q_{vo}}{\gamma H} = 1$.

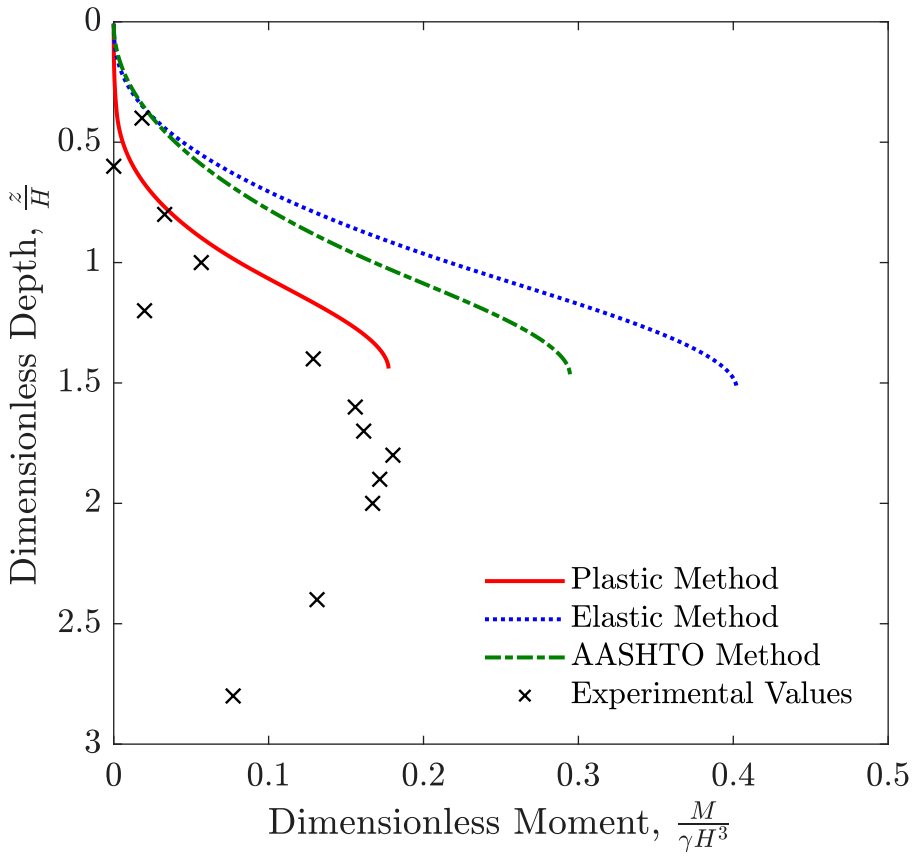

Figure D.12. Comparison of observed and predicted dimensionless moments for each of the three methods for $\frac{d}{H} = 0.4$, $\frac{q_h}{q_{vo}} = 0.1$, and $\frac{q_{vo}}{\gamma H} = 1$.

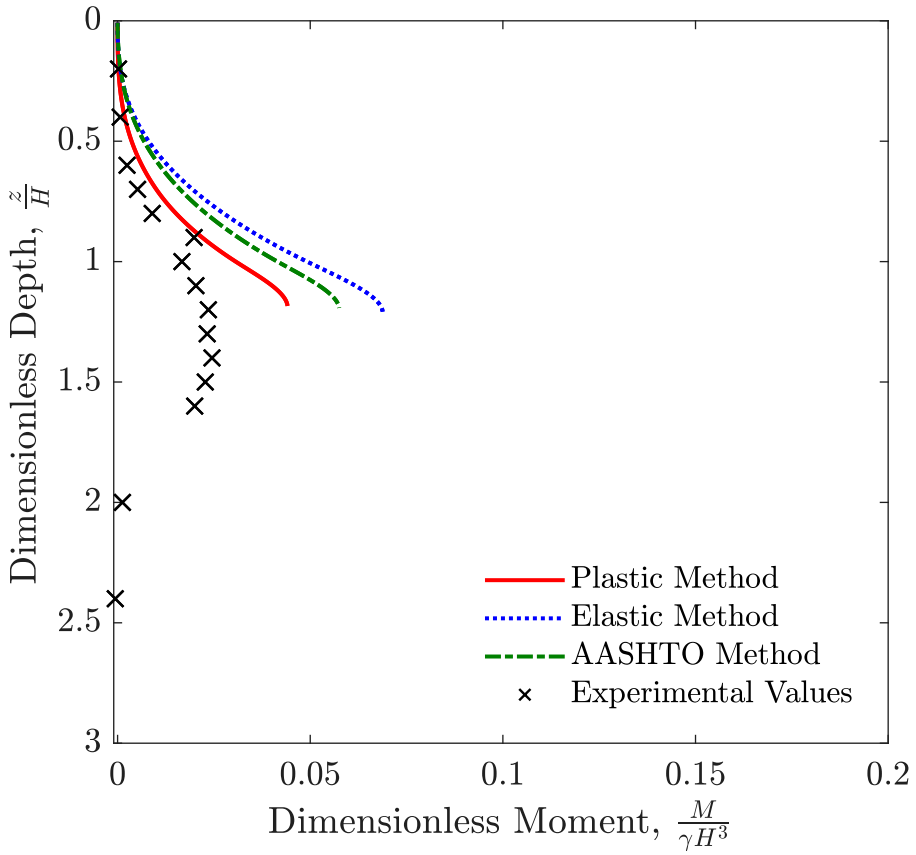

Figure D.13. Comparison of observed and predicted dimensionless moments for each of the three methods for $\frac{d}{H} = 0.4$, $\frac{q_h}{q_{vo}} = 0.1$, and $\frac{q_{vo}}{\gamma H} = 0.1$.

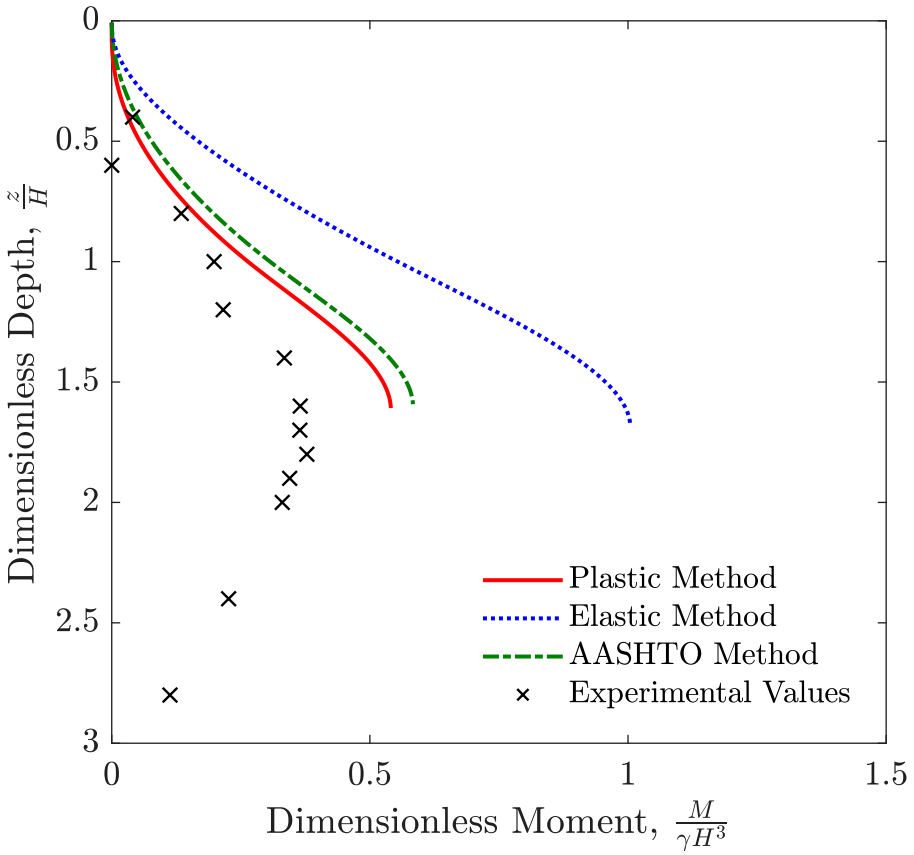

Figure D.14. Comparison of observed and predicted dimensionless moments for each of the three methods for $\frac{d}{H} = 0.1$, $\frac{q_h}{q_{vo}} = 0.3$, and $\frac{q_{vo}}{\gamma H} = 1$.

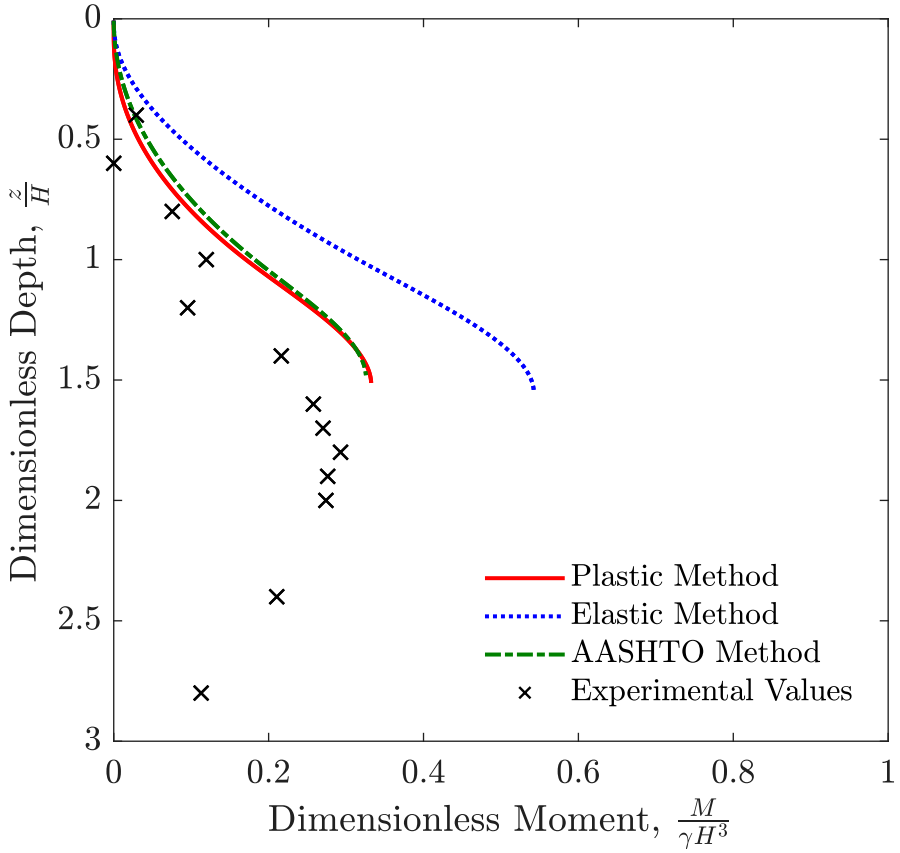

Figure D.15. Comparison of observed and predicted dimensionless moments for each of the three methods for $\frac{d}{H} = 0.1$, $\frac{q_h}{q_{vo}} = 0.1$, and $\frac{q_{vo}}{\gamma H} = 1$.

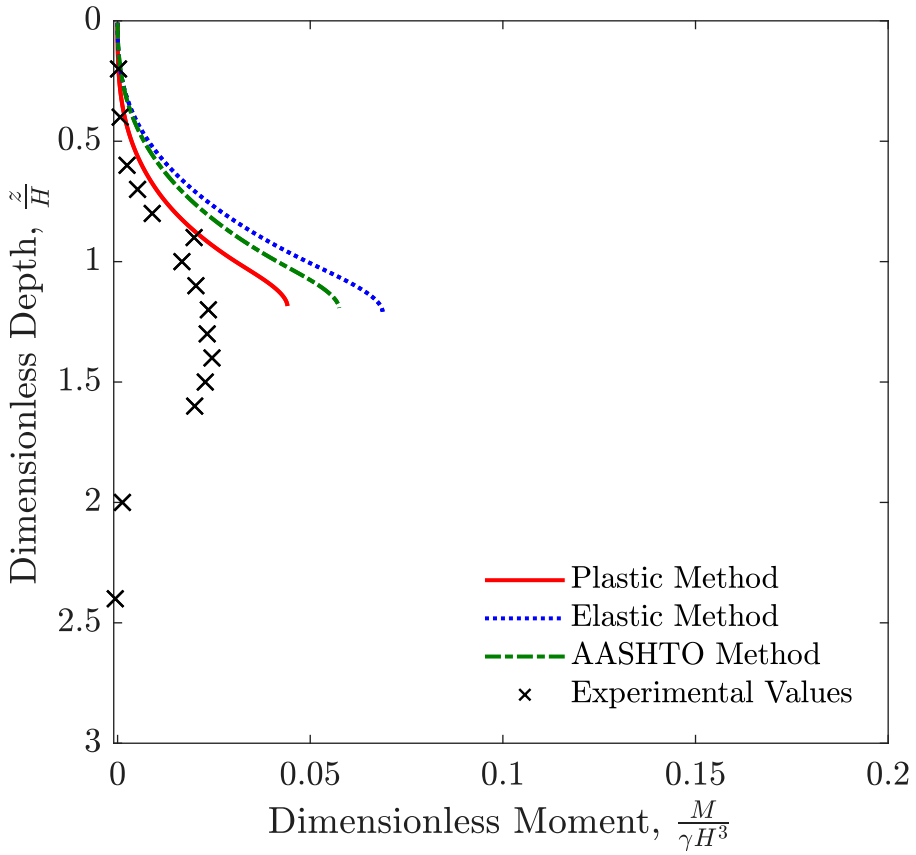

Figure D.16. Comparison of observed and predicted dimensionless moments for each of the three methods for $\frac{d}{H} = 0.1$, $\frac{q_h}{q_{vo}} = 0.1$, and $\frac{q_{vo}}{\gamma H} = 0.1$.